The Astrophysical Journal, 930:95 (28pp), 2022 May 1 https://doi.org/10.3847/1538-4357/ac59b7

Quantifying Wave–Particle Interactions in Collisionless Plasmas: Theory and Its Application to the Alfvén-mode Wave

Jinsong Zhao[1,2], Louchuang Lee[3,4], Huasheng Xie[5,6], Yuhang Yao[1,2], Dejin Wu[1], Yuriy Voitenko[7], and Viviane, Pierrard[7,8]

[1] Key Laboratory of Planetary Sciences, Purple Mountain Observatory, Chinese Academy of Sciences, Nanjing 210023, People's Republic of China
js_zhao@pmo.ac.cn
[2] School of Astronomy and Space Science, University of Science and Technology of China, Hefei 230026, People's Republic of China
[3] Institute of Earth Sciences, Academia Sinica, Taipei, 11529, Taiwan
[4] Space Science Institute, Macau University of Science and Technology, Macau, People's Republic of China
[5] Hebei Key Laboratory of Compact Fusion, Langfang 065001, People's Republic of China
[6] ENN Science and Technology Development Co., Ltd., Langfang 065001, People's Republic of China
[7] Solar-Terrestrial Centre of Excellence, Space Physics Division, Royal Belgian Institute for Space Aeronomy, 3 av. Circulaire, B-1180, Brussels, Belgium
[8] Center for Space Radiations, ELIC, Université Catholique de Louvain, B-1348 Louvain-La-Neuve, Belgium

Received 2021 December 1; revised 2022 February 28; accepted 2022 February 28; published 2022 May 6

Abstract

Wave–particle interactions can induce energy transfer at different timescales in collisionless plasmas, which leads to the reshaping of the particle velocity distribution function. Therefore, how to quantify wave–particle interactions is one of the fundamental problems in the heliosphere and in astrophysical plasmas. This study proposes a systematic method to quantify linear wave–particle interactions based on the Vlasov–Maxwellian model. We introduce energy transfer rates with various expressions by using perturbed electric fields and perturbed particle velocity distribution functions. Then, we use different expressions of the energy transfer rate to perform a comprehensive investigation of wave–particle interactions of the Alfvén-mode wave. We clarify the physical mechanisms responsible for the damping of the Alfvén-mode wave in wavevector space. Moreover, this study exhibits for the first time evident signatures of wave–particle interactions between Alfvén-mode waves and resonant/nonresonant particles in the velocity space. These resonant and nonresonant particles can induce energy transfer in opposite directions, which leads to self-regulation of the particle velocity distribution function. Furthermore, this study exhibits a comprehensive dependence of wave–particle interactions of the Alfvén-mode wave on the wavenumber and plasma beta (the ratio between the plasma thermal pressure and the magnetic pressure). These results illustrate that the proposed method would be very useful for quantifying different types of linear wave–particle interactions of an arbitrary wave mode.

Unified Astronomy Thesaurus concepts: Plasma physics (2089); Plasma astrophysics (1261); Space plasmas (1544); Solar wind (1534)

1. Introduction

In most of the heliosphere and in astrophysical plasma environments, such as the solar corona, the solar wind, the interstellar medium, and the intracluster medium, collisionless wave–particle interactions, instead of collisions among particles, play a key role in determining the particle dynamics. On one hand, a nonequilibrium particle velocity distribution function can release the free energy into plasma waves through wave–particle interactions (e.g., Verscharen et al. 2019; Sun et al. 2021; Liu et al. 2021). On the other hand, plasma waves can energize particles, leading to plasma heating and particle acceleration (e.g., Marsch 2006). Moreover, space and astrophysical turbulence is widely believed to be dissipated via wave–particle interactions (e.g., Leamon et al. 1998; Howes et al. 2008; Schekochihin et al. 2009; Woodham et al. 2018; He et al. 2020). Consequently, how wave–particle interactions affect the particle velocity distribution function is a fundamental problem in the heliosphere and astrophysical plasma communities.

Plasma waves that cover various spatial and temporal scales can interact with particles through different types of wave–particle interactions, e.g., Landau interaction, transit-time interaction, and normal/anomalous cyclotron interaction (e.g., Barnes 1966; Kennel & Engelmann 1966; Stix 1992). For example, Landau and transit-time interactions are responsible for the damping of low-frequency kinetic-scale Alfvén waves (e.g., Quataert 1998), and the normal ion-cyclotron interaction dominates the damping of Alfvén-mode waves near the ion-cyclotron frequency (e.g., Kennel & Engelmann 1966). Based on numerical simulations and spacecraft observational data, a method using the field–particle correlation is proposed to diagnose the electron Landau damping of the electrostatic Langmuir wave (Klein & Howes 2016; Howes et al. 2017), the electron and ion Landau damping of the kinetic-scale Alfvén wave (Klein et al. 2017; Chen et al. 2019; Verniero et al. 2021), and the ion-cyclotron damping of high-frequency Alfvén waves in velocity space (Klein et al. 2020). Recently, Cerri et al. (2021) proposed a possible signature of transit-time damping in velocity space in Alfvénic turbulence simulations. However, the aforementioned studies normally pay attention to wave–particle interactions related to resonant particles.

This paper further develops the field–particle correlation method to quantify wave–particle interactions of both resonant and nonresonant particles in collisionless plasmas. Through the energy transfer rate calculated using the electric field and particle velocity distribution function perturbations, we can directly diagnose signatures of wave–particle interactions associated with resonant and nonresonant particles in velocity space in which resonant particles satisfy the resonant condition of $v_{\|}k_{\|} - \omega_r + n\Omega_{\rm cs} = 0$, whereas nonresonant particles do not follow this resonant condition. Here $v_{\|}$ denotes the parallel velocity of particles, $k_{\|}$ denotes the wavenumber parallel to the background magnetic field, ω_r denotes the wave frequency, $\Omega_{\rm cs}$ denotes the cyclotron frequency of the particle species "s", and n denotes an integer.

This paper also uses this correlation method to quantify linear wave–particle interactions of the Alfvén-mode wave in velocity space. Based on the analysis of energy transfer rates, we propose that the Alfvén-mode wave in the wavevector space can be mainly classified into four typical wave regimes: the quasi-parallel and medium oblique MHD Alfvén wave regime, the quasi-parallel ion-cyclotron wave regime, the quasi-perpendicular MHD and ion-scale Alfvén wave regime, and the sub-ion-scale Alfvén wave regime. Moreover, this study explores the dependence of the wave–particle interaction of a parallel Alfvén wave and a highly oblique Alfvén wave on the plasma beta (the ratio between the plasma thermal pressure and the magnetic pressure).

This paper is organized as follows. In Section 2, we give basic equations for quantifying wave–particle interactions in collisionless plasmas. Section 3 uses the energy transfer rate to quantify linear wave–particle interactions of the Alfvén-mode wave. Section 4 provides a detailed analysis of the distributions of resonant and nonresonant energy transfer rates of four typical Alfvén-mode waves in velocity space. The discussion and summary are presented in Sections 5 and 6, respectively.

2. Basic Equations for Quantifying Wave–Particle Interactions in Collisionless Plasmas

In a collisionless or weakly collisional plasma, the particle dynamics can be described by the Vlasov equation:

$$\frac{\partial f_s}{\partial t} + \boldsymbol{v} \cdot \frac{\partial f_s}{\partial \boldsymbol{r}} + \frac{q_s}{m_s}(\boldsymbol{E} + \boldsymbol{v} \times \boldsymbol{B}) \cdot \frac{\partial f_s}{\partial \boldsymbol{v}} = 0, \tag{1}$$

where f_s, q_s, and m_s represent the velocity distribution function, the charge, and the mass of particle species "s," respectively. $\boldsymbol{E}$ and $\boldsymbol{B}$ represent the electric and magnetic fields, respectively.

In order to perform the linearization of Equation (1), we consider f_s to consist of a zero-order term f_{s0}, a first-order term f_{s1}, and a second-order term f_{s2}, i.e., $f_s = f_{s0} + \varepsilon f_{s1} + \varepsilon^2 f_{s2}$, where $\varepsilon \ll 1$. Similarly, $\boldsymbol{B}$ is given by $\boldsymbol{B} = \boldsymbol{B}_0 + \varepsilon \boldsymbol{B}_1 + \varepsilon^2 \boldsymbol{B}_2$, where $\boldsymbol{B}_0 = B_0 \hat{\boldsymbol{e}}_z$ denotes a background magnetic field, $\boldsymbol{B}_1$ denotes the first-order magnetic field perturbation, and $\boldsymbol{B}_2$ denotes the second-order magnetic field perturbation. We also assume there is no bulk flow crossing $\boldsymbol{B}_0$, and $\boldsymbol{E}$ is therefore given as $\boldsymbol{E} \simeq \varepsilon \boldsymbol{E}_1 + \varepsilon^2 \boldsymbol{E}_2$, where $\boldsymbol{E}_1$ and $\boldsymbol{E}_2$ represent the first-order and second-order electric field perturbations, respectively. We note that the third-order and higher-order terms are ignored.

In a homogeneous plasma environment, a steady background particle velocity distribution f_{s0} is only a function of the velocity $\boldsymbol{v}$, independent of the time t and the position $\boldsymbol{r}$ (i.e., $\partial f_{s0}/\partial t = 0$ and $\partial f_{s0}/\partial \boldsymbol{r} = 0$). Therefore, f_{s0} behaves as a gyrotropic distribution function, i.e., $(\boldsymbol{v} \times \boldsymbol{B}_0) \cdot \partial f_{s0}/\partial \boldsymbol{v} = 0$ or $\partial f_{s0}/\partial \phi = 0$, where $\phi = \mathrm{atan}(v_y/v_x)$.

Under the aforementioned conditions, the first-order (ε) linearized Vlasov equation is

$$\frac{\partial f_{s1}}{\partial t} + \boldsymbol{v} \cdot \frac{\partial f_{s1}}{\partial \boldsymbol{r}} + \frac{q_s}{m_s}(\boldsymbol{v} \times \boldsymbol{B}_0) \cdot \frac{\partial f_{s1}}{\partial \boldsymbol{v}} + \frac{q_s}{m_s}(\boldsymbol{E}_1 + \boldsymbol{v} \times \boldsymbol{B}_1) \cdot \frac{\partial f_{s0}}{\partial \boldsymbol{v}} = 0, \tag{2}$$

and the second-order (ε^2) linearized equation is

$$\frac{\partial f_{s2}}{\partial t} + \boldsymbol{v} \cdot \frac{\partial f_{s2}}{\partial \boldsymbol{r}} + \frac{q_s}{m_s}(\boldsymbol{v} \times \boldsymbol{B}_0) \cdot \frac{\partial f_{s2}}{\partial \boldsymbol{v}} + \frac{q_s}{m_s}(\boldsymbol{E}_2 + \boldsymbol{v} \times \boldsymbol{B}_2) \cdot \frac{\partial f_{s0}}{\partial \boldsymbol{v}} + \frac{q_s}{m_s}(\boldsymbol{E}_1 + \boldsymbol{v} \times \boldsymbol{B}_1) \cdot \frac{\partial f_{s1}}{\partial \boldsymbol{v}} = 0. \tag{3}$$

2.1. The Dynamic Equation of the First-order Particle Kinetic Energy

Here we consider the change of the first-order kinetic energy of the particle species "s," which is defined as $\mathcal{E}_{s1} = \iint d\boldsymbol{r} d\boldsymbol{v}\,(m_s v^2 f_{s1}/2)$.

Multiplying Equation (2) by $m_s v^2/2$ and integrating in velocity and configuration space, we have

$$\begin{aligned}\frac{\partial \mathcal{E}_{s1}}{\partial t} = &- \iint d\boldsymbol{r} d\boldsymbol{v} \left[\boldsymbol{v} \cdot \frac{\partial}{\partial \boldsymbol{r}}\left(\frac{1}{2} m_s v^2 f_{s1}\right)\right] \\ &- \frac{q_s}{2} \iint d\boldsymbol{r} d\boldsymbol{v} \left[v^2 (\boldsymbol{v} \times \boldsymbol{B}_0) \cdot \frac{\partial f_{s1}}{\partial \boldsymbol{v}}\right] \\ &- \frac{q_s}{2} \iint d\boldsymbol{r} d\boldsymbol{v} \left[v^2 (\boldsymbol{v} \times \boldsymbol{B}_1) \cdot \frac{\partial f_{s0}}{\partial \boldsymbol{v}}\right] \\ &- \frac{q_s}{2} \iint d\boldsymbol{r} d\boldsymbol{v} \left(v^2 \boldsymbol{E}_1 \cdot \frac{\partial f_{s0}}{\partial \boldsymbol{v}}\right).\end{aligned} \tag{4}$$

The first term on the right-hand side of Equation (4) is associated with the ballistic movement of particles (Howes et al. 2017; Klein et al. 2017). Because this ballistic term is only dependent on the gradient of the first-order kinetic energy density of particle species "s," i.e., $\partial_{\boldsymbol{r}}(m_s v^2 f_{s1}/2)$, the integration in configuration space is zero when f_{s1} is periodically varying therein (Howes et al. 2017; Klein et al. 2017).

The second and third terms on the right-hand side of Equation (4) are induced by the Lorentz forces $q_s \boldsymbol{v} \times \boldsymbol{B}_0$ and $q_s \boldsymbol{v} \times \boldsymbol{B}_1$, respectively. The Lorentz forces only change the moving direction of particles, not their kinetic energy. As a consequence, these two terms are zero.

The fourth term on the right-hand side of Equation (4) is rewritten as the following expression via integration by parts,

$$-\frac{q_s}{2} \iint d\boldsymbol{r} d\boldsymbol{v} \left(v^2 \boldsymbol{E}_1 \cdot \frac{\partial f_{s0}}{\partial \boldsymbol{v}}\right) = \int d\boldsymbol{r}\,(\boldsymbol{E}_1 \cdot \boldsymbol{J}_{s0}), \tag{5}$$

where $\boldsymbol{J}_{s0} = \int d\boldsymbol{v}\,(q_s \boldsymbol{v} f_{s0})$ is the current density carried by drift particles. For a plasma with zero-current condition, $\sum_s \boldsymbol{J}_{s0} = 0$, we have $\int d\boldsymbol{r} \sum_s (\boldsymbol{E}_1 \cdot \boldsymbol{J}_{s0}) = 0$, indicating that this term does not contribute to the net change of the first-order kinetic energy of total particle species.

Based on these arguments, the first-order particle kinetic energy of the total particle species does not change with time.

2.2. The Dynamic Equation of the Second-order Particle Kinetic Energy

Multiplying Equation (3) by $m_s v^2/2$ and integrating in velocity and configuration space, we obtain the dynamic equation for the change in the second-order kinetic energy,

$$\begin{aligned}\frac{\partial \mathcal{E}_{s2}}{\partial t} = &- \iint d\boldsymbol{r}d\boldsymbol{v}\left[\boldsymbol{v}\cdot\frac{\partial}{\partial \boldsymbol{r}}\left(\frac{1}{2}m_s v^2 f_{s2}\right)\right]\\ &- \frac{q_s}{2}\iint d\boldsymbol{r}d\boldsymbol{v}\left[v^2(\boldsymbol{v}\times\boldsymbol{B}_0)\cdot\frac{\partial f_{s2}}{\partial \boldsymbol{v}}\right]\\ &- \frac{q_s}{2}\iint d\boldsymbol{r}d\boldsymbol{v}\left[v^2(\boldsymbol{v}\times\boldsymbol{B}_2)\cdot\frac{\partial f_{s0}}{\partial \boldsymbol{v}}\right]\\ &- \frac{q_s}{2}\iint d\boldsymbol{r}d\boldsymbol{v}\left[v^2(\boldsymbol{v}\times\boldsymbol{B}_1)\cdot\frac{\partial f_{s1}}{\partial \boldsymbol{v}}\right]\\ &- \frac{q_s}{2}\iint d\boldsymbol{r}d\boldsymbol{v}\left(v^2\boldsymbol{E}_2\cdot\frac{\partial f_{s0}}{\partial \boldsymbol{v}}\right)\\ &- \frac{q_s}{2}\iint d\boldsymbol{r}d\boldsymbol{v}\left(v^2\boldsymbol{E}_1\cdot\frac{\partial f_{s1}}{\partial \boldsymbol{v}}\right) \end{aligned}\tag{6}$$

with

$$\mathcal{E}_{s2} = \iint d\boldsymbol{r}d\boldsymbol{v}\left(\frac{1}{2}m_s v^2 f_{s2}\right).$$

The first term on the right-hand side of Equation (6) results from the particle's ballistic motion related to f_{s2}. The second, third, and fourth terms are induced by Lorentz forces $q_s\boldsymbol{v}\times\boldsymbol{B}_0$, $q_s\boldsymbol{v}\times\boldsymbol{B}_2$, and $q_s\boldsymbol{v}\times\boldsymbol{B}_1$, respectively. These terms are zero according to the same physical argument stated in Section 2.1. The fifth term can be rewritten as $\int d\boldsymbol{r}(\boldsymbol{E}_2\cdot\boldsymbol{J}_{s0})$, which does not contribute to the change of $\sum_s \mathcal{E}_{s2}$ under the condition $\sum_s \boldsymbol{J}_{s0} = 0$. Consequently, only the sixth term controls the net change of $\mathcal{E}_{s2}$,

$$\frac{\partial \mathcal{E}_{s2}}{\partial t} = -\frac{q_s}{2}\iint d\boldsymbol{r}d\boldsymbol{v}\left(v^2\boldsymbol{E}_1\cdot\frac{\partial f_{s1}}{\partial \boldsymbol{v}}\right),\tag{7}$$

which is rewritten as

$$\begin{aligned}\frac{\partial \mathcal{E}_{s2}}{\partial t} = &-\frac{q_s}{2}\iint d\boldsymbol{r}d\boldsymbol{v}\left[\boldsymbol{E}_1\cdot\frac{\partial}{\partial \boldsymbol{v}}(v^2 f_{s1})\right]\\ &+ q_s\iint d\boldsymbol{r}d\boldsymbol{v}(\boldsymbol{E}_1\cdot\boldsymbol{v}f_{s1}).\end{aligned}\tag{8}$$

In the first term on the right-hand side of Equation (8), the integration function $-(q_s\boldsymbol{E}_1/m_s)\cdot\partial_{\boldsymbol{v}}(m_s v^2 f_{s1}/2)$ relates to the gradient of the first-order kinetic energy in units of phase space, $\partial_{\boldsymbol{v}}(m_s v^2 f_{s1}/2)$. Its integration is zero due to $(m_s v^2 f_{s1}/2)\to 0$ at $|v|\to\infty$. Therefore, only the second term is responsible for the net change of $\mathcal{E}_{s2}$. We finally obtain

$$\begin{aligned}\frac{\partial \mathcal{E}_{s2}}{\partial t} &= q_s\iint d\boldsymbol{r}d\boldsymbol{v}(\boldsymbol{E}_1\cdot\boldsymbol{v}f_{s1})\\ &= \int d\boldsymbol{r}(\boldsymbol{E}_1\cdot\boldsymbol{J}_{s1}),\end{aligned}\tag{9}$$

where $J_{s1} = \int d\boldsymbol{v}(q_s\boldsymbol{v}f_{s1})$. Equation (9) indicates that a net energy transfer between the plasma waves and particles is controlled by the dot product between the electric field and current density perturbations (e.g., Stix 1992; Howes et al. 2017; Klein et al. 2017).

Based on Equations (9), considering the only source of the net energy transfer between the waves and particles, the dynamical equation of the particle kinetic energy in units of phase space e_s is given by

$$\frac{\partial e_s}{\partial t} = q_s\boldsymbol{E}_1\cdot\boldsymbol{v}f_{s1},\tag{10}$$

and its integration in velocity space yields

$$\frac{\partial}{\partial t}\int d\boldsymbol{v}e_s = \boldsymbol{E}_1\cdot\boldsymbol{J}_{s1}.\tag{11}$$

Here we define $e_s \equiv m_s v^2 f_{s2}'/2$, in which f_{s2}' is different from f_{s2} (see Equation (3)). The former is only affected by the electric field force, and the latter is controlled by the interplay of the pressure gradient force, Lorentz force, and electric field force.

2.3. Energy Transfer and Energy Transfer Rate of the Monochromatic Plasma Wave

Now we consider the energy transfer between the particles and the monochromatic plasma wave.

When a plasma wave behaves as a plane wave, its first-order electric field, current density, and particle velocity distribution function perturbation are given as

$$\begin{aligned}\boldsymbol{E}_1 &= \frac{1}{2}[\widetilde{\boldsymbol{E}}_1 e^{-i(\omega t-\boldsymbol{k}\cdot\boldsymbol{r})} + \widetilde{\boldsymbol{E}}_1^* e^{i(\omega^* t-\boldsymbol{k}\cdot\boldsymbol{r})}],\\ \boldsymbol{J}_{s1} &= \frac{1}{2}[\widetilde{\boldsymbol{J}}_{s1} e^{-i(\omega t-\boldsymbol{k}\cdot\boldsymbol{r})} + \widetilde{\boldsymbol{J}}_{s1}^* e^{i(\omega^* t-\boldsymbol{k}\cdot\boldsymbol{r})}],\\ f_{s1} &= \frac{1}{2}[\widetilde{f}_{s1} e^{-i(\omega t-\boldsymbol{k}\cdot\boldsymbol{r})} + \widetilde{f}_{s1}^* e^{i(\omega^* t-\boldsymbol{k}\cdot\boldsymbol{r})}],\end{aligned}\tag{12}$$

where $\widetilde{\boldsymbol{E}}_1$, $\widetilde{\boldsymbol{J}}_{s1}$, and $\widetilde{f}_{s1}$ denote the electric field, current density, and particle velocity distribution function perturbations in Fourier space, respectively. $\boldsymbol{k}$ denotes the wavevector, and the superscript "*" denotes the complex conjugate.

Using expressions in Equation (12), Equations (10) and (11) are rewritten as

$$\begin{aligned}\frac{\partial e_s}{\partial t} = &\frac{q_s}{4}\widetilde{\boldsymbol{E}}_1\cdot\boldsymbol{v}\widetilde{f}_{s1}e^{-i2(\omega t-\boldsymbol{k}\cdot\boldsymbol{r})} + \frac{q_s}{4}\widetilde{\boldsymbol{E}}_1^*\cdot\boldsymbol{v}\widetilde{f}_{s1}^* e^{i2(\omega^* t-\boldsymbol{k}\cdot\boldsymbol{r})}\\ &+ \frac{q_s}{4}\widetilde{\boldsymbol{E}}_1\cdot\boldsymbol{v}\widetilde{f}_{s1}^* e^{i(\omega^*-\omega)t} + \frac{q_s}{4}\widetilde{\boldsymbol{E}}_1^*\cdot\boldsymbol{v}\widetilde{f}_{s1}e^{i(\omega^*-\omega)t},\end{aligned}\tag{13}$$

and

$$\begin{aligned}\frac{\partial}{\partial t}\int d\boldsymbol{v}e_s = &\frac{1}{4}\widetilde{\boldsymbol{E}}_1\cdot\widetilde{\boldsymbol{J}}_{s1}e^{-i2(\omega t-\boldsymbol{k}\cdot\boldsymbol{r})} + \frac{1}{4}\widetilde{\boldsymbol{E}}_1^*\cdot\widetilde{\boldsymbol{J}}_{s1}^* e^{i2(\omega^* t-\boldsymbol{k}\cdot\boldsymbol{r})}\\ &+ \frac{1}{4}\widetilde{\boldsymbol{E}}_1\cdot\widetilde{\boldsymbol{J}}_{s1}^* e^{i(\omega^*-\omega)t} + \frac{1}{4}\widetilde{\boldsymbol{E}}_1^*\cdot\widetilde{\boldsymbol{J}}_{s1}e^{i(\omega^*-\omega)t}.\end{aligned}\tag{14}$$

Considering $\omega = \omega_r + i\gamma$ (where ω_r is the real part of ω and γ is the imaginary part of ω), there exist two kinds of varying timescales of e_s and $\int d\boldsymbol{v}e_s$: $\propto\exp(\pm i2\omega_r t)$ and $\propto\exp(2\gamma t)$. The former corresponds to the oscillation at a timescale of $1/(2\omega_r)$, and the latter describes a continuously increasing or decreasing energy density with time. These oscillation terms can disappear after averaging over one wave period, and therefore, the nonoscillation terms are responsible for the net energy transfer between the particles and plasma waves.

Now we only consider the nonoscillation terms in Equations (13) and (14), and we rewrite these two equations as

$$\frac{\partial e_s}{\partial t} = \frac{q_s}{4}(\widetilde{\boldsymbol{E}}_1 \cdot \boldsymbol{v}\widetilde{f}_{s1}^{*} + \widetilde{\boldsymbol{E}}_1^{*} \cdot \boldsymbol{v}\widetilde{f}_{s1})e^{2\gamma t} \tag{15}$$

and

$$\frac{\partial}{\partial t}\int d\boldsymbol{v} e_s = \frac{1}{4}(\widetilde{\boldsymbol{E}}_1 \cdot \widetilde{\boldsymbol{J}}_{s1}^{*} + \widetilde{\boldsymbol{E}}_1^{*} \cdot \widetilde{\boldsymbol{J}}_{s1})e^{2\gamma t}. \tag{16}$$

To better quantify the energy transfer between plasma waves and particles, we further rewrite Equations (15) and (16) in terms of the nonoscillation part of the wave electromagnetic field energy $W_{\rm EB}\exp(2\gamma t)$,

$$\frac{\partial e_s}{\partial t} = P_s(\boldsymbol{v})W_{\rm EB}e^{2\gamma t} \tag{17}$$

and

$$\frac{\partial}{\partial t}\int d\boldsymbol{v} e_s = P_{\rm st}W_{\rm EB}e^{2\gamma t} \tag{18}$$

with

$$P_s(\boldsymbol{v}) = \frac{q_s(\widetilde{\boldsymbol{E}}_1 \cdot \boldsymbol{v}\widetilde{f}_{s1}^{*} + \widetilde{\boldsymbol{E}}_1^{*} \cdot \boldsymbol{v}\widetilde{f}_{s1})}{4W_{\rm EB}}, \tag{19}$$

$$P_{\rm st} = \int d\boldsymbol{v} P_s(\boldsymbol{v}) = \frac{\widetilde{\boldsymbol{E}}_1 \cdot \widetilde{\boldsymbol{J}}_{s1}^{*} + \widetilde{\boldsymbol{E}}_1^{*} \cdot \widetilde{\boldsymbol{J}}_{s1}}{4W_{\rm EB}}, \tag{20}$$

and $W_{\rm EB} = \varepsilon_0|\widetilde{\boldsymbol{E}}|^2/4 + |\widetilde{\boldsymbol{B}}|^2/4\mu_0$. The physical meaning of $P_s(\boldsymbol{v})$ is energy emission/absorption per unit of phase space, per unit of electromagnetic energy, and per unit of time. The expression (20) has been used to identify Landau and/or cyclotron resonant interactions in studies of Alfvén-mode waves and of electron/ion beam instabilities (e.g., He et al. 2019; Duan et al. 2020; He et al. 2020; Sun et al. 2021; Liu et al. 2021; Kitamura et al. 2021).

$P_s(\boldsymbol{v})$ is the energy transfer rate in three-dimensional (3D) velocity space, and $P_{\rm st}$ is the energy transfer rate integrated in 3D velocity space. Similarly, one-dimensional (1D) and two-dimensional (2D) energy transfer rates are defined as

$$P_s(v_i) = \iint dv_j dv_k P_s(\boldsymbol{v}) \tag{21}$$

and

$$P_s(v_i, v_j) = \int dv_k P_s(\boldsymbol{v}), \tag{22}$$

where i, j, and k represent the three axes (x, y, z) in a Cartesian coordinate system.

When we consider the cylindrical velocity coordinates ($v_\parallel$, $v_\perp$, ϕ), the 1D and 2D energy transfer rates are then defined as

$$P_s(v_\parallel) = \int dv_\perp P_s(v_\parallel, v_\perp),$$
$$P_s(v_\perp) = \int dv_\parallel P_s(v_\parallel, v_\perp), \tag{23}$$

and

$$P_s(v_\parallel, v_\perp) = \int d\phi v_\perp P_s(v_\parallel, v_\perp, \phi). \tag{24}$$

In this study, the transformation formulas from Cartesian coordinates (v_x, v_y, v_z) into cylindrical coordinates ($v_\parallel$, $v_\perp$, ϕ) are $v_\parallel = v_z$, $v_\perp = (v_x^2 + v_y^2)^{1/2}$, and $\phi = {\rm atan}(v_y/v_x)$.

Moreover, in order to explore the role of each kind of wave–particle interaction on wave damping or growth, the energy transfer rate concerning each electric field component and each n in velocity space can be given by

$$P_{sl}(\boldsymbol{v}) = \frac{q_s(\widetilde{E}_{1l}v_l\widetilde{f}_{s1}^{*} + \widetilde{E}_{1l}^{*}v_l\widetilde{f}_{s1})}{4W_{\rm EB}} \tag{25}$$

and

$$P_s(\boldsymbol{v}, n) = \frac{q_s(\widetilde{\boldsymbol{E}}_1 \cdot \boldsymbol{v}\widetilde{f}_{s1}^{*}(\boldsymbol{v}, n) + \widetilde{\boldsymbol{E}}_1^{*} \cdot \boldsymbol{v}\widetilde{f}_{s1}(\boldsymbol{v}, n))}{4W_{\rm EB}}, \tag{26}$$

where "l" is x, y, or z. n can determine the nature of the wave–particle interaction via the interaction factor $v_\parallel k_\parallel - \omega + n\Omega_{\rm cs}$. The resonant wave–particle interaction arises as the resonant condition $v_\parallel k_\parallel - \omega + n\Omega_{\rm cs} = 0$ is satisfied. Referring to Equations (23)–(24) and using $P_{sl}(\boldsymbol{v})$ and $P_s(\boldsymbol{v}, n)$, we can obtain corresponding 1D and 2D energy transfer rates in cylindrical coordinates.

Due to $\sum_s P_{\rm st} = -2\gamma$ (Liu et al. 2021), the main advantage of using energy transfer rates (e.g., Equations (19)–(26)) is that we can quantify different types of wave–particle interactions contributing to the growth or damping of one mode wave. It should be noted that one can directly calculate the growth or damping rate of plasma waves through the expression of $\gamma = -\sum_s P_{\rm st}/2$. For example, starting from a reduced expression of γ under a weak growth rate condition ($|\gamma| \ll \omega_r$), Kennel & Wong (1967) considered only resonant wave–particle interactions and derived the analytical expression of the growth rate in resonant instabilities.

2.4. The First-order Velocity Distribution Function and Electric Field Perturbations in a Plasma with a Maxwellian Distribution

From the linearized Equation (2), the first-order velocity distribution function can be directly given through the integration of the unperturbed trajectory of the particle (e.g., Stix 1992; Miyamoto 2005),

$$\widetilde{f}_{s1}(\boldsymbol{v}) = \sum_{n=-\infty}^{\infty}\widetilde{f}_{s1}(\boldsymbol{v}, n) = \sum_{n=-\infty}^{\infty}\frac{f_{s1}(\boldsymbol{v}, n)}{v_\parallel - (\omega - n\Omega_{\rm cs})/k_\parallel}, \tag{27}$$

where

$$\begin{aligned} f_{s1}(\boldsymbol{v}, n) = {}& \frac{iq_s}{m_s k_\parallel}e^{ia_s\sin(\phi)}e^{-in\phi}\Bigg[\frac{n}{a_s}UJ_n(a_s)\widetilde{E}_x \\ & + iUJ_n'(a_s)\widetilde{E}_y + \left(\frac{n}{a_s}W + \frac{\partial f_0}{\partial v_\parallel}\right)J_n(a_s)\widetilde{E}_z\Bigg], \\ U = {}& \left(1 - \frac{k_\parallel v_\parallel}{\omega}\right)\frac{\partial f_0}{\partial v_\perp} + \frac{k_\parallel v_\perp}{\omega}\frac{\partial f_0}{\partial v_\parallel}, \\ W = {}& \frac{k_\perp v_\parallel}{\omega}\frac{\partial f_0}{\partial v_\perp} - \frac{k_\perp v_\perp}{\omega}\frac{\partial f_0}{\partial v_\parallel}, \end{aligned}$$

J_n is the nth Bessel function of the first kind, $a_s = k_\perp v_\perp/\Omega_{\rm cs}$, and $V_{\rm ts}$ and $\Omega_{\rm cs}$ are the thermal speed and the cyclotron frequency of the particle species "s," respectively.

Once an eigenmode and adjoined eigenfunctions are known, one can obtain $\widetilde{f}_{s1}$ through Equation (27). Eigenmodes and eigenfunctions in plasmas can be obtained through the wave equation in terms of the electric field perturbation,

$$c^2\boldsymbol{k} \times (\boldsymbol{k} \times \widetilde{\boldsymbol{E}}_1) + \omega^2\boldsymbol{K} \cdot \widetilde{\boldsymbol{E}}_1 = 0, \tag{28}$$

which is derived from Equation (27) and Maxwellian's equations,

$$\begin{aligned} \boldsymbol{k} \times \widetilde{\boldsymbol{B}}_1 &= -i\mu_0 \int d\boldsymbol{v}(q_s\boldsymbol{v}\widetilde{f}_{s1}) - \frac{\omega}{c^2}\widetilde{\boldsymbol{E}}_1, \\ \boldsymbol{k} \times \widetilde{\boldsymbol{E}}_1 &= \omega\widetilde{\boldsymbol{B}}_1. \end{aligned} \tag{29}$$

In Equation (28), $\boldsymbol{K}$ represents the dielectric tensor, and c is the light speed. By combining Equations (27) and (28), we can obtain both the first-order velocity distribution function and electric field perturbations.

Before the analysis of wave–particle interactions of both resonant and nonresonant particles is performed, it needs to identify the contributions of these two kinds of particles to the integral over the velocity for a function related to $\widetilde{f}_{s1}$. These resonant and nonresonant particles can have distinct contributions to the integral in the velocity space in the case of $\gamma < 0$. For example, in the following integral at the condition of $\gamma < 0$,

$$\begin{aligned} \int d\boldsymbol{v}[\widetilde{\boldsymbol{E}}_1^* \cdot \boldsymbol{v}\widetilde{f}_{s1}(\boldsymbol{v}, n)] &= P\int d\boldsymbol{v}\left[\frac{\widetilde{\boldsymbol{E}}_1^* \cdot \boldsymbol{v}f_{s1}(\boldsymbol{v}, n)}{v_\parallel - V_{\rm rn} - i\gamma/k_\parallel}\right] \\ &\quad + i2\pi\int d\boldsymbol{v}[\widetilde{\boldsymbol{E}}_1^* \cdot \boldsymbol{v}f_{s1}(\boldsymbol{v}, n)]\delta(v_\parallel - V_{\rm rn}), \end{aligned} \tag{30}$$

the first term (the principal value of the integral) comes from the contribution of nonresonant particles, and the second term (the analytical continuation for the singular point arising at $v_\parallel = V_{\rm rn}$ in the integral) results from resonant particles, where $V_{\rm rn} = (\omega_r - n\Omega_{\rm cs})/k_\parallel$ denotes the resonant velocity. Note that the principal value of the integral equals $\int d\boldsymbol{v}\left[\frac{\widetilde{\boldsymbol{E}}_1^* \cdot \boldsymbol{v}f_{s1}(\boldsymbol{v},n)}{v_\parallel - V_{\rm rn} - i\gamma/k_\parallel}\right]$ for $\gamma < 0$. Consequently, we can naturally distinguish wave–particle interactions associated with these two types of particles for $\gamma < 0$ in theory.

On the other hand, considering the growing case ($\gamma > 0$) and assuming $\gamma \to 0$, one can have

$$\begin{aligned} \int d\boldsymbol{v}[\widetilde{\boldsymbol{E}}_1^* \cdot \boldsymbol{v}\widetilde{f}_{s1}(\boldsymbol{v}, n)] &= P\int d\boldsymbol{v}\left[\frac{\widetilde{\boldsymbol{E}}_1^* \cdot \boldsymbol{v}f_{s1}(\boldsymbol{v}, n)}{v_\parallel - V_{\rm rn} - i\gamma/k_\parallel}\right] \\ &\quad + i\pi\int d\boldsymbol{v}[\widetilde{\boldsymbol{E}}_1^* \cdot \boldsymbol{v}f_{s1}(\boldsymbol{v}, n)]\delta(v_\parallel - V_{\rm rn}), \end{aligned} \tag{31}$$

where $\frac{1}{i(v_\parallel - V_{\rm rn}) + \gamma/k_\parallel} \simeq P\frac{1}{i(v_\parallel - V_{\rm rn}) + \gamma/k_\parallel} + \pi\delta(v_\parallel - V_{\rm rn})$ at $\gamma \to 0^+$ is used. The principal value term and δ-function term correspond to the contributions of nonresonant and resonant particles, respectively. A similar procedure has been used to analyze the quasilinear evolution of the electron velocity distribution function resulting from wave–particle interactions of both resonant and nonresonant electrons (Drummond & Pines 1962; Sagdeev & Galeev 1969).

However, for a finite positive γ (which indicates the condition $\gamma \to 0$ being not satisfied), there is no singularity in the velocity integral related to the function of $(v_\parallel - V_{\rm rn} - i\gamma/k_\parallel)^{-1}$. Hence, we cannot distinguish the difference between nonresonant and resonant particles through the analysis of the principal value term and the δ-function term as shown in Equation (31). We will study wave–particle interactions of the growing wave ($\gamma > 0$) in the next work, and in this study, we focus on wave–particle interactions of the damping wave ($\gamma < 0$).

In order to exhibit wave–particle interactions of both resonant and nonresonant particles in the case of $\gamma < 0$, we use the following expression to calculate the energy transfer rate distribution in 2D and 3D velocity space,

$$\begin{aligned} \boldsymbol{v}\widetilde{f}_{s1}(\boldsymbol{v}, n) = {} & \frac{\boldsymbol{v}f_{s1}(\boldsymbol{v}, n)}{v_\parallel - V_{\rm rn} - i\gamma/k_\parallel} \\ & + i2\pi(\boldsymbol{v}f_{s1}(\boldsymbol{v}, n))\delta(v_\parallel - V_{\rm rn}). \end{aligned} \tag{32}$$

We also note that when $\gamma = 0$, $\boldsymbol{v}\widetilde{f}_{s1}(\boldsymbol{v}, n) = \boldsymbol{v}f_{s1}(\boldsymbol{v}, n)/(v_\parallel - V_{\rm rn}) + i\pi\boldsymbol{v}f_{s1}(\boldsymbol{v}, n)\delta(v_\parallel - V_{\rm rn})$.

Because the plasma is usually modeled by use of the thermal equilibrium Maxwellian distribution function, this study will show the basic properties of wave–particle interactions in a Maxwellian plasma with isotropic temperatures ($V_{\rm ts\perp} = V_{\rm ts\parallel} = V_{\rm ts}$),

$$f_{s0} = \frac{n_{s0}}{\pi^{3/2}V_{\rm ts}^3}\exp\left(-\frac{v_\parallel^2 + v_\perp^2}{V_{\rm ts}^2}\right), \tag{33}$$

where n_{s0} denotes the background number density of the particle species "s."

All basic plasma waves correspond to the solutions of Equation (28). In this study, we use Newton's iteration method to numerically solve Equation (28) under the Maxwellian distribution (Equation (33)), in which the initial guess value is given through the matrix eigenvalue method (Xie 2019; Xie et al. 2021), and we simultaneously obtain the wave frequency and electric field perturbations. In addition, this study considers the wavevector being limited to the x–z plane in Cartesian coordinates, i.e., $\boldsymbol{k} = k_\perp\boldsymbol{e}_x + k_\parallel\boldsymbol{e}_z$.

3. Quantifying Wave–Particle Interactions of the Alfvén-mode Wave in a Typical Inner Heliosphere Environment

Here we use energy transfer rates defined in the last section to quantify different types of linear wave–particle interactions of the Alfvén-mode wave.

The wave dispersion and damping of the Alfvén-mode wave can be considerably affected by the magnetic field strength and plasma parameters (e.g., the plasma beta β, and the ratio between the ion and electron temperatures T_i/T_e; Quataert 1998; Hollweg 1999; Zhao 2015; Wu & Chen 2020). This study does not plan to proceed with a comprehensive parameter investigation for wave–particle interactions of the Alfvén-mode wave but mainly focuses on a typical plasma environment in the inner heliosphere. The proton plasma parameters and magnetic field strength used in this study are $n_{\rm p0} \simeq 286$ cm^{-3}, $T_p \simeq 27$ eV, and $B_0 \simeq 91$ nT based on the Parker Solar Probe measurement at $t \sim 15{:}00$ on 2018 November 5, in which the spacecraft position approximates 36 times the solar radius. The number density and temperature of the electron population are assumed as $n_{\rm e0} = n_{\rm p0}$ and $T_e = T_p$. These parameters yield $\beta_p = \beta_e \simeq 0.37$. Referring to a recent observation on the Alfvén-mode wave by Duan et al. (2021), who showed the existence of both quasi-parallel and quasi-perpendicular Alfvén waves from 14:30 to 15:30 on 2018 November 5, we will exhibit the basic properties of the

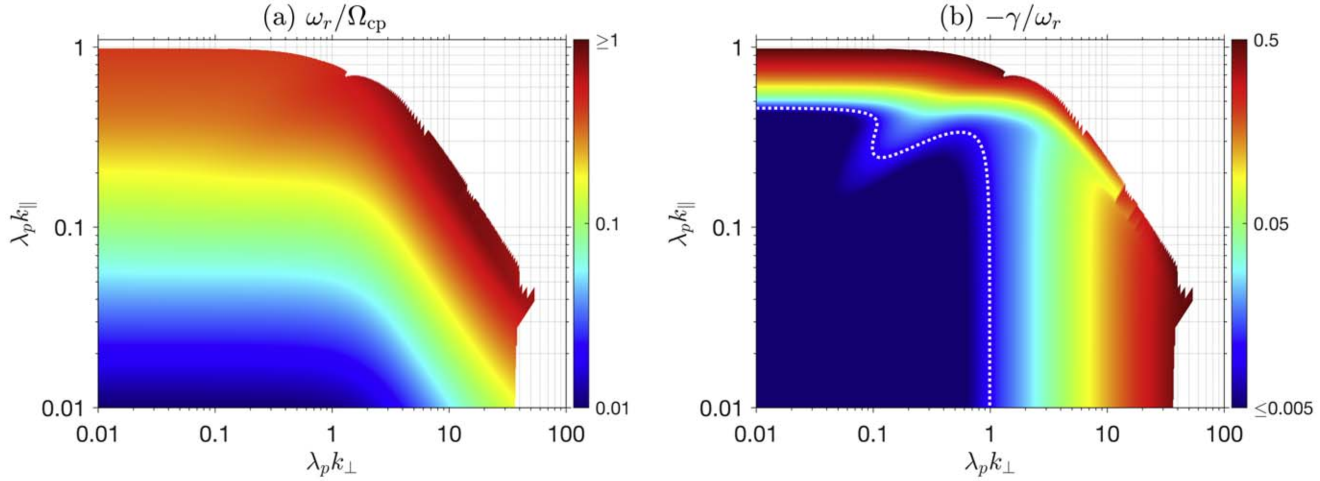

Figure 1. Dispersion surface and damping rate of the Alfvén-mode wave: (a) the real wave frequency normalized by the proton cyclotron frequency, $\omega_r/\Omega_{\rm cp}$, and (b) the imaginary part of the wave frequency normalized by the real wave frequency, $-\gamma/\omega_r$. The dotted curve in panel (b) denotes the contour at $\gamma = -0.01\ \omega_r$.

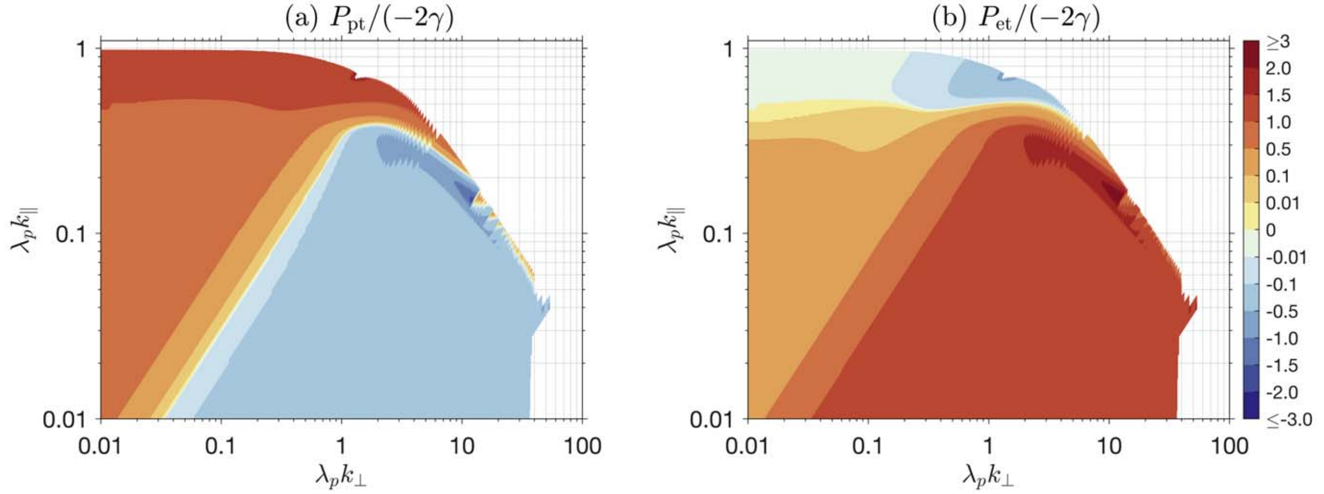

Figure 2. Total energy transfer rates in $k_\perp$–$k_\parallel$ space: (a) the proton energy transfer rate $P_{\rm pt}$ normalized by (-2γ), and (b) the electron energy transfer rate $P_{\rm et}$ normalized by (-2γ).

Alfvén-mode wave in such a typical inner heliosphere environment in theory.

The wave dispersion surface and damping rate in $k_\perp$–$k_\parallel$ space are presented in Figure 1, where the data with the damping rate of $|\gamma|/\omega_r > 0.5$ are ignored. Figure 1(a) shows that the wave dispersion surface extends from MHD scales ($\lambda_p k_{\parallel,\perp} \ll 1$) down to proton scales ($\lambda_p k_\parallel \sim 1$) in the parallel direction and down to electron scales ($\lambda_e k_\perp \sim 1$ or $\lambda_p k_\perp \sim 40$) in the perpendicular direction, where λ_p and λ_e represent the proton and electron inertial lengths, respectively. The wave can even extend to frequency higher than the proton cyclotron frequency in medium oblique propagation ($\theta \sim 62°$). From the damping rate distribution shown by Figure 1(b), the damping rate becomes larger at smaller scales. A larger damping rate corresponds to more resonant particles taking part in wave–particle interactions. Due to the Alfvén wave being dispersive at small wavelength (this dispersive feature is also dependent on the propagation angle), the resonant velocity decreases with increasing wavelength, leading to more particles absorbing energy from the waves. Moreover, the waves become considerably damped (e.g., $|\gamma|/\omega_r \gtrsim 0.01$) as $\lambda_p k_\parallel \gtrsim 0.4$ or $\lambda_p k_\perp \gtrsim 1$. We note that Appendix A summarized more mode properties of the Alfvén-mode wave, and this appendix also exhibits the wave dispersion relations at a transition point where the wave frequency can be larger than $\Omega_{\rm cp}$.

In order to quantify the proton and electron contributions to the wave-damping rate, Figure 2 presents the distributions of total proton and electron energy transfer rates obtained from Equation (20). Here the current density is calculated as

$$\widetilde{\boldsymbol{J}}_s = \boldsymbol{\sigma}_s \cdot \widetilde{\boldsymbol{E}}, \tag{34}$$

where $\boldsymbol{\sigma}_s$ is the conductivity tensor (see Appendix B). This figure shows that the proton dissipation controls the wave damping as $\theta \lesssim 62°$, and the electron dissipation is dominant as $\theta > 62°$. The boundary between proton- and electron-dissipation-dominating regimes roughly corresponds to the position where the left-handed polarized wave turns to right-hand polarization (see Figure 16 in Appendix A). Figure 2 also shows that the proton or electron population would emit energy, e.g., $P_{\rm pt} < 0$ in quasi-perpendicular propagation, and $P_{\rm et} < 0$ at $\lambda_p k_\parallel \gtrsim 0.6$. This energy is flowing into another particle species beyond the electromagnetic field energy, e.g., $P_{\rm et} = -P_{\rm pt} - 2\gamma > 0$ in quasi-perpendicular propagation, and

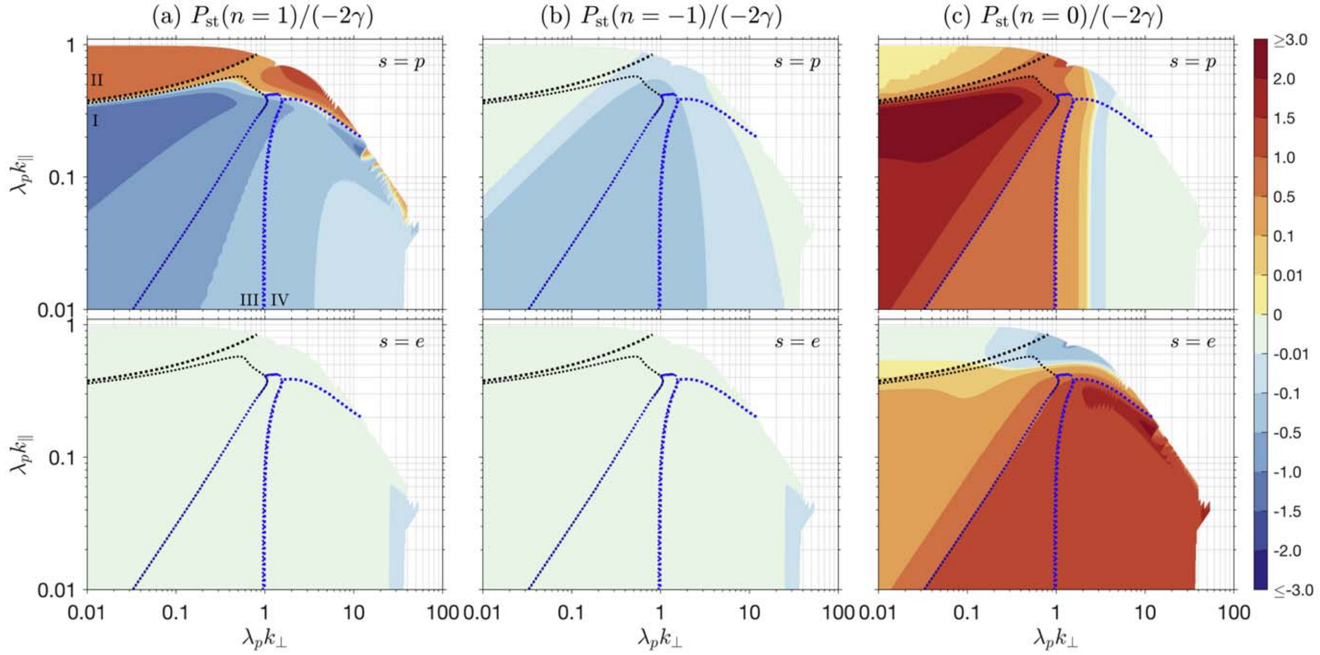

Figure 3. Total energy transfer rates at different n in $k_\perp$–$k_\parallel$ space: (left panels) $n=1$; (middle panels) $n=-1$; and (right panels) $n=0$. (Upper panels) proton energy transfer rates and (bottom panels) electron energy transfer rates. The data are normalized by (-2γ). The four regions surrounded by dotted curves correspond to the quasi-parallel and medium oblique MHD Alfvén wave regime, the quasi-parallel ion-cyclotron wave regime, the quasi-perpendicular MHD and ion-scale Alfvén wave regime, and the quasi-perpendicular sub-ion-scale Alfvén wave regime, respectively. These four regimes are labeled by "I," "II," "III," and "IV" shown in the upper-left panel, respectively.

$P_{\rm pt}=-P_{\rm et}-2\gamma>0$ at $\lambda_p k_\parallel \gtrsim 0.6$. The source of the energy absorption/emission normally comes from resonant/nonresonant particles, and the explanation for the energy change will be given in Section 4 through the analysis of the energy transfer rate distributions in velocity space.

Moreover, in order to identify the contributions of wave–particle interactions at $n=0$ and $n=\pm1$ on the wave damping, we calculate total energy transfer rates $P_{\rm st}$ at different n for each particle species, which are presented in Figure 3. According to the dominant wave–particle interaction shown in Figure 3, the Alfvén-mode wave surface can be roughly classified into the following four regimes.

(i) Quasi-parallel and medium oblique MHD Alfvén waves in Regime I with $\theta \lesssim 72°$. This regime is characterized by $P_{\rm pt}(n=0)/(-2\gamma)\gtrsim 1$. Also, $P_{\rm pt}(n=1)/(-2\gamma)\lesssim -0.5$ and $P_{\rm et}(n=0)/(-2\gamma)\gtrsim 0.1$ in this regime. Consequently, the wave is entirely dissipated through the $n=0$ wave–particle interactions with both resonant protons and electrons.

(ii) Quasi-parallel ion-cyclotron waves in Regime II. This regime is characterized by $P_{\rm pt}(n=1)/(-2\gamma)\gtrsim 0.5$. The corresponding dissipation mechanism is the proton cyclotron damping. At a finite $k_\perp$, $P_{\rm pt}(n=0)$ is small but positive, and this indicates that the $n=0$ wave–particle interactions of resonant protons contribute to the wave dissipation.

(iii) Quasi-perpendicular MHD and ion-scale Alfvén waves in Regime III. This regime is characterized by strong $n=0$ wave–particle interactions with both resonant electrons and protons, e.g., $P_{\rm et}(n=0)/(-2\gamma)\gtrsim 1$ and $P_{\rm pt}(n=0)/(-2\gamma)\gtrsim 0.5$. Due to $P_{\rm pt}(n=1)<0$ and $P_{\rm pt}(n=-1)<0$, the nonresonant proton population also emits energy at $n=\pm1$.

(iv) Quasi-perpendicular sub-ion-scale Alfvén waves in Regime IV, which is characterized by $P_{\rm et}(n=0)/(-2\gamma)\gtrsim 1$. Actually, the electron Landau damping mechanism controls the wave damping (see Appendix D). The second damping mechanism is the electron transit-time damping. In addition, the nonresonant proton population can emit energy because of $P_{\rm pt}(n=1)<0$ and $P_{\rm pt}(n=-1)<0$.

We note that this classification can distinguish well most of Alfvén-mode waves in $k_\perp$–$k_\parallel$ space. For obliquely propagating waves nearby $\lambda_p k_\perp \sim 2$ and $\lambda_p k_\parallel \sim 0.6$, their frequencies are about the proton cyclotron frequency, and the $n=1$ wave–particle interactions dominate the wave damping. We also note that the damping is very weak for MHD Alfvén waves in Regimes I and III (see Figure 1(b)), and consequently, these waves can propagate through a long distance without significant dissipation of the wave energy. However, because this paper plans to give a comprehensive understanding of wave–particle interactions for the Alfvén-mode wave (e.g., the dependence on the wave frequency and wavelength), we will perform a detailed analysis of the energy transfer rate distributions in the four aforementioned typical regimes.

4. Resonant and Nonresonant Energy Transfer Rates of Four Typical Alfvén-mode Waves

In order to explain the energy transfer rates shown in Figures 2 and 3, we will analyze their $v_\perp$–$v_\parallel$ distributions of four typical Alfvén-mode waves listed in Table 1 in detail. Case 1 represents a typical quasi-parallel MHD Alfvén wave in Regime I, which has $\lambda_p k_\perp = 0.01$, $\lambda_p k_\parallel = 0.1$, and $\omega_r/\Omega_{\rm cp}\simeq 0.09$. Case 2 corresponds to a typical quasi-

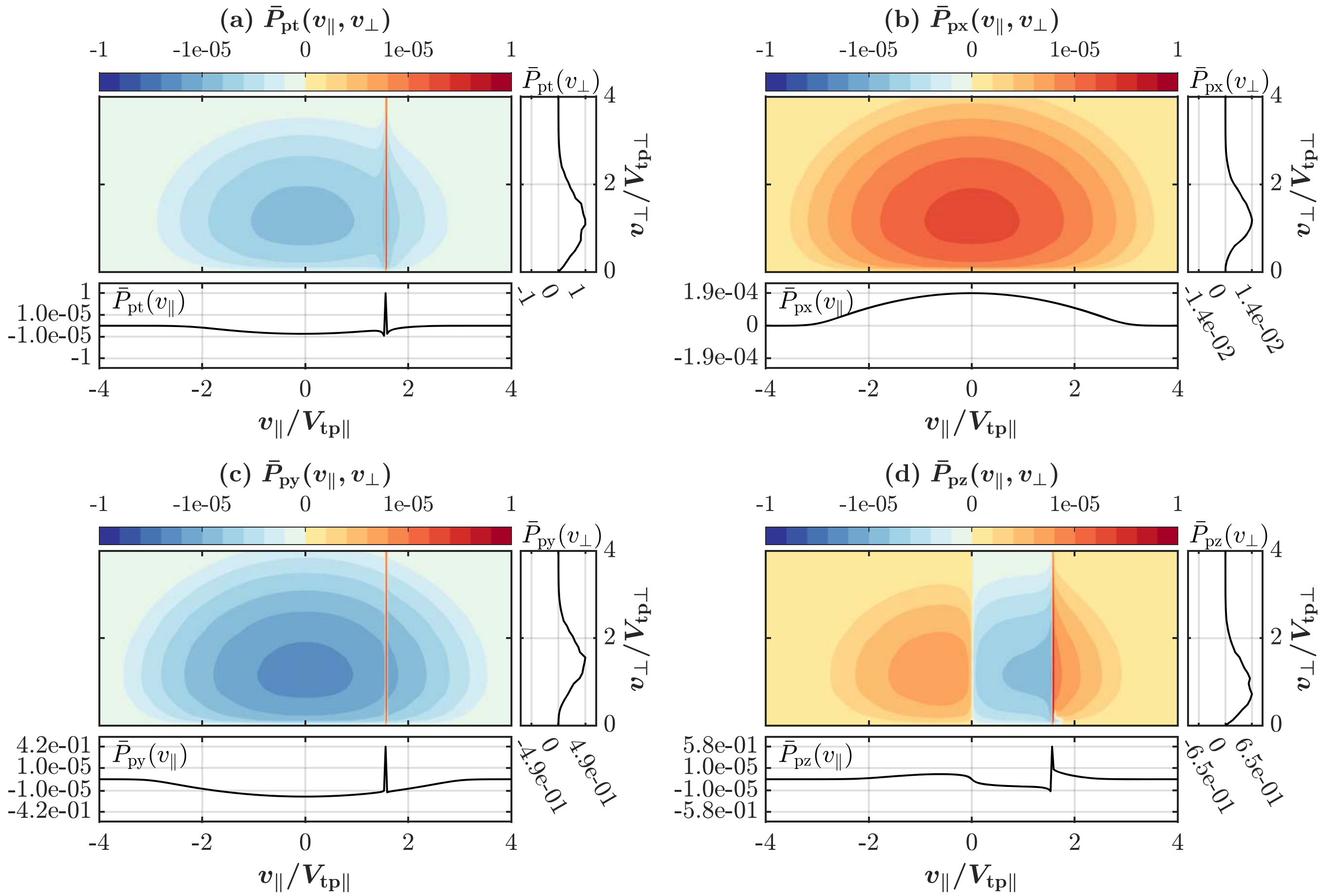

Figure 4. The 1D and 2D distributions of proton energy transfer rates in Case 1, where $\lambda_p k_\perp = 0.01$ and $\lambda_p k_\parallel = 0.1$: (a) the total energy transfer rate, P_{pt}; (b) the x component of the energy transfer rate, P_{px}; (c) the y component of the energy transfer rate, P_{py}; and (d) the parallel energy transfer rate, P_{pz}. The 2D energy transfer rates are normalized by the maximum P_{pt} in the $v_\parallel$–$v_\perp$ plane. The 1D energy transfer rates are normalized by the corresponding maximum $P_{\mathrm{pt}}(v_\parallel)$ or maximum $P_{\mathrm{pt}}(v_\perp)$.

Table 1
Energy Transfer Rates for Four Typical Alfvén-mode Waves

	Wave Parameters				Resonant/Nonresonant $P_p(n)/(-2\gamma)$			Resonant/Nonresonant $P_e(n)/(-2\gamma)$		
	$\lambda_p k_\perp$	$\lambda_p k_\parallel$	$\omega_r/\Omega_{\mathrm{cp}}$	$-\gamma/\omega_r$	$n = 1$	$n = -1$	$n = 0$	$n = 1$	$n = -1$	$n = 0$
Case 1	0.01	0.1	0.09	9×10^{-4}	$0/-1.09$	$0/-10^{-3}$	$3.92/-1.96$	$0/-10^{-4}$	0/0	$0.26/-0.14$
Case 2	0.01	0.7	0.37	0.18	$3.86/-2.86$	0/0	$10^{-3}/-10^{4}$	$0/-10^{-4}$	0/0	0/0
Case 3	0.5	0.01	0.01	2×10^{-3}	$0/-0.48$	$0/-0.47$	$1.57/-0.78$	$0/-10^{-4}$	$0/-10^{-4}$	$2.34/-1.18$
Case 4	10	0.01	0.05	0.13	$0/-0.03$	$0/-0.03$	$0/-10^{-4}$	$0/-10^{-3}$	$0/-10^{-3}$	$2.97/-1.66$

parallel ion-cyclotron wave in Regime II, and this wave has $\lambda_p k_\perp = 0.01$, $\lambda_p k_\parallel = 0.7$, and $\omega_r/\Omega_{\mathrm{cp}} \simeq 0.37$. Case 3 and Case 4 are examples of the quasi-perpendicular ion-scale Alfvén wave regime (Regime III) and the quasi-perpendicular sub-ion-scale Alfvén wave regime (Regime IV), respectively. The former has $\lambda_p k_\parallel = 0.01$, $\lambda_p k_\perp = 0.5$, and $\omega_r/\Omega_{\mathrm{cp}} \simeq 0.01$; the latter has $\lambda_p k_\parallel = 0.01$, $\lambda_p k_\perp = 10$, and $\omega_r/\Omega_{\mathrm{cp}} \simeq 0.05$.

We note that the subscript "1" for the first-order perturbations is ignored in the following discussions for simplicity, and the resonant/nonresonant energy transfer rate corresponds to the energy transfer resulting from resonant/nonresonant particles.

4.1. The Quasi-parallel MHD Alfvén Wave

The distributions of proton energy transfer rates P_p in Case 1 are presented in Figures 4 and 5, where 1D energy transfer rates are normalized by the corresponding maximum $P_{\mathrm{pt}}(v_\parallel)$ or maximum $P_{\mathrm{pt}}(v_\perp)$, and 2D energy transfer rates are normalized by the maximum $P_{\mathrm{pt}}(v_\parallel, v_\perp)$. The similar normalization method is used to prepare Figures 6–12.

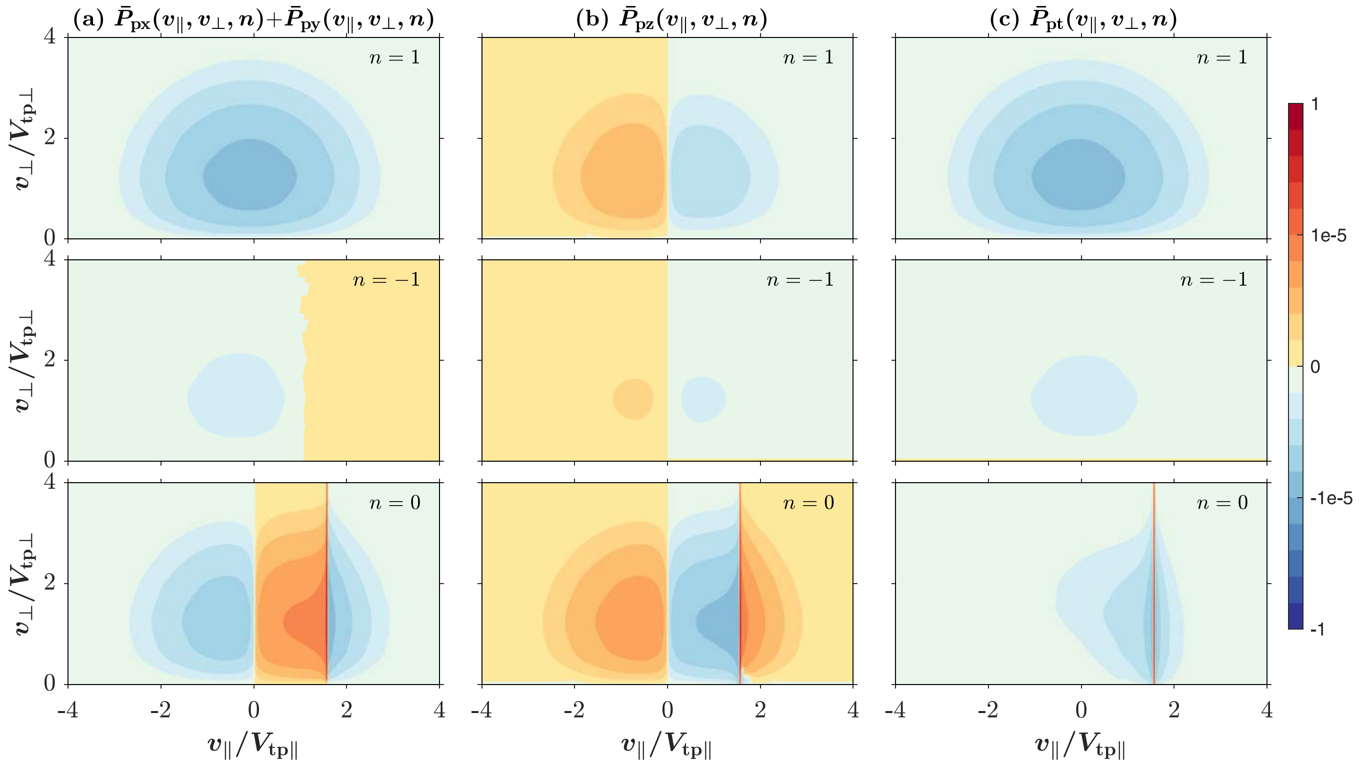

Figure 5. The $v_\parallel$−$v_\perp$ distributions of proton energy transfer rates at $n = \pm 1$ and $n = 0$ in Case 1: (a) the perpendicular energy transfer rate, $P_{\rm px} + P_{\rm py}$; (b) the parallel energy transfer rate, $P_{\rm pz}$; and (c) the total energy transfer rate, $P_{\rm pt}$. The data are normalized by the maximum $P_{\rm pt}$ in the $v_\parallel$−$v_\perp$ plane.

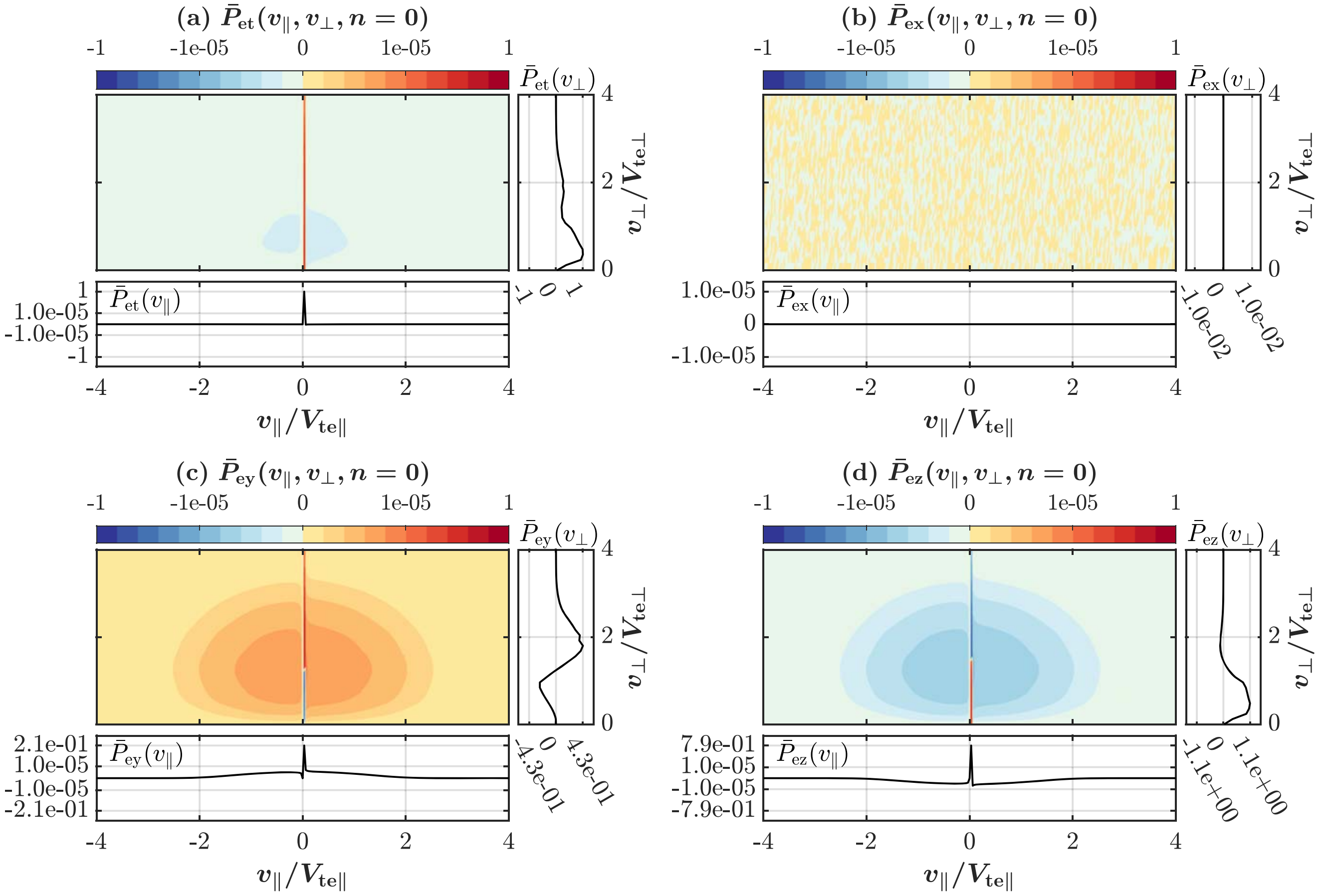

Figure 6. The 1D and 2D distributions of electron energy transfer rates at $n = 0$ in Case 1: (a) the total energy transfer rate, $P_{\rm et}$; (b) the x component of the energy transfer rate, $P_{\rm ex}$; (c) the $y$component of the energy transfer rate, $P_{\rm ey}$; and (d) the parallel energy transfer rate, $P_{\rm ez}$. The 2D energy transfer rates are normalized by the maximum $P_{\rm et}$ in the $v_\parallel$−$v_\perp$ plane. The 1D energy transfer rates are normalized by the corresponding maximum $P_{\rm et}(v_\parallel)$ or maximum $P_{\rm et}(v_\perp)$.

According to the resonant condition, $k_{\|}v_{\|} = \omega_r - n\Omega_{\rm cp}$, between the waves and protons, the proton resonant speed is approximately $1.6V_{\rm tp}$ at $n = 0$, $-18.9V_{\rm tp}$ at $n = 1$, and $18.0V_{\rm tp}$ at $n = -1$. Because the latter two resonant speeds are much larger than the proton thermal speed, the number of protons taking part in the $n = \pm1$ resonant wave–particle interactions is negligible, and this leads to a weak energy transfer, $P_p^r(n = \pm1)/(2|\gamma|) \sim 0$ (see Table 1). The $n = 0$ resonant wave–particle interaction controls the wave damping. The signatures of this wave–particle interaction (enhanced energy transfer rates at $v_{\|} = 1.6V_{\rm tp}$) are evident in the $P_{\rm py}(v_{\|}, v_{\perp})$ and $P_{\rm pz}(v_{\|}, v_{\perp})$ distributions (see Figures 4 and 5).

From Equations (C3) and (C4) in Appendix C, we give the analytical expressions of the $n = 0$ resonant energy transfer rates at the condition of $a_p \ll 1$,

$$P_{\rm py}^r(v_{\|}, v_{\perp}, n = 0) = \frac{\sqrt{\pi}\,\omega_{\rm pp}^2}{\Omega_{\rm cp}}\frac{k_{\perp}}{k_{\|}}\frac{v_{\perp}^4}{V_{\rm tp}^5}e^{-\frac{v_{\|}^2+v_{\perp}^2}{V_{\rm tp}^2}} \times \left[\frac{v_{\perp}}{V_A}\lambda_p k_{\perp} + 2\frac{v_{\|}}{v_{\perp}}\sin(\psi_{\widetilde{E}_y} - \psi_{\widetilde{E}_z})\frac{|\widetilde{E}_z|}{|\widetilde{E}_y|}\right] \times \frac{\epsilon_0|\widetilde{E}_y|^2}{W_{\rm EB}}\delta(v_{\|} - V_{\rm r0}) \tag{35}$$

and

$$P_{\rm pz}^r(v_{\|}, v_{\perp}, n = 0) = \frac{2\sqrt{\pi}\,\omega_{\rm pp}^2}{k_{\|}}\frac{v_{\|}v_{\perp}^2}{V_{\rm tp}^5}e^{-\frac{v_{\|}^2+v_{\perp}^2}{V_{\rm tp}^2}} \times \left[2\frac{v_{\|}}{v_{\perp}} - \frac{v_{\perp}}{V_A}\lambda_p k_{\perp}\sin(\psi_{\widetilde{E}_z} - \psi_{\widetilde{E}_y})\frac{|\widetilde{E}_y|}{|\widetilde{E}_z|}\right] \times \frac{\epsilon_0|\widetilde{E}_z|^2}{W_{\rm EB}}\delta(v_{\|} - V_{\rm r0}), \tag{36}$$

where $\omega_{\rm pp}$ is the proton plasma frequency, and $\psi_{\widetilde{E}_y} - \psi_{\widetilde{E}_z} \simeq 121°$ is the phase difference between $\widetilde{E}_y$ and $\widetilde{E}_z$ in Case 1. Due to $P_{\rm py}^r(n = 0) > 0$ and $P_{\rm pz}^r(n = 0) > 0$, the transit-time and Landau resonant interactions absorb energy from the quasi-parallel MHD Alfvén wave. Also, both $P_{\rm py}^r(n = 0)$ and $P_{\rm pz}^r(n = 0)$ depend on the proton perpendicular velocity $v_{\perp}$ (also see Figures 4(c) and 4(d)). Through a straightforward numerical calculation, we find the maximum $P_{\rm py}^r(n = 0)$ and $P_{\rm pz}^r(n = 0)$ occurring at $v_{\perp} \simeq 1.5V_{\rm tp}$ and $v_{\perp} \simeq 0.9V_{\rm tp}$, respectively, as shown in Figure 4.

Figures 4 and 5 also exhibit the signatures of wave–particle interactions of nonresonant particles. Here we will give a detailed explanation of these wave–particle interactions.

At first, we will explore the basic features of the energy transfer rate distributions resulting from the $n = 1$ wave–particle interactions. From Equations (C12) and (C13) in Appendix C, we obtain the following analytical expressions of nonresonant energy transfer rates at $n = 1$ and $a_p \ll 1$,

$$P_{\rm px}^{\rm nr}(v_{\|}, v_{\perp}, n = 1) = \frac{\omega_{\rm pp}^2}{2\sqrt{\pi}\,k_{\|}}\frac{v_{\perp}^3/V_{\rm tp}^5}{(v_{\|} - V_{\rm r1})^2 + (\gamma/k_{\|})^2} \times e^{-\frac{v_{\|}^2+v_{\perp}^2}{V_{\rm tp}^2}}\left\{\frac{\gamma}{k_{\|}} + \left[(v_{\|} - V_{\rm r1})\cos(\psi_{\widetilde{E}_x} - \psi_{\widetilde{E}_y}) + \frac{\gamma}{k_{\|}}\sin(\psi_{\widetilde{E}_x} - \psi_{\widetilde{E}_y})\right]\frac{|\widetilde{E}_y|}{|\widetilde{E}_x|}\right\}\frac{\epsilon_0|\widetilde{E}_x|^2}{W_{\rm EB}} \tag{37}$$

and

$$P_{\rm py}^{\rm nr}(v_{\|}, v_{\perp}, n = 1) = \frac{\omega_{\rm pp}^2}{2\sqrt{\pi}\,k_{\|}}\frac{v_{\perp}^3/V_{\rm tp}^5}{(v_{\|} - V_{\rm r1})^2 + (\gamma/k_{\|})^2} \times e^{-\frac{v_{\|}^2+v_{\perp}^2}{V_{\rm tp}^2}}\left\{\frac{\gamma}{k_{\|}} - \left[(v_{\|} - V_{\rm r1})\cos(\psi_{\widetilde{E}_y} - \psi_{\widetilde{E}_x}) + \frac{\gamma}{k_{\|}}\sin(\psi_{\widetilde{E}_y} - \psi_{\widetilde{E}_x})\right]\frac{|\widetilde{E}_x|}{|\widetilde{E}_y|}\right\}\frac{\epsilon_0|\widetilde{E}_y|^2}{W_{\rm EB}}, \tag{38}$$

where $\psi_{\widetilde{E}_x} - \psi_{\widetilde{E}_y} \simeq 89°$ is the phase difference between $\widetilde{E}_x$ and $\widetilde{E}_y$ in Case 1. We note that due to $|\widetilde{E}_z| \ll |\widetilde{E}_{\rm x,\,y}|$, the energy transfer rate in the parallel direction is much weaker than that in the perpendicular direction, and therefore, we do not analyze the features of $P_{\rm pz}^{\rm nr}(n = 1)$ in Case 1. In the velocity regime of $|v_{\|}| < 3V_{\rm tp}$, $(v_{\|} - V_{\rm r1}) \gg |\gamma/k_{\|}|$, and the terms related to $v_{\|} - V_{\rm r1}$ control the energy transfer. Consequently, $P_{\rm px}^{\rm nr}(n = 1)$ and $P_{\rm py}^{\rm nr}(n = 1)$ have opposite energy transfer directions, as shown in Figure 4. Actually, the source of these two dominant terms is the electric field drift of protons, and this drift results in $J_{px} \propto E_y$ and $J_{py} \propto -E_x$ which lead to the anticorrelation between $P_{\rm px}^{\rm nr}(n = 1)$ and $P_{\rm py}^{\rm nr}(n = 1)$. For the sum of $P_{\rm px}^{\rm nr}(n = 1)$ and $P_{\rm py}^{\rm nr}(n = 1)$, the two terms related to $v_{\|} - V_{\rm r1}$ are nearly canceled out, and only the terms associated with γ survive. Due to $P_{\rm px}^{\rm nr}(n = 1) + P_{\rm py}^{\rm nr}(n = 1) \propto \gamma < 0$, nonresonant protons emit energy, as shown in Figure 5.

Moreover, Equations (37) and (38) show that both $P_{\rm px}^{\rm nr}(n = 1)$ and $P_{\rm py}^{\rm nr}(n = 1)$ are nearly proportional to $\exp(-v_{\|}^2/V_{\rm tp}^2)/[(v_{\|} - V_{\rm r1})^2 + (\gamma/k_{\|})^2]$, and hence their maxima occur at $v_{\|} \simeq 0$ in the velocity regime of $|v_{\|}| < 3V_{\rm tp}$. Also, the two energy transfer rates are a function of $v_{\perp}^3\exp(-v_{\perp}^2/V_{\rm tp}^2)$, which indicates that the maxima appear at $v_{\perp} \simeq 1.2V_{\rm tp}$. These two predictions are consistent with the numerical results shown in Figures 4(b) and 4(c).

Second, in order to explain the distributions of proton energy transfer rates resulting from the $n = 0$ nonresonant wave–particle interactions, we give their analytical expressions in the limit of $a_p \ll 1$ from Equations (C5) and (C6) in Appendix C,

$$P_{\rm py}^{\rm nr}(v_\parallel, v_\perp, n=0) = \frac{\omega_{\rm pp}^2}{\sqrt{\pi}\,\Omega_{\rm cp}} \frac{(k_\perp/k_\parallel)(v_\perp^4/V_{\rm tp}^5)}{(v_\parallel - V_{\rm r0})^2 + (\gamma/k_\parallel)^2} \times e^{-\frac{v_\parallel^2+v_\perp^2}{V_{\rm tp}^2}} \left\{ \frac{1}{2}\frac{\gamma}{k_\parallel}\frac{v_\perp}{V_A}\lambda_p k_\perp + \frac{v_\parallel}{v_\perp}\left[\frac{\gamma}{k_\parallel}\sin(\psi_{\widetilde{E}_y} - \psi_{\widetilde{E}_z}) + (v_\parallel - V_{\rm r0})\cos(\psi_{\widetilde{E}_y} - \psi_{\widetilde{E}_z})\right]\frac{|\widetilde{E}_z|}{|\widetilde{E}_y|}\right\}\frac{\epsilon_0|\widetilde{E}_y|^2}{W_{\rm EB}} \tag{39}$$

and

$$P_{\rm pz}^{\rm nr}(v_\parallel, v_\perp, n=0) = \frac{\omega_{\rm pp}^2}{\sqrt{\pi}\,k_\parallel} \frac{v_\parallel v_\perp^2/V_{\rm tp}^5}{(v_\parallel - V_{\rm r0})^2 + (\gamma/k_\parallel)^2} \times e^{-\frac{v_\parallel^2+v_\perp^2}{V_{\rm tp}^2}} \left\{ 2\frac{\gamma}{k_\parallel}\frac{v_\parallel}{v_\perp} - \frac{v_\perp}{V_A}\lambda_p k_\perp\left[\frac{\gamma}{k_\parallel}\sin(\psi_{\widetilde{E}_z} - \psi_{\widetilde{E}_y}) + (v_\parallel - V_{\rm r0})\cos(\psi_{\widetilde{E}_z} - \psi_{\widetilde{E}_y})\right]\frac{|\widetilde{E}_y|}{|\widetilde{E}_z|}\right\}\frac{\epsilon_0|\widetilde{E}_z|^2}{W_{\rm EB}}. \tag{40}$$

In the velocity regime of $|v_\parallel - V_{\rm r0}| \gg |\gamma/k_\parallel|$, the terms related to $(v_\parallel - V_{\rm r0})$ dominate $P_{\rm py}^{\rm nr}(n=0)$ and $P_{\rm pz}^{\rm nr}(n=0)$, and they make these two energy transfer rates having opposite directions (see Figure 5). Also, both $P_{\rm py}^{\rm nr}(n=0)$ and $P_{\rm pz}^{\rm nr}(n=0)$ are proportional to $v_\parallel(v_\parallel - V_{\rm r0})$, and thus their signs change at the positions of $v_\parallel = 0$ and $v_\parallel = V_{\rm r0}$. From the $P_{\rm pz}^{\rm nr}(n=0)$ distribution shown by Figure 5, we can see protons with $v_\parallel \gtrsim V_{\rm r0} = 1.6V_{\rm tp}$ releasing energy and protons with $0 < v_\parallel \lesssim V_{\rm r0}$ absorbing energy. Moreover, for protons streaming opposite to the background magnetic field ($v_\parallel < 0$), they release energy. Furthermore, the sum of $P_{\rm py}^{\rm nr}(n=0)$ and $P_{\rm pz}^{\rm nr}(n=0)$ is proportional to γ, and this indicates that nonresonant protons release energy, similarly to the energy transfer induced by the $n=1$ nonresonant wave–particle interactions.

Similar to Figure 4, the distributions of electron energy transfer rates are presented in Figure 6. These distributions can be well understood by analyzing their analytical expressions. We note that the $n=\pm1$ interactions between electrons and low-frequency Alfvén waves are extremely weak due to the electron resonant speed $v_\parallel = (\omega_r \pm \Omega_{\rm ce})/k_\parallel \simeq \mp 700V_{\rm te}$ being much larger than the electron thermal speed $V_{\rm te}$, hence Figure 6 exhibits energy transfer rates at $n=0$.

From Equations (C3) and (C4) in Appendix C, the analytical expressions of resonant electron energy transfer rates are given by

$$P_{\rm ey}^{r}(v_\parallel, v_\perp, n=0) = \frac{\sqrt{\pi}\,\omega_{\rm pe}^2}{|\Omega_{\rm ce}|}\frac{k_\perp}{k_\parallel}\frac{v_\perp^4}{V_{\rm te}^5}e^{-\frac{v_\parallel^2+v_\perp^2}{V_{\rm te}^2}} \times \left[\frac{m_e}{m_p}\frac{v_\perp}{V_A}\lambda_p k_\perp - 2\frac{v_\parallel}{v_\perp}\sin(\psi_{\widetilde{E}_y} - \psi_{\widetilde{E}_z})\frac{|\widetilde{E}_z|}{|\widetilde{E}_y|}\right] \times \frac{\epsilon_0|\widetilde{E}_y|^2}{W_{\rm EB}}\delta(v_\parallel - V_{\rm r0}) \tag{41}$$

and

$$P_{\rm ez}^{r}(v_\parallel, v_\perp, n=0) = \frac{2\sqrt{\pi}\,\omega_{\rm pe}^2}{k_\parallel}\frac{v_\parallel v_\perp^2}{V_{\rm te}^5}e^{-\frac{v_\parallel^2+v_\perp^2}{V_{\rm te}^2}} \times \left[2\frac{v_\parallel}{v_\perp} + \frac{m_e}{m_p}\frac{v_\perp}{V_A}\lambda_p k_\perp\sin(\psi_{\widetilde{E}_z} - \psi_{\widetilde{E}_y})\frac{|\widetilde{E}_y|}{|\widetilde{E}_z|}\right] \times \frac{\epsilon_0|\widetilde{E}_z|^2}{W_{\rm EB}}\delta(v_\parallel - V_{\rm r0}), \tag{42}$$

where $V_{\rm r0} \simeq 0.036V_{\rm te}$ is the electron resonant speed at $n=0$. The signatures of electron resonant wave–particle interactions at $V_{\rm r0} \simeq 0.036V_{\rm te}$ are evident in Figure 6. Also, the two terms in square brackets in both $P_{\rm ey}^{r}(n=0)$ and $P_{\rm ez}^{r}(n=0)$ have opposite signs. With increasing $v_\perp$, $P_{\rm ey}^{r}(n=0)$ becomes positive from negative value, and $P_{\rm ez}^{r}(n=0)$ turns to negative from positive value. The transition point corresponds to $v_\perp = [2(m_p/m_e)(V_{\rm r0}V_A/\lambda_p k_\perp)\sin(\psi_{\widetilde{E}_y} - \psi_{\widetilde{E}_z})(|\widetilde{E}_z|/|\widetilde{E}_y|)]^{1/2} \sim V_{\rm te}$ in Case 1. These theoretical predictions can be identified in Figure 6. In addition, the sum of $P_{\rm ey}^{r}(n=0)$ and $P_{\rm ez}^{r}(n=0)$ shown in Figure 6(a) is always larger than zero at arbitrary $v_\perp$, indicating that electrons absorb energy from the quasi-parallel MHD Alfvén wave.

Nonresonant electron energy transfer rates at $n=0$ are analytically given by

$$P_{\rm ey}^{\rm nr}(v_\parallel, v_\perp, n=0) = \frac{\omega_{\rm pe}^2}{\sqrt{\pi}\,|\Omega_{\rm ce}|}\frac{(k_\perp/k_\parallel)(v_\perp^4/V_{\rm te}^5)}{(v_\parallel - V_{\rm r0})^2 + (\gamma/k_\parallel)^2} \times e^{-\frac{v_\parallel^2+v_\perp^2}{V_{\rm te}^2}}\left\{\frac{1}{2}\frac{\gamma}{k_\parallel}\frac{m_e}{m_p}\frac{v_\perp}{V_A}\lambda_p k_\perp - \frac{v_\parallel}{v_\perp}\left[(v_\parallel - V_{\rm r0}) \times \cos(\psi_{\widetilde{E}_y} - \psi_{\widetilde{E}_z}) + \frac{\gamma}{k_\parallel}\sin(\psi_{\widetilde{E}_y} - \psi_{\widetilde{E}_z})\right]\frac{|\widetilde{E}_z|}{|\widetilde{E}_y|}\right\} \times \frac{\epsilon_0|\widetilde{E}_y|^2}{W_{\rm EB}} \tag{43}$$

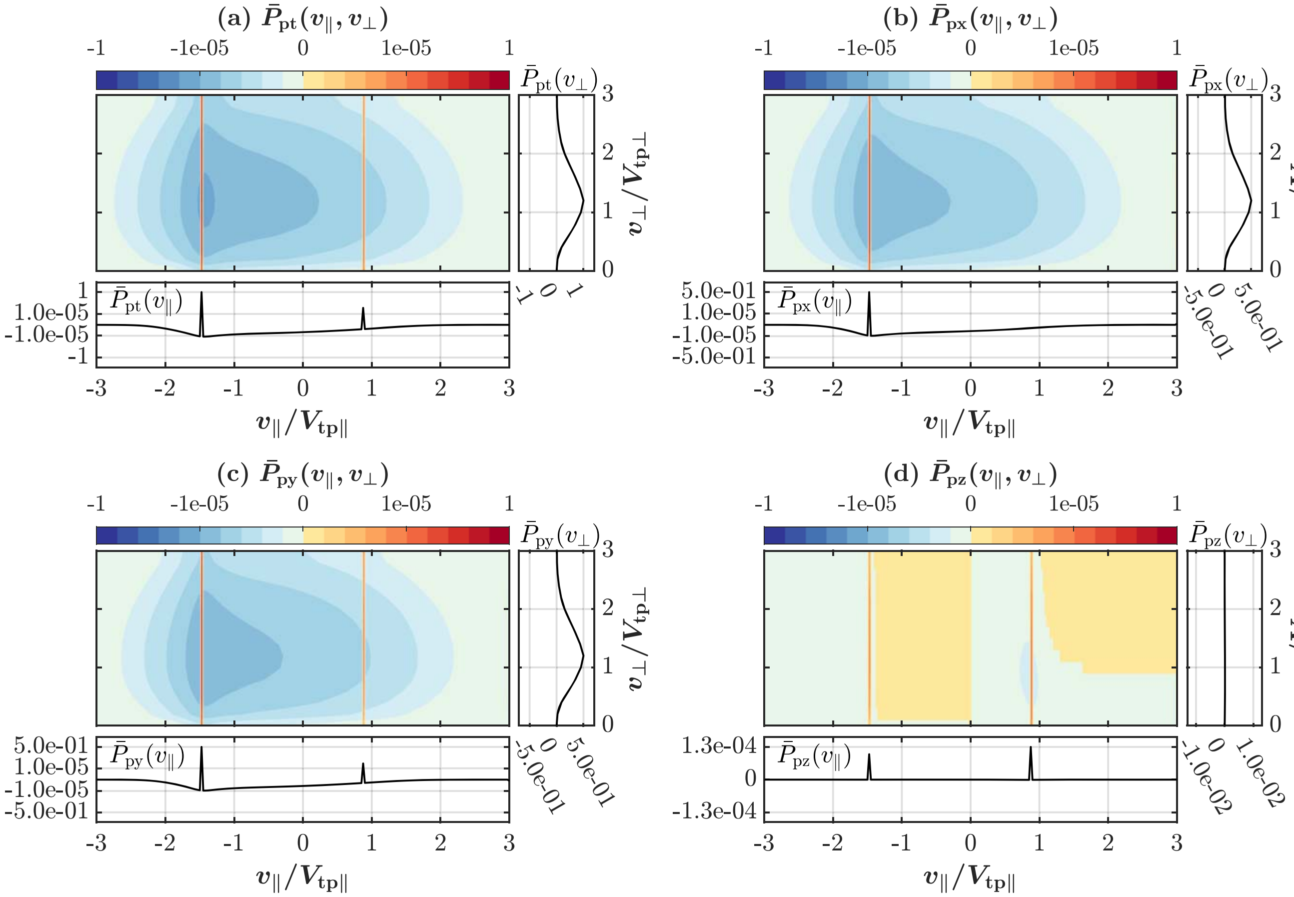

Figure 7. The 1D and 2D distributions of proton energy transfer rates in Case 2 where $\lambda_p k_\perp = 0.01$ and $\lambda_p k_\parallel = 0.7$. The description of panels (a)−(d) is the same as that in Figure 4.

and

$$P_{ez}^{nr}(v_\parallel, v_\perp, n=0) = \frac{\omega_{pe}^2}{\sqrt{\pi}k_\parallel}\frac{v_\parallel v_\perp^2/V_{te}^5}{(v_\parallel - V_{r0})^2 + (\gamma/k_\parallel)^2} \times e^{-\frac{v_\parallel^2+v_\perp^2}{V_{te}^2}}\left\{2\frac{\gamma}{k_\parallel}\frac{v_\parallel}{v_\perp} + \frac{m_e}{m_p}\frac{v_\perp}{V_A}\lambda_p k_\perp\left[(v_\parallel - V_{r0}) \times \cos(\psi_{\widetilde{E}_z} - \psi_{\widetilde{E}_y}) + \frac{\gamma}{k_\parallel}\sin(\psi_{\widetilde{E}_z} - \psi_{\widetilde{E}_y})\right]\frac{|\widetilde{E}_y|}{|\widetilde{E}_z|}\right\} \times \frac{\epsilon_0|\widetilde{E}_z|^2}{W_{EB}}. \quad (44)$$

In the velocity regime of $|v_\parallel - V_{r0}| \gg |\gamma/k_\parallel|$, the terms related to $(v_\parallel - V_{r0})$ control the $P_{ey}^{nr}(n=0)$ and $P_{ez}^{nr}(n=0)$ distributions, which result in $P_{ey}^{nr}(n=0) > 0$ and $P_{ez}^{nr}(n=0) < 0$. Similar to the proton case, these two dominant terms actually come from the electric field drift of electrons. They are totally canceled out in summing $P_{ey}^{nr}(n=0)$ and $P_{ez}^{nr}(n=0)$, and the major contributions of $P_{ey}^{nr}(n=0) + P_{ez}^{nr}(n=0)$ are the terms related to γ. Furthermore, shown by Figure 6, $P_{ey}^{nr}(n=0) + P_{ez}^{nr}(n=0) < 0$, and this means the $n = 0$ nonresonant wave–particle interactions lead to electrons releasing energy.

4.2. The Quasi-parallel Ion-cyclotron Wave

Figures 7 and 8 present the distributions of proton energy transfer rates in Case 2.

According to the resonant condition, the proton resonant speeds occur at $v_\parallel \simeq -1.5\,V_{tp}$ at $n = 1$ and $0.9V_{tp}$ at $n = 0$. The $n = 1$ cyclotron resonant interactions control the wave damping. The $n = 0$ resonant interactions contribute to only ∼0.1% of the wave damping (see Table 1). Hence, here we only analyze the $n = 1$ cyclotron resonant interaction. Using Equations (C8) and (C9) in Appendix C and considering $a_p \ll 1$, the $n = 1$ resonant proton energy transfer rates are written as

$$P_{px}^{r}(v_\parallel, v_\perp, n=1) = \frac{\sqrt{\pi}\omega_{pp}^2}{k_\parallel}\frac{v_\perp^3}{V_{tp}^5}e^{-\frac{v_\parallel^2+v_\perp^2}{V_{tp}^2}}\left[1 + \sin(\psi_{\widetilde{E}_x} - \psi_{\widetilde{E}_y})\frac{|\widetilde{E}_y|}{|\widetilde{E}_x|}\right]\frac{\epsilon_0|\widetilde{E}_x|^2}{W_{EB}}\delta(v_\parallel - V_{r1}) \quad (45)$$

and

$$P_{py}^{r}(v_\parallel, v_\perp, n=1) = \frac{\sqrt{\pi}\omega_{pp}^2}{k_\parallel}\frac{v_\perp^3}{V_{tp}^5}e^{-\frac{v_\parallel^2+v_\perp^2}{V_{tp}^2}}\left[1 - \sin(\psi_{\widetilde{E}_y} - \psi_{\widetilde{E}_x})\frac{|\widetilde{E}_x|}{|\widetilde{E}_y|}\right]\frac{\epsilon_0|\widetilde{E}_y|^2}{W_{EB}}\delta(v_\parallel - V_{r1}), \quad (46)$$

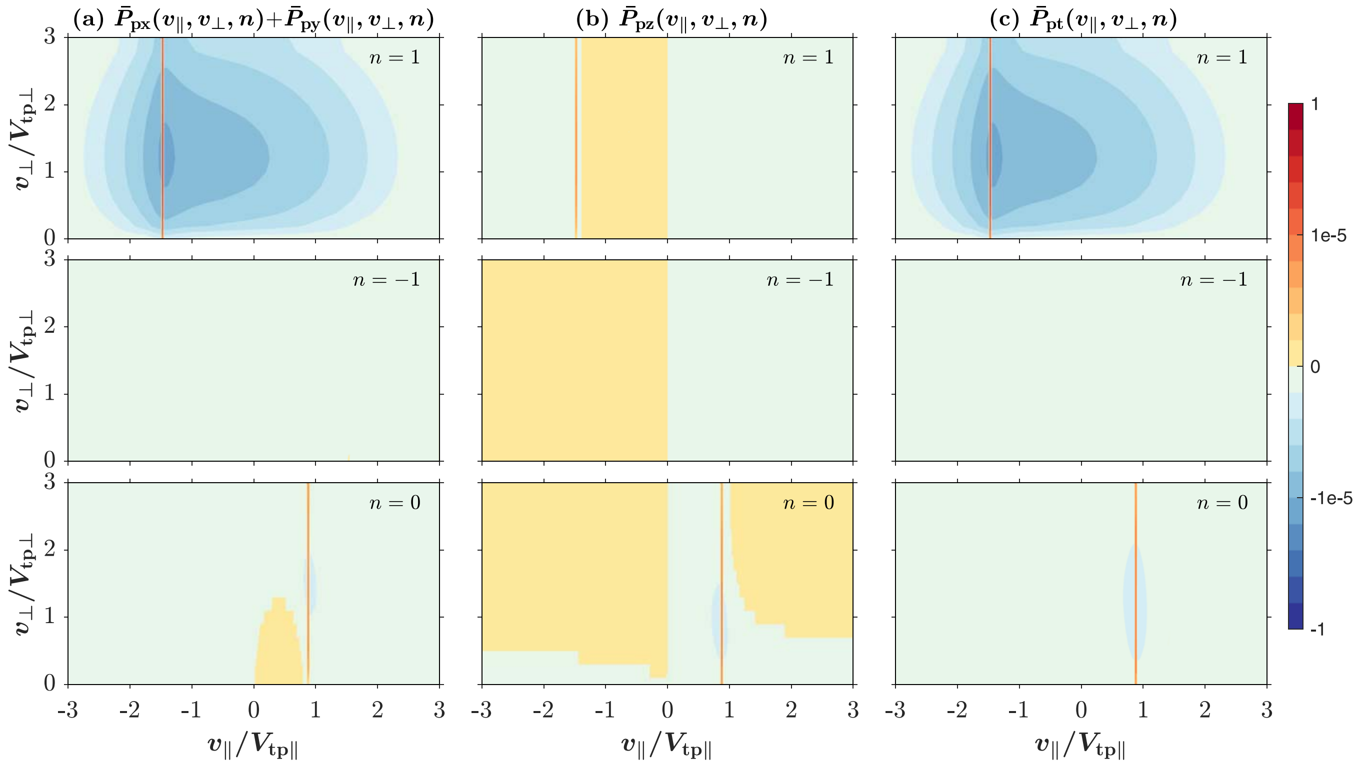

Figure 8. The $v_\parallel$–$v_\perp$ distributions of proton energy transfer rates at $n = \pm 1$ and $n = 0$ in Case 2. The description of the panels in this figure is the same as that in Figure 5.

where $\psi_{\widetilde{E}_x} - \psi_{\widetilde{E}_y} \simeq 90°$ and $V_{\rm r1} = -1.5 V_{\rm tp}$ in Case 2. Because both $P_{\rm px}^r$ and $P_{\rm py}^r$ are always larger than zero, the protons continuously absorb energy from this quasi-parallel ion-cyclotron wave through the $n = 1$ cyclotron resonant interactions.

For proton energy transfer rates induced by the $n = 1$ nonresonant wave–particle interactions, their analytical expressions are the same as those given in Equations (37) and (38). Due to $\cos(\psi_{\widetilde{E}_x} - \psi_{\widetilde{E}_y}) \simeq 0$ in Case 2, both $P_{\rm px}^{\rm nr}(v_\parallel, v_\perp, n = 1)$ and $P_{\rm py}^{\rm nr}(v_\parallel, v_\perp, n = 1)$ are proportional to γ. As a consequence, they release energy, and the magnitude of this energy emission is nearly six times the wave-damping rate (see Table 1). On the other hand, because both perpendicular energy transfer rates are nearly proportional to $\exp(-v_\parallel^2/V_{\rm tp}^2)/[(v_\parallel - V_{\rm r1})^2 + (\gamma/k_\parallel)^2] \times [v_\perp^3 \exp(-v_\perp^2/V_{\rm tp}^2)]$ in Case 2, the strongest energy transfer arises at $v_\parallel \simeq V_{\rm r1}$ and $v_\perp \simeq 1.2 V_{\rm tp}$, as shown in Figures 7 and 8.

4.3. The Quasi-perpendicular Ion-scale Alfvén Wave

Figures 9 and 10 present the distributions of proton energy transfer rates in Case 3.

At first, we explain the distributions of energy transfer rates induced by resonant wave–particle interactions. Considering $\omega_r/\Omega_{\rm cp} \simeq 0.01$ and $\lambda_p k_\parallel = 0.01$, the $n = 0$ resonant interactions arise at $v_\parallel \simeq 1.67 V_{\rm tp}$, and the $n = \pm 1$ resonant interactions appear at $|v_\parallel| \simeq 160 V_{\rm tp}$. Therefore, the n=0 wave–particle interaction controls the wave damping. In order to compare all sources responsible for the $n = 0$ resonant proton energy transfer rate, we rewrite Equations (C3) and (C4) in Appendix C as

$$P_{\rm py}^r(n = 0) \propto -v_\perp J_0'(a_p)|\widetilde{E}_y|^2 + v_\parallel J_0(a_p)\sin(\psi_{\widetilde{E}_y} - \psi_{\widetilde{E}_z})|\widetilde{E}_y||\widetilde{E}_z| \tag{47}$$

and

$$P_{\rm pz}^r(n = 0) \propto v_\perp J_0'(a_p)\sin(\psi_{\widetilde{E}_z} - \psi_{\widetilde{E}_y})|\widetilde{E}_z||\widetilde{E}_y| + v_\parallel J_0(a_p)|\widetilde{E}_z|^2. \tag{48}$$

Due to $\psi_{\widetilde{E}_y} - \psi_{\widetilde{E}_z} \simeq -80°$ in Case 3 and $J_0'(a_p) < 0$, the terms including $|\widetilde{E}_y||\widetilde{E}_z|$ are smaller than zero, and the other two terms (related to $|\widetilde{E}_y|^2$ and $|\widetilde{E}_z|^2$) are larger than zero. As a consequence, with increasing $v_\perp$, $P_{\rm py}^r(n = 0)$ changes from negative to positive value, while $P_{\rm pz}^r(n = 0)$ changes from positive to negative value. However, the total of $P_{\rm py}^r(n = 0)$ and $P_{\rm pz}^r(n = 0)$ is always positive, independent of $v_\perp$, as shown in Figure 9.

Second, we explain the distributions of nonresonant proton energy transfer rates.

Because the wave in Case 3 approximates a linearly polarized mode wave ($|\widetilde{E}_x| \simeq 319|\widetilde{E}_y|$), this leads to the appearance of both $n = 1$ and $n = -1$ nonresonant wave–particle interactions (see Table 1 and Figure 9). In order to exhibit the basic features of the $n = \pm 1$ nonresonant wave–particle interactions, we retain the main effects in Equations (C12)–(C14) in Appendix C and rewrite

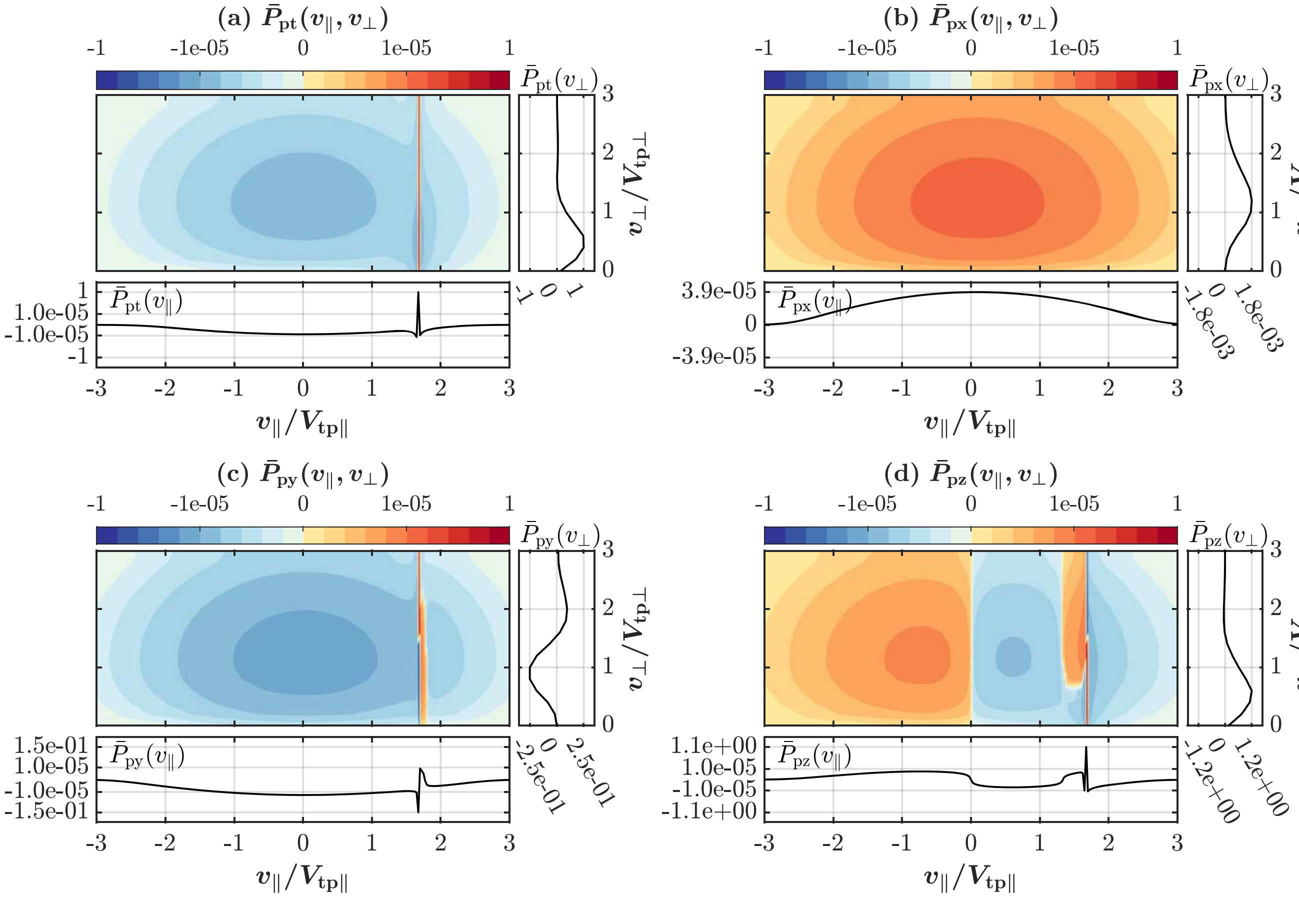

Figure 9. The 1D and 2D distributions of proton energy transfer rates in Case 3, where $\lambda_p k_\parallel = 0.01$ and $\lambda_p k_\perp = 0.5$. The description of panels (a)–(d) is the same as that in Figure 4.

nonresonant energy transfer rates as

$$P^{\rm nr}_{\rm px}(v_\parallel, v_\perp, n=1) + P^{\rm nr}_{\rm py}(v_\parallel, v_\perp, n=1) \simeq \frac{2\omega_{\rm pp}^2\Omega_{\rm cp}}{\sqrt{\pi}k_\parallel k_\perp} \times \frac{J_1(a_p)v_\perp^2/V_{\rm tp}^5}{(v_\parallel - V_{\rm r1})^2 + (\gamma/k_\parallel)^2} e^{-\frac{v_\parallel^2+v_\perp^2}{V_{\rm tp}^2}} \left[\frac{\gamma}{k_\parallel}\frac{J_1(a_p)}{a_p}\frac{\epsilon_0|\widetilde{E}_x|^2}{W_{\rm EB}} - \frac{v_\parallel}{v_\perp}(v_\parallel - V_{\rm r1})J_1(a_p)\sin(\psi_{\widetilde{E}_x} - \psi_{\widetilde{E}_z})\frac{\epsilon_0|\widetilde{E}_x||\widetilde{E}_z|}{W_{\rm EB}}\right] \tag{49}$$

and

$$P^{\rm nr}_{\rm pz}(v_\parallel, v_\perp, n=1) \simeq -\frac{2\omega_{\rm pp}^2\Omega_{\rm cp}}{\sqrt{\pi}k_\parallel k_\perp}\frac{[J_1(a_p)]^2 v_\parallel v_\perp/V_{\rm tp}^5}{(v_\parallel - V_{\rm r1})^2 + (\gamma/k_\parallel)^2} \times e^{-\frac{v_\parallel^2+v_\perp^2}{V_{\rm tp}^2}}\left[(v_\parallel - V_{\rm r1})\sin(\psi_{\widetilde{E}_z} - \psi_{\widetilde{E}_x}) - \frac{\gamma}{k_\parallel} \times \cos(\psi_{\widetilde{E}_z} - \psi_{\widetilde{E}_x})\right]\frac{\epsilon_0|\widetilde{E}_z||\widetilde{E}_x|}{W_{\rm EB}}, \tag{50}$$

where $\psi_{\widetilde{E}_z} - \psi_{\widetilde{E}_x} = 167°$. In the regime of $|v_\parallel| \leqslant 3V_{\rm tp}$, the terms related to $(v_\parallel - V_{\rm r1})\sin(\psi_{\widetilde{E}_x} - \psi_{\widetilde{E}_z})$ control both perpendicular and parallel energy transfer rates. However, these two terms are canceled out in the total energy transfer rate $P^{\rm nr}_{\rm pt}(v_\parallel, v_\perp, n=1)$, and the term related to $\gamma|\widetilde{E}_x|^2$ controls the energy transfer. Therefore, as shown in Figure 10, the total $n = 1$ nonresonant energy transfer rate is negative in the whole $v_\parallel$–$v_\perp$ space, in which nonresonant protons emit energy.

Similar to nonresonant energy transfer rates at $n = 1$, nonresonant energy transfer rates at $n = -1$ are given as

$$P^{\rm nr}_{\rm px}(v_\parallel, v_\perp, n=-1) + P^{\rm nr}_{\rm py}(v_\parallel, v_\perp, n=-1) \simeq \frac{2\omega_{\rm pp}^2\Omega_{\rm cp}}{\sqrt{\pi}k_\parallel k_\perp} \times \frac{J_1(a_p)v_\perp^2/V_{\rm tp}^5}{(v_\parallel - V_{\rm r-1})^2 + (\gamma/k_\parallel)^2} e^{-\frac{v_\parallel^2+v_\perp^2}{V_{\rm tp}^2}} \left[\frac{\gamma}{k_\parallel}\frac{J_1(a_p)}{a_p}\frac{\epsilon_0|\widetilde{E}_x|^2}{W_{\rm EB}} + \frac{v_\parallel}{v_\perp}(v_\parallel - V_{\rm r-1})J_1(a_p)\sin(\psi_{\widetilde{E}_x} - \psi_{\widetilde{E}_z})\frac{\epsilon_0|\widetilde{E}_x||\widetilde{E}_z|}{W_{\rm EB}}\right]$$

and

$$P^{\rm nr}_{\rm pz}(v_\parallel, v_\perp, n=-1) \simeq \frac{2\omega_{\rm pp}^2\Omega_{\rm cp}}{\sqrt{\pi}k_\parallel k_\perp}\frac{[J_1(a_p)]^2 v_\parallel v_\perp/V_{\rm tp}^5}{(v_\parallel - V_{\rm r-1})^2 + (\gamma/k_\parallel)^2} \times e^{-\frac{v_\parallel^2+v_\perp^2}{V_{\rm tp}^2}}\left[(v_\parallel - V_{\rm r-1})\sin(\psi_{\widetilde{E}_z} - \psi_{\widetilde{E}_x}) - \frac{\gamma}{k_\parallel} \times \cos(\psi_{\widetilde{E}_z} - \psi_{\widetilde{E}_x})\right]\frac{\epsilon_0|\widetilde{E}_z||\widetilde{E}_x|}{W_{\rm EB}}. \tag{52}$$

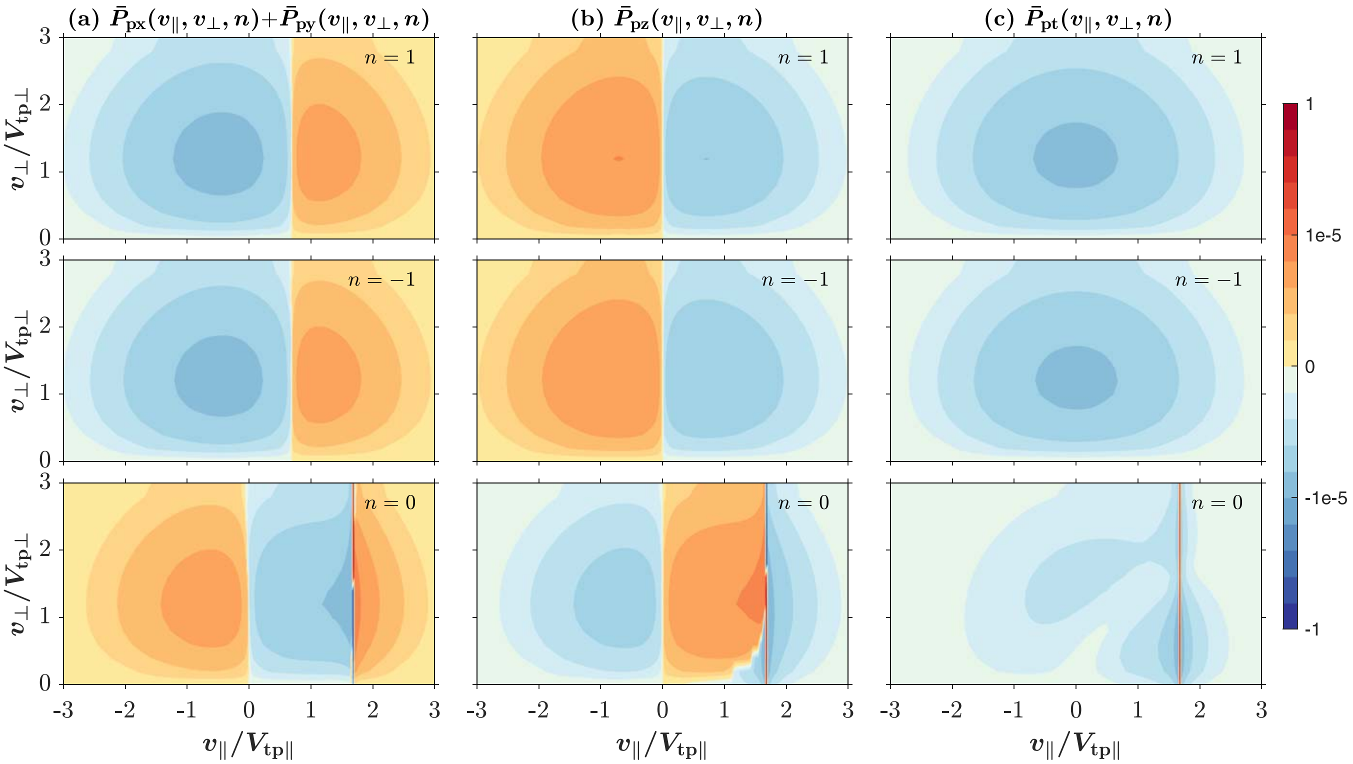

Figure 10. The $v_\parallel$–$v_\perp$ distributions of proton energy transfer rates at $n = \pm 1$ and $n = 0$ in Case 3. The description of the panels in this figure is the same as that in Figure 5.

where the relation $J_{-1}(a_p) = -J_1(a_p)$ is used. Considering $v_\parallel - V_{r-1} \simeq -V_{r1}$ at the condition of $|v_\parallel| \leqslant 3V_{\rm tp}$, nonresonant energy transfer rates at $n = -1$ would have the same distribution as that at $n = 1$, as shown by Figure 10.

For nonresonant proton energy transfer rates at $n = 0$, their analytical expressions in the region of $|v - V_{\rm r0}| \gg |\gamma/k_\parallel|$ are approximately given by

$$P_{\rm py}^{\rm nr}(v_\parallel, v_\perp, n = 0) = \frac{2\omega_{\rm pp}^2}{\sqrt{\pi}k_\parallel}\frac{J_0'(a_p)v_\perp^3/V_{\rm tp}^5}{(v_\parallel - V_{\rm r0})^2 + (\gamma/k_\parallel)^2} \times e^{-\frac{v_\parallel^2+v_\perp^2}{V_{\rm tp}^2}}\left[\frac{\gamma}{k_\parallel}J_0'(a_p) - \frac{v_\parallel}{v_\perp}(v_\parallel - V_{\rm r0})J_0(a_p) \times \cos(\psi_{\widetilde{E}_y} - \psi_{\widetilde{E}_z})\frac{|\widetilde{E}_z|}{|\widetilde{E}_y|}\right]\frac{\epsilon_0|\widetilde{E}_y|^2}{W_{\rm EB}} \tag{53}$$

and

$$P_{\rm pz}^{\rm nr}(v_\parallel, v_\perp, n = 0) = \frac{2\omega_{\rm pp}^2}{\sqrt{\pi}k_\parallel}\frac{J_0(a_p)v_\parallel v_\perp^2/V_{\rm tp}^5}{(v_\parallel - V_{\rm r0})^2 + (\gamma/k_\parallel)^2} \times e^{-\frac{v_\parallel^2+v_\perp^2}{V_{\rm tp}^2}}\left[\frac{\gamma}{k_\parallel}\frac{v_\parallel}{v_\perp}J_0(a_p) + (v_\parallel - V_{\rm r0})J_0'(a_p) \times \cos(\psi_{\widetilde{E}_z} - \psi_{\widetilde{E}_y})\frac{|\widetilde{E}_y|}{|\widetilde{E}_z|}\right]\frac{\epsilon_0|\widetilde{E}_z|^2}{W_{\rm EB}}, \tag{54}$$

where $\psi_{\widetilde{E}_z} - \psi_{\widetilde{E}_y} \simeq 81°$. Both $P_{\rm py}^{\rm nr}(n = 0)$ and $P_{\rm pz}^{\rm nr}(n = 0)$ are dominated by the terms related to $|\widetilde{E}_y||\widetilde{E}_z|$. Consequently, $P_{\rm py}^{\rm nr}(n = 0) \propto v_\parallel(v_\parallel - V_{\rm r0})$ and $P_{\rm pz}^{\rm nr}(n = 0) \propto -v_\parallel(v_\parallel - V_{\rm r0})$, which results in opposite signs of $P_{\rm py}^{\rm nr}(n = 0)$ and $P_{\rm pz}^{\rm nr}(n = 0)$. Compared to the $n = 0$ nonresonant energy transfer rates in Case 1, a major difference is the different phase relation between $\widetilde{E}_y$ and $\widetilde{E}_z$, and this leads to the signs of both $P_{\rm py}^{\rm nr}(n = 0)$ and $P_{\rm pz}^{\rm nr}(n = 0)$ in Case 3 being nearly opposite to that in Case 1. The other two terms in $P_{\rm py}^{\rm nr}(n = 0)$ and $P_{\rm pz}^{\rm nr}(n = 0)$ are proportional to γ, and they are releasing energy. Furthermore, the total $n = 0$ nonresonant energy transfer rate $P_{\rm py}^{\rm nr}(n = 0) + P_{\rm pz}^{\rm nr}(n = 0)$ is negative, as shown in Figure 10.

Figure 11 shows the distributions of electron energy transfer rates at $n = 0$. Due to $|a_e| \sim k_\perp V_{\rm te}/|\Omega_{\rm ce}| \simeq \lambda_p k_\perp \sqrt{\beta_e}\sqrt{m_e/m_p} \ll 1$, the analytical expressions of resonant and nonresonant energy transfer rates are the same as that given in Equations (41)–(44). Due to $\psi_{\widetilde{E}_z} - \psi_{\widetilde{E}_y} \simeq 81°$ in Case 3, both $P_{\rm ey}^r(n = 0)$ and $P_{\rm ez}^r(n = 0)$ are always positive, and $P_{\rm ey}^{\rm nr}(n = 0) < 0$ and $P_{\rm ez}^{\rm nr}(n = 0) > 0$ appear in the regime of $|v_\parallel - V_{\rm r0}| \gg |\gamma/k_\parallel|$. In addition, the total of $P_{\rm ey}^{\rm nr}(n = 0)$ and $P_{\rm ez}^{\rm nr}(n = 0)$ is proportional to γ, indicating that nonresonant electrons release energy. These results are shown in Figure 11.

4.4. The Quasi-perpendicular Sub-ion-scale Alfvén Wave

According to Figure 3 and Table 1, the $n = 0$ wave–particle interaction controls the damping of quasi-perpendicular sub-ion Alfvén waves, so here we only present the distributions of electron energy transfer rates at $n = 0$ in Case 4, shown by Figure 12, in which the $n = 0$ resonant wave–particle interaction occurs at $v_\parallel \simeq 0.2V_{\rm te}$.

Because $\lambda_e k_\perp \sim 0.1$ in Case 4, the analytical expressions (41)–(44) can describe well the electron energy transfer rate distribution in Figure 12. Similar to the explanations of

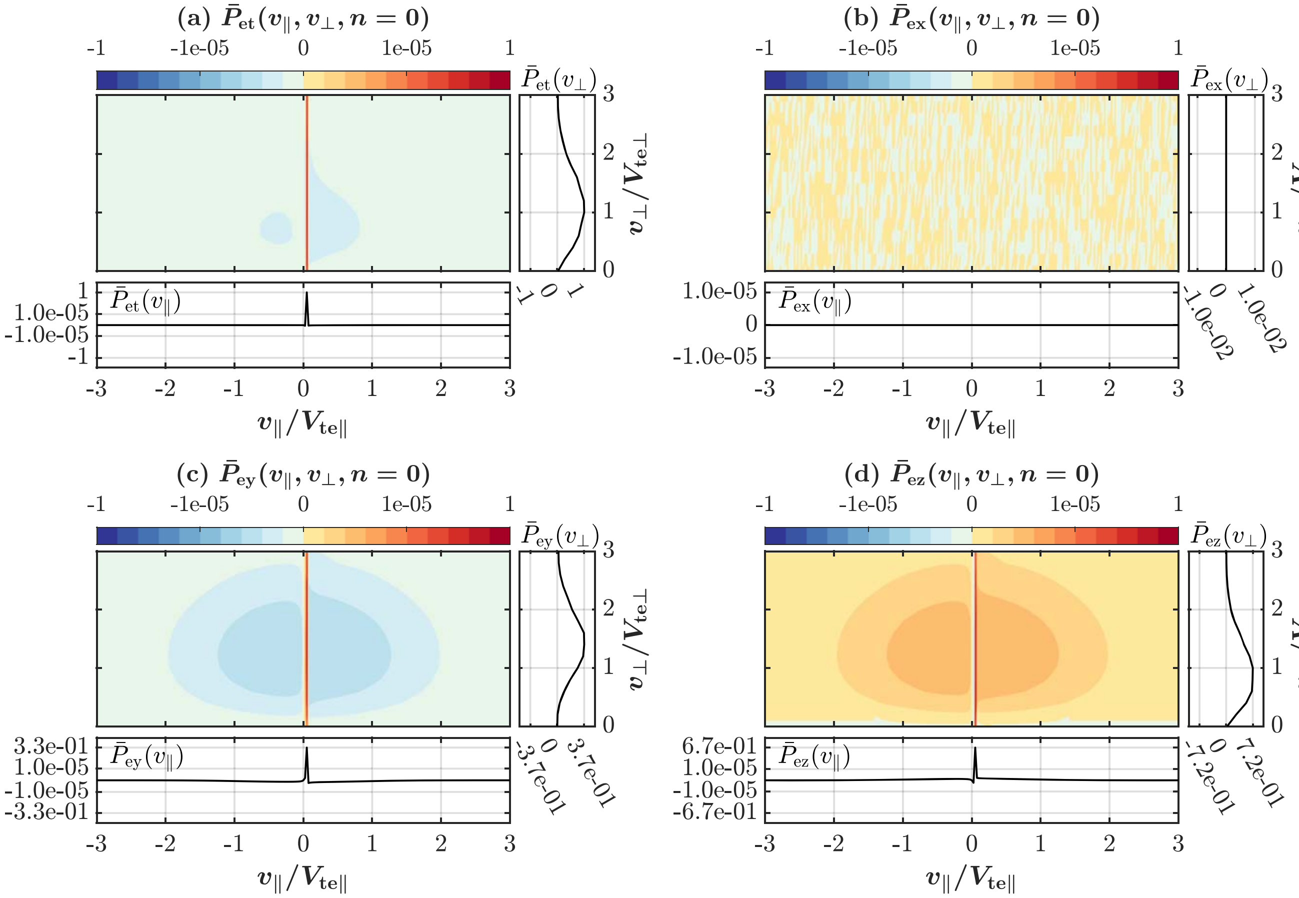

Figure 11. The 1D and 2D distributions of electron energy transfer rates at $n = 0$ in Case 3. The description of panels (a)–(d) is the same as that in Figure 6.

Figure 11, the same arguments are applicable for explaining Figure 12. It should be pointed out that because the $|\widetilde{E}_z|^2$ term dominates $P_{\rm ez}^{\rm nr}$ at small $v_\perp$, there is a negative $P_{\rm ez}^{\rm nr}$ in the velocity regime of $v_\perp \lesssim V_{\rm te}$.

Further, the quasi-perpendicular sub-ion-scale Alfvén wave would encounter the $n = \pm 1$ nonresonant wave–proton interactions, and energy transfer rates are about $P_p^{\rm nr}(n = \pm 1)/2 \simeq -0.03|\gamma|$. We note that there exist high-order n ($|n| > 1$) nonresonant wave–particle interactions of the sub-ion-scale Alfvén wave, and these interactions can also induce energy to be released from nonresonant protons.

5. Discussion

5.1. Energy Transfer: Resonant Particles and Nonresonant Particles

One of interesting findings in this paper is that the energy transfer directions are normally opposite in wave–particle interactions between Alfvén-mode waves and resonant/nonresonant particles. Resonant particles absorb energy, and nonresonant particles emit energy. Therefore, the particle velocity distribution function can be self-regulated during the damping of the Alfvén-mode wave. Because linear resonant wave–particle interactions occur at resonant speeds, these interactions only energize the particles with velocities at the resonant speed. Linear wave–particle interactions of nonresonant particles become strong around the resonant speed and/or around $v_\parallel \sim 0$, and consequently, nonresonant particles will effectively lose their kinetic energy around these two characteristic velocities.

We note that the same behavior of the energy transfer induced by resonant and nonresonant particles was found in the system consisting of electrons and electron plasma oscillations (Drummond & Pines 1962; Vedenov et al. 1962; Sagdeev & Galeev 1969). For example, Drummond & Pines (1962) considered the change of the kinetic energy resulting from resonant electrons with $\omega_r = vk$ and nonresonant electrons with $\omega_r \neq vk$ in a quasilinear diffusion process, and they demonstrated that the energy transfer directions are opposite between electron plasma oscillations and resonant/nonresonant electrons (see also Bellan 2008, Chapter 14).

A detailed explanation of the energy transfer distribution of the Alfvén-mode wave in 2D velocity space has been proposed in Section 4. Here we provide a simple physical explanation of the energy transfer direction associated with resonant/nonresonant particles. In addition to the electromagnetic energy $W_{\rm EB}$, the Alfvén-mode wave carries the kinetic energy $W_V = \sum_s \rho_s |\widetilde{\mathbf{V}}_s|^2/2$ that behaves as the oscillatory kinetic energy of nonresonant particles, where ρ_s and $\widetilde{\mathbf{V}}_s$ denote the density and fluid velocity perturbations of species "s." When the Alfvén-mode wave is damping, both $W_{\rm EB}$ and W_V decrease, and energy flows into resonant particles. While a growing Alfvén-mode wave is driven by one resonant instability, energy transfers from resonant particles into $W_{\rm EB}$ and W_V (we note that the resonant energy transfer rate in a weak resonant instability can be estimated by using the δ-function term in velocity

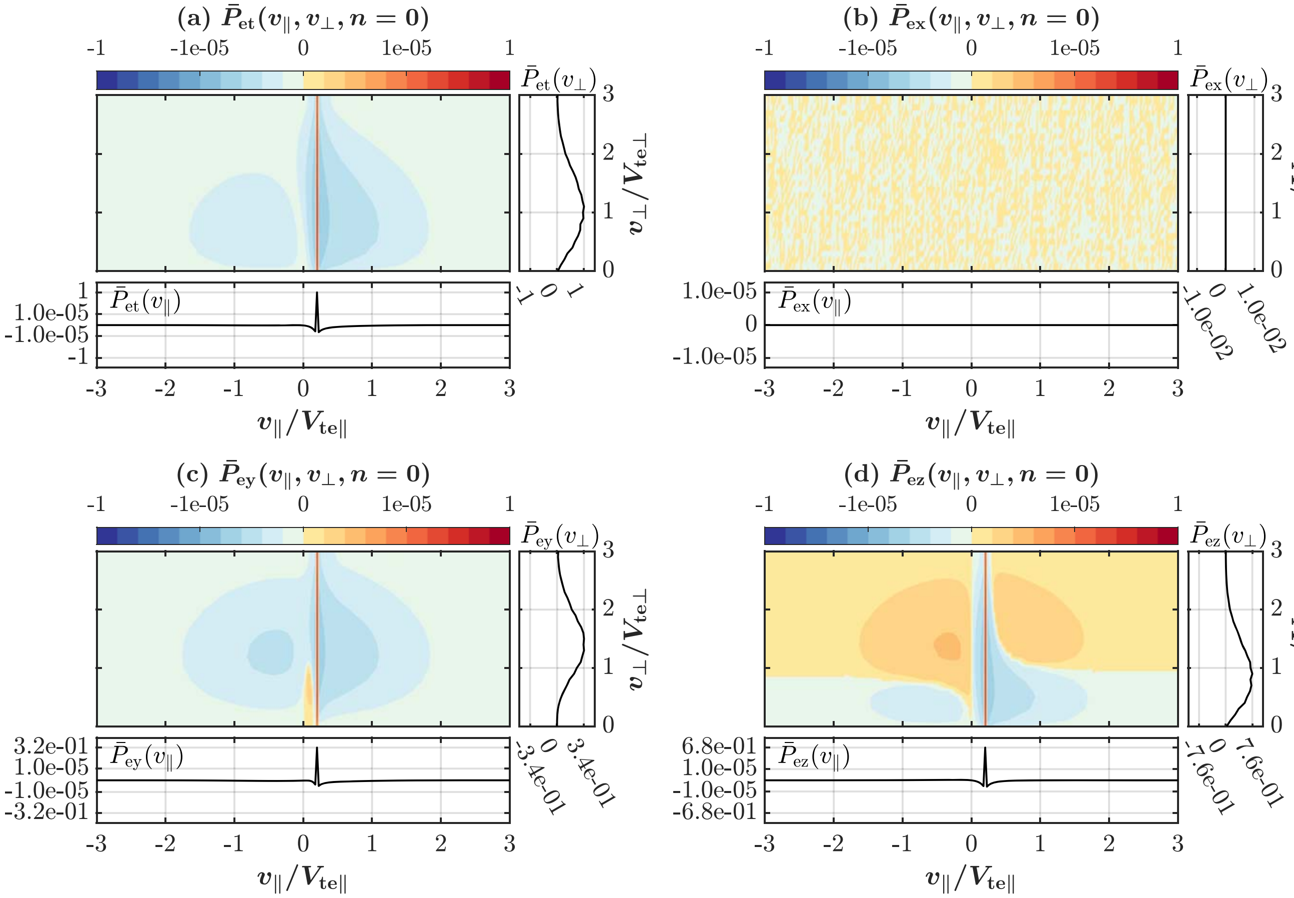

Figure 12. The 1D and 2D distributions of electron energy transfer rates at $n = 0$ in Case 4 where $\lambda_p k_\parallel = 0.01$ and $\lambda_p k_\perp = 10$. The description of panels (a)–(d) is the same as that in Figure 6.

integral (see Equation (31)); however, this procedure would not be used to strictly describe resonant wave–particle interactions in a strong resonant instability where the growth rate is large). Resonant wave–particle interactions will smooth the particle velocity distribution function in the resonance region, leading to an irreversible process (e.g., Drummond & Pines 1962; Sagdeev & Galeev 1969). However, the change in the particle velocity distribution function related to nonresonant particles is an adiabatic process, i.e., the population of nonresonant particles looks like it is "cooling" or "heating" as the wave is damping or growing, and the entropy cannot change during this adiabatic process (e.g., Sagdeev & Galeev 1969; Bellan 2008).

Furthermore, because the energy transfer between electromagnetic fluctuations and the whole plasma determines the change of fluctuating electromagnetic energy, secular energy transfer is proposed to diagnose the dissipation of space plasma turbulence and the excitation of the quasi-monochromatic wave (He et al. 2019; Duan et al. 2020; He et al. 2020; Sun et al. 2021; Liu et al. 2021; Kitamura et al. 2021). He et al. (2019) performed the analysis for the energy transfer between fluctuating electromagnetic energy and plasma kinetic energy in Earth's magnetosheath, and they first give a quantitative estimation of the energy dissipation rate at ion scales. He et al. (2020) further performed the analysis for the dissipation rate spectra defined by $\gamma = -\sum_s P_s/2$ in typical Alfvénic turbulence in the space plasma, and they provided observational evidence of the electromagnetic energy converted to electron parallel kinetic energy. Kitamura et al. (2021) provided observational evidence of the excitation of quasi-monochromatic ion-cyclotron waves in Earth's magnetosheath through the analysis of the energy transfer (see also He et al. 2019). Liu et al. (2021) and Sun et al. (2021) explored the detailed physical mechanism responsible for the instabilities driven by beaming protons and electrons by using the energy transfer method.

5.2. Two Energy Transfer Functions in Velocity Space: $(q_s\boldsymbol{E}_1 \bullet \boldsymbol{v}f_{s1})$ versus $(-q_s v^2\boldsymbol{E}_1 \bullet \partial_v f_{s1}/2)$

This study uses the function $f_1 = q_s\boldsymbol{E}_1 \cdot \boldsymbol{v}f_{s1}$ to quantify wave–particle interactions. One reason for using this function is that only f_1 contributes to the net energy transfer between the particles and waves. Chen et al. (2019) and Cerri et al. (2021) have used f_1 to identify resonant wave–particle interactions based on spacecraft and simulation data.

The field–particle correlation method proposed by Klein & Howes (2016) and Howes et al. (2017) used the function $f_2 = -q_s v^2\boldsymbol{E}_1 \cdot \partial_{\boldsymbol{v}} f_{s1}/2$ to quantify the wave–particle interaction (see Equation (7)). Based on f_2, Klein & Howes (2016) first gave the signature of the electron Landau damping of Langmuir wave in velocity space (also see Howes et al. 2017). Recently, Klein et al. (2020) used the same method to exhibit the signatures of the proton Landau damping and proton cyclotron damping through Alfvénic turbulence simulation. We note that the difference between f_1 and f_2 is $f_3 = q_s\boldsymbol{E}_1 \cdot \partial_{\boldsymbol{v}}(v^2 f_{s1})/2$ (see Equation (8)).

Although the integration of f_1 in velocity space is the same as that of f_2, these two functions have different distributions in velocity space. The comparison of the energy transfer rate distributions related to f_1 and f_2 is presented in Figure 13, which considers the $n = 1$ proton cyclotron interaction in Case 2, the proton transit-time and Landau interactions in Case 3, and the electron transit-time and Landau interactions in Case 4. The energy transfer rate distributions of f_1 are obviously deviating from those of f_2 at small $v_\perp$. These obvious differences between the two distributions of f_1 and f_2 indicate that f_3 can considerably affect the distribution of the energy transfer rate (it does not contribute to the net energy transfer).

We propose that these two correlation methods have their own advantages. For example, the f_1 method does not need to calculate the gradient of the perturbed particle velocity distribution function in velocity space, and the f_2 method can provide more details on the mass, momentum, and energy transfer in velocity space. Combining the two methods would be better to give a comprehensive picture of wave–particle interactions in collisionless plasmas, which will be investigated in the future. We note that in addition to the energy transfer rate related to f_1, Chen et al. (2019) have also used an f_1 and f_2 combined energy transfer rate to diagnose the electron Landau damping in magnetosheath plasma.

5.3. Dependence on β

The plasma beta is a key parameter affecting wave–particle interactions. Here we consider the beta dependence of two typical Alfvén-mode waves, i.e., the parallel-propagating Alfvén wave and the highly oblique Alfvén wave propagating at $\theta = 89°$. The former can encounter $n = 1$ cyclotron wave–particle interactions, and the latter will experience $n = 0$ transit-time and Landau wave–particle interactions.

For the β_p dependence of the wave–particle interaction of the parallel-propagating Alfvén wave, because the ratio of the proton resonant speed at $n = 1$ to the proton thermal speed, $|V_{\mathrm{r1}}|/V_{\mathrm{tp}} = |\omega_r - \Omega_{\mathrm{cp}}|/(k_\parallel V_{\mathrm{tp}}) \sim (\lambda_p k_\parallel)^{-1}\beta_p^{-1/2}$, decreases with increasing β_p at a fixed $\lambda_p k_\parallel$, more protons take part in cyclotron interactions in larger β_p plasmas, which would induce a larger damping rate. Figure 14 presents the distributions of the energy transfer rate induced by the $n = 1$ wave–particle interaction in a $\beta_p = 30$ plasma. This figure shows that the signatures of resonant wave–particle interactions arise at resonant speeds (i.e., $v_\parallel \simeq -2.9V_{\mathrm{tp}}$ at $\lambda_p k = 0.06$, and $v_\parallel \simeq -1.9V_{\mathrm{tp}}$ at $\lambda_p k = 0.09$), and nonresonant wave–particle interactions mainly concentrate around the resonant speeds and/or $v_\parallel \sim 0$. These results are consistent with those in the intermediate-beta plasma shown in Section 4. We note that Appendix D presents more wave properties of the parallel-propagating Alfvén wave as functions of β_p and $\lambda_p k$.

For the $n = 0$ wave–particle interactions between highly oblique Alfvén waves and protons, according to $V_{\mathrm{r0}}/V_{\mathrm{tp}} = \omega_r/(k_\parallel V_{\mathrm{tp}}) = \omega_r/(k_\parallel V_A)\beta_p^{-1/2}$, the MHD Alfvén waves can even encounter strong wave–particle interactions in high-beta plasmas ($\beta_p \gtrsim 1$; also see Appendix D). For the $n = 0$ wave–particle interactions related to electrons, due to $V_{\mathrm{r0}}/V_{\mathrm{te}} = \omega_r/(k_\parallel V_{\mathrm{te}}) = \omega_r/(k_\parallel V_A)(m_e/m_p)^{1/2}\beta_e^{-1/2}$, different from protons, the MHD Alfvén waves can experience considerable wave–particle interactions in plasmas with $\beta_e \lesssim 1$. Figure 15 compares the $v_\parallel$–$v_\perp$ distributions of energy transfer rates of highly oblique Alfvén waves with $\lambda_p k_\perp = 0.5$ in plasmas with different β: $\beta \equiv \beta_p = \beta_e = 0.03$, 0.3, 3, and 30. The most remarkable result in this figure is that with increasing β, nonresonant proton energy transfer rates $P_{\mathrm{py}}(n = 0)$ and $P_{\mathrm{pz}}(n = 0)$ become more sensitive with $v_\perp$. This dependence is induced by the functions $J_0(a_p)$ and $J_0'(a_p)$, which vary highly with $v_\perp$ in the velocity regime of $v_\perp \leqslant 3V_{\mathrm{tp}}$ at higher β. Moreover, Figure 15 shows that nonresonant energy transfer rates $P_{\mathrm{ey}}(n = 0)$ and $P_{\mathrm{ez}}(n = 0)$ become weaker with increasing β. We note that Appendix D summarizes the contributions of both resonant and nonresonant energy transfer rates of proton and electron populations for highly oblique Alfvén waves at different β plasmas.

6. Summary

At first, this study introduces a theoretical method to obtain the particle velocity distribution function perturbations resulting from wave–particle interactions. By using these particle velocity distributions, we can calculate energy transfer rates with different definitions, e.g., Equations (19)–(26), to analyze different types of wave–particle interactions. For example, we can quantify the transit-time wave–particle interaction via $P_{\mathrm{sy}}(n = 0)$, the Landau wave–particle interaction via $P_{\mathrm{sz}}(n = 0)$, the normal cyclotron wave–particle interaction via $P_{\mathrm{px}}(n = 1)$ and $P_{\mathrm{py}}(n = 1)$ for protons ($P_{\mathrm{ex}}(n = -1)$ and $P_{\mathrm{ey}}(n = -1)$ for electrons), and the abnormal cyclotron interaction $P_{\mathrm{px}}(n = -1)$ and $P_{\mathrm{py}}(n = -1)$ for protons ($P_{\mathrm{ex}}(n = 1)$ and $P_{\mathrm{ey}}(n = 1)$ for electrons).

Second, using energy transfer rates with different expressions, we explored different behaviors of wave–particle interactions of the Alfvén-mode wave in a typical inner heliosphere plasma environment where $\beta_p = \beta_e \sim 0.37$.

From the total proton and electron energy transfer rates in wavevector space (see Figure 2), we find that wave damping is mainly caused by the interactions with protons when $\theta \lesssim 62°$, and the wave damping is mainly contributed by the interactions with electrons when $\theta \gtrsim 62°$.

From energy transfer rates at different n (Figure 3) and the distributions of energy transfer rates in velocity space (Figures 4–12), we show that the damping of the Alfvén-mode wave is indeed controlled by different wave–particle interaction mechanisms in different wavevector regimes, and we classify the Alfvén-mode wave in wavevector space into four main types.

(i) The quasi-parallel and medium oblique MHD Alfvén waves with $\lambda_p k_\parallel \lesssim 0.4$ and $\theta \lesssim 72°$ are mainly dissipated through the proton transit-time and Landau damping mechanisms.

(ii) The quasi-parallel ion-cyclotron waves with $\lambda_p k_\parallel \gtrsim 0.5$ and $\theta \lesssim 45°$ are mainly damped by proton cyclotron resonant interactions.

(iii) The quasi-perpendicular MHD and ion-scale Alfvén waves with $\lambda_p k_\perp \lesssim 1$ are mainly dissipated via the proton and electron Landau damping mechanisms.

And (iv) the quasi-perpendicular sub-ion-scale Alfvén waves with $\lambda_p k_\perp \gtrsim 1$ are dissipated by the electron Landau damping mechanism.

Furthermore, through the 1D and 2D distributions of proton and electron energy transfer rates in velocity space (see Section 4), we exhibit the detailed wave–particle interactions of Alfvén-mode waves. In addition to providing the evident signatures of each kind of resonant wave–particle interactions, we give the signatures of wave–particle interactions of

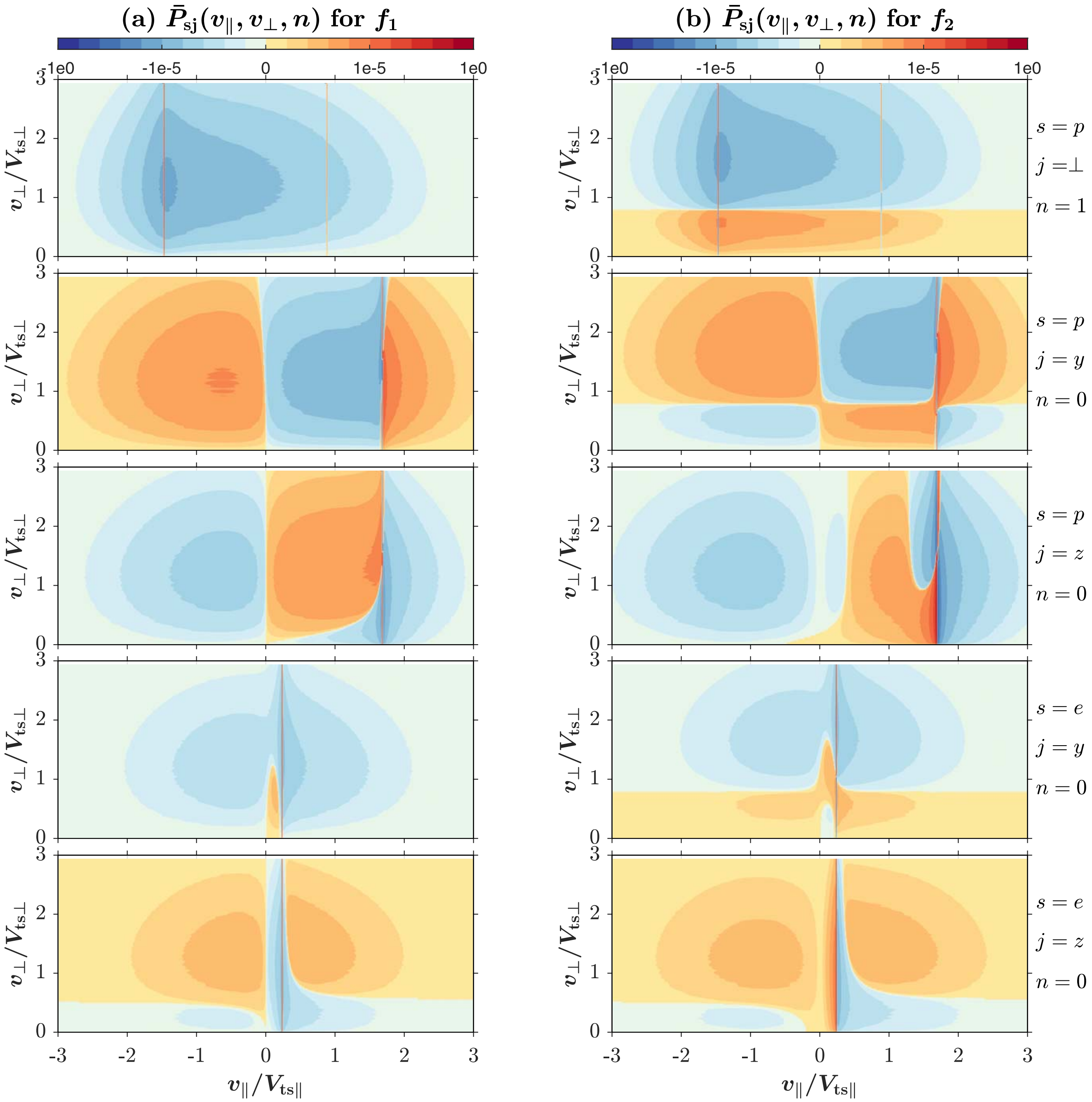

Figure 13. A comparison between two different wave–particle correlation functions: (a) $f_1 = q_s \boldsymbol{E}_1 \cdot \boldsymbol{v} f_{s1}$ and (b) $f_2 = -q_s v^2 \boldsymbol{E}_1 \cdot \partial_{\boldsymbol{v}} f_{s1}/2$. (Upper panels) $\bar{P}_{p\perp}(v_\parallel, v_\perp, n=1)$ in Case 2; (second panels) $\bar{P}_{\rm py}(v_\parallel, v_\perp, n=0)$ in Case 3; (third panels) $\bar{P}_{\rm pz}(v_\parallel, v_\perp, n=0)$ in Case 3; (fourth panels) $\bar{P}_{\rm ey}(v_\parallel, v_\perp, n=0)$ in Case 4; and (bottom panels) $\bar{P}_{\rm ez}(v_\parallel, v_\perp, n=0)$ in Case 4.

nonresonant particles in velocity space. Our main findings of nonresonant wave–particle interactions are

(i) Nonresonant wave–particle interactions can lead to significant energy released from nonresonant particles (see Table 1).
(ii) Nonresonant wave–proton interactions at $n=1$ become strong at $v_\parallel \sim 0$ and/or $v_\parallel \sim V_{\rm r1}$.
(iii) The energy transfer direction induced by nonresonant transit-time interactions is roughly opposite to that induced by nonresonant Landau interactions in velocity space.

This study also compares two energy transfer functions, i.e., $(q_s \boldsymbol{E}_1 \cdot \boldsymbol{v} f_{s1})$ versus $(-q_s v^2 \boldsymbol{E}_1 \cdot \partial_{\boldsymbol{v}} f_{s1}/2)$ (see Section 5.2). Although these two functions result in the same net energy transfer rates between the waves and particles, their distributions are obviously different at small $v_\perp$ in velocity space (see Figure 14).

Finally, this paper explores the dependence of the distribution of energy transfer rates on the plasma beta (see Section 5.3). We show that due to the change in Bessel functions $J_0(a_p)$ and $J_0'(a_p)$, the highly varying energy transfer rate arises at large β_p for an highly oblique Alfvén wave. Moreover, according to the analysis of energy transfer rates, we

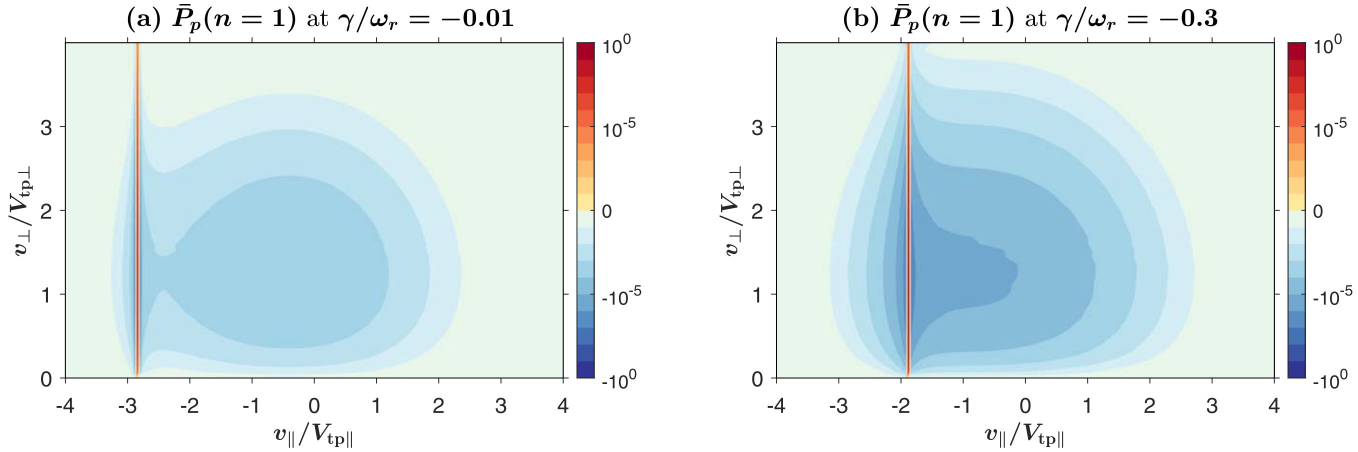

Figure 14. The $v_\parallel$–$v_\perp$ distributions of proton energy transfer rates at $n = 1$ for parallel-propagating Alfvén-mode waves in a $\beta_p = 30$ plasma: (a) the wave having $\lambda_p k = 0.06$, $\omega_r/\Omega_{\mathrm{cp}} \simeq 0.03$, and $\gamma/\omega_r = -0.01$; and (b) the wave having $\lambda_p k = 0.09$, $\omega_r/\Omega_{\mathrm{cp}} \simeq 0.03$, and $\gamma/\omega_r = -0.3$. The data are normalized by the maximum in each distribution.

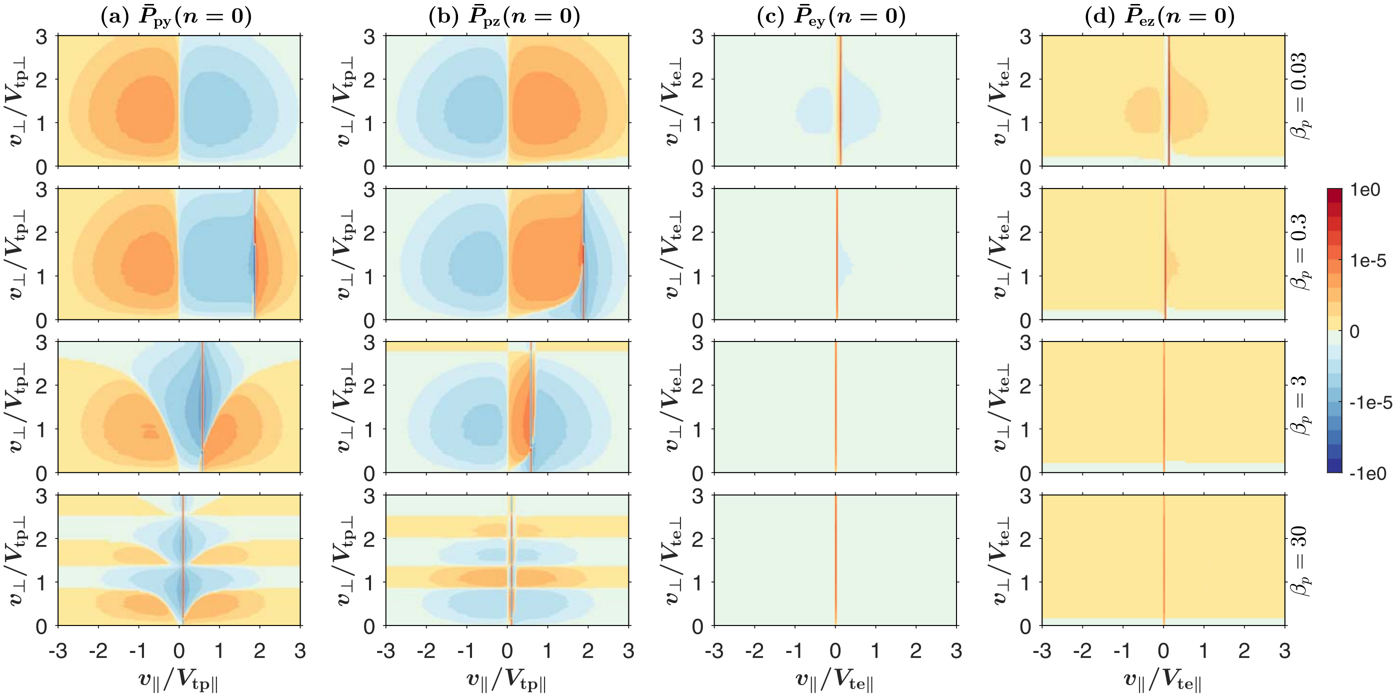

Figure 15. The $v_\parallel$–$v_\perp$ distributions of energy transfer rates at $n = 0$ associated with highly oblique ($\theta = 89°$) Alfvén-mode waves: (a) the proton energy transfer rate in the y direction; (b) the proton energy transfer rate in the z direction; (c) the electron energy transfer rate in the y direction; and (d) the electron energy transfer rate in the z direction. From the upper to bottom panels, β_p is increasing: (upper panels) $\beta_p = 0.03$, (second panels) $\beta_p = 0.3$, (third panels) $\beta_p = 3$, and (bottom panels) $\beta_p = 30$. The data are normalized by the maximum in each total energy transfer rate distribution.

classify the $\lambda_p k$–β_p space of the highly oblique Alfvén wave into the following four regions.

(i) The proton transit-time damping regime ($P^r_{\mathrm{py}}(n = 0)/(2|\gamma|) \gtrsim 1$), where $\lambda_p k \lesssim 1$ and $\beta_p \gtrsim 0.5$.

(ii) The proton Landau damping regime ($P^r_{\mathrm{pz}}(n = 0) \gtrsim 1$), where $\lambda_p k \lesssim 1$ and $\beta_p \sim 0.2$–0.5.

(iii) The electron transit-time damping regime ($P^r_{\mathrm{ey}}(n = 0) \gtrsim 1$), where $\lambda_p k \gtrsim 1$ and $\beta_e = \beta_p \gtrsim 0.3$.

And (iv) the electron Landau damping regime ($P^r_{\mathrm{pz}}(n = 0) \gtrsim 1$), where $\beta_e = \beta_p \lesssim 0.2$.

According to these interesting findings, we propose that the method developed in this paper is very useful for understanding linear wave–particle interactions in the plasmas.

This work was supported by the NNSFC 41974203. J.Z. appreciates the referee for inspiring comments and helpful suggestions.

Appendix A
Electromagnetic Perturbations and Dispersion Relations near the Frequency Transition Points of the Alfvén-mode Wave

In this appendix, we will explore more mode properties of the Alfvén-mode wave. For simplicity, we ignore the subscript "1" in the expressions of the first-order perturbations in this appendix and in the following appendices.

Figure 16 presents electromagnetic perturbations of the Alfvén-mode wave. We see that the Alfvén-mode wave is circularly polarized ($\widetilde{E}_x/\widetilde{E}_y \simeq e^{i\pi/2}$ and $\widetilde{B}_x/\widetilde{B}_y \simeq e^{i\pi/2}$) as $k_\parallel \gg k_\perp$, and this mode becomes highly elliptical or even linearly polarized ($|\widetilde{E}_x| \gg |\widetilde{E}_y|$ and $|\widetilde{B}_y| \gg |\widetilde{B}_x|$) at finite $\lambda_p k_\perp$ and/or at a finite wave normal angle θ. The left-hand circularly polarized wave can induce a normal cyclotron resonant interaction, and the highly elliptically (or linearly) polarized wave can result in both normal and anomalous cyclotron resonant interactions due to $\widetilde{E}_L = \widetilde{E}_x + i\widetilde{E}_y \neq 0$ and $\widetilde{E}_R = \widetilde{E}_x - i\widetilde{E}_y \neq 0$. Moreover, because Alfvén-mode waves are not strictly parallel propagation in Figure 16, there exist the parallel electric and magnetic field perturbations, and these parallel fields can lead to both Landau and transit-time resonant interactions. Furthermore, from the phase differences between two perpendicular electromagnetic perturbations as shown in

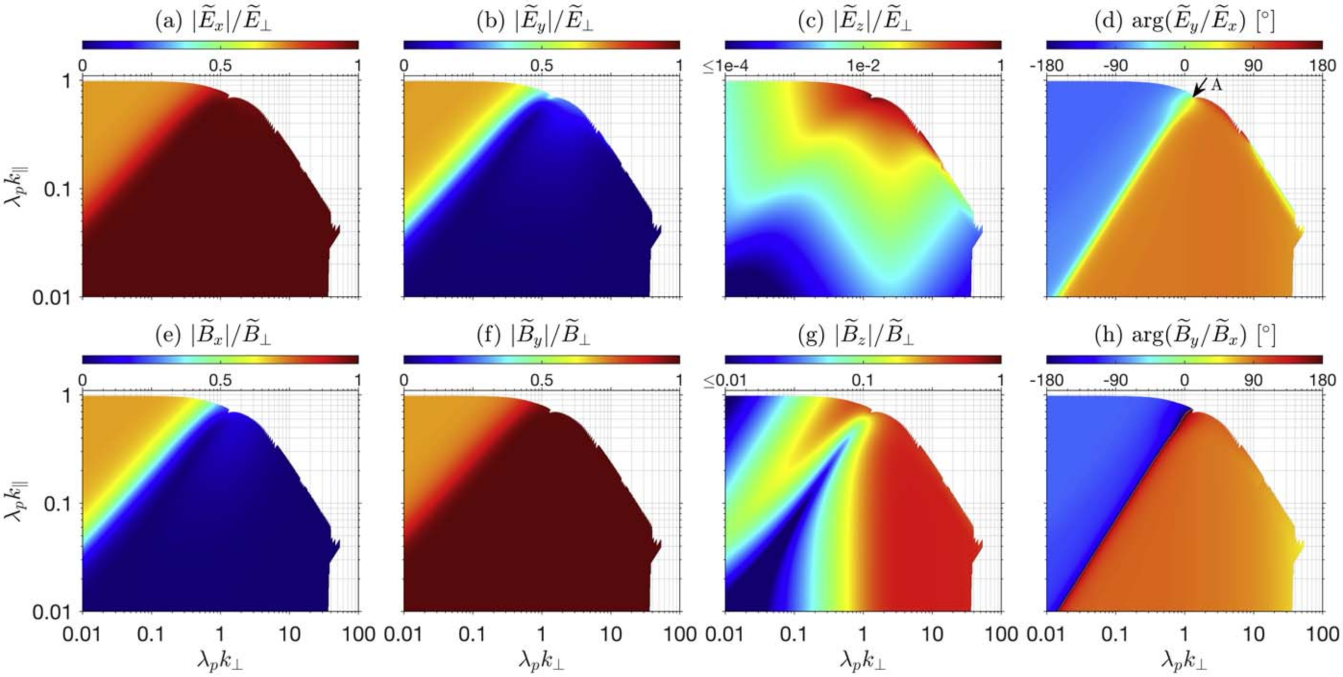

Figure 16. The distributions of electromagnetic perturbations of the Alfvén-mode wave in $k_\perp$–$k_\parallel$ space: (a) $|\widetilde{E}_x|/\widetilde{E}_\perp$; (b) $|\widetilde{E}_y|/\widetilde{E}_\perp$; (c) $|\widetilde{E}_z|/\widetilde{E}_\perp$; (d) the phase difference between $\widetilde{E}_x$ and $\widetilde{E}_y$; (e) $|\widetilde{B}_x|/\widetilde{B}_\perp$; (f) $|\widetilde{B}_y|/\widetilde{B}_\perp$; (g) $|\widetilde{B}_z|/\widetilde{B}_\perp$; and (h) the phase difference between $\widetilde{B}_x$ and $\widetilde{B}_y$. $\widetilde{E}_\perp = (|\widetilde{E}_x|^2 + |\widetilde{E}_y|^2)^{1/2}$ and $\widetilde{B}_\perp = (|\widetilde{B}_x|^2 + |\widetilde{B}_y|^2)^{1/2}$ denote the perpendicular electric and magnetic perturbations, respectively. The arrow "A" labels the transition point associated with the dispersion relation.

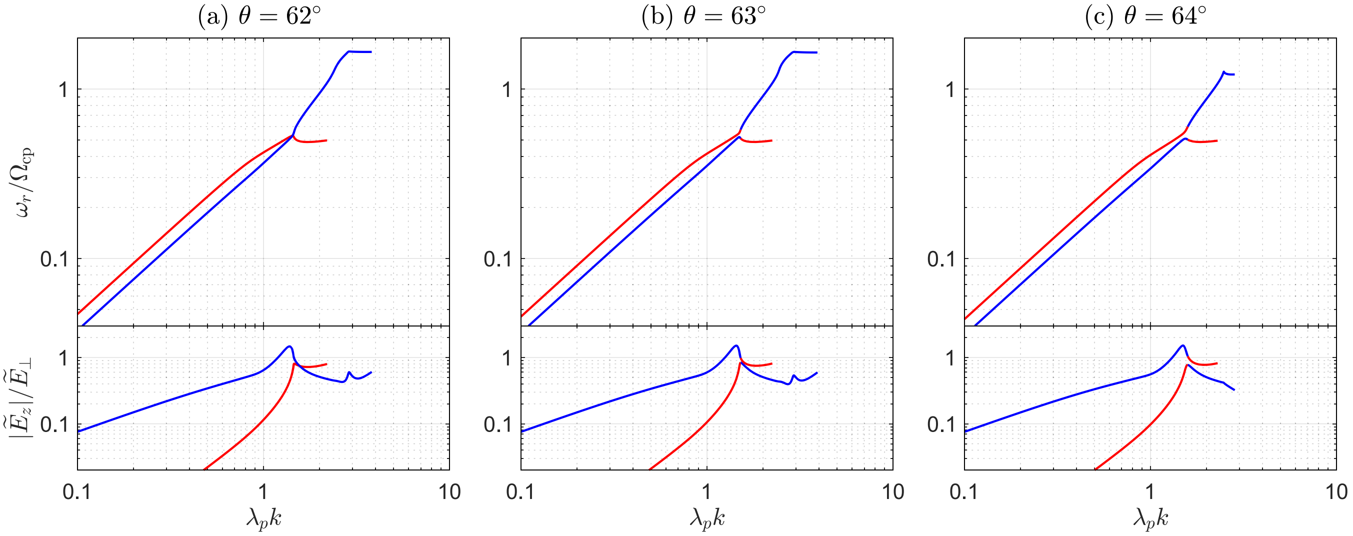

Figure 17. The dispersion relations and $|\widetilde{E}_z/\widetilde{E}_\perp|$ of the Alfvén-mode wave at three angles: (a) $\theta = 62°$, (b) 63°, and (c) 64°. The red and blue curves denote the Alfvén-mode wave and the slow-mode wave, respectively.

Figures 16(d) and 16(h), we can see the polarization of the Alfvén-mode wave changes at $\theta \sim 62°$, i.e., from left-hand to right-hand polarization (e.g., Gary 1986; Zhao et al. 2014). The change in polarization leads to the change in the definition of normal and anomalous cyclotron resonant interactions based on the resonant condition $k_\parallel v_\parallel = \omega - n\Omega_{\rm cp}$, i.e., normal cyclotron interaction corresponding to $n > 0$ ($n < 0$) for the left-hand (right-hand) polarization wave, and anomalous cyclotron interaction corresponding to $n < 0$ ($n > 0$) for the left-hand (right-hand) polarization wave.

In addition to the polarization transition, there is a transition point labeled “A” in Figure 16(d) corresponding to the coupling between the Alfvén-mode wave and the slow-mode wave. In order to show how dispersion relations vary at the transition point A, Figure 17 shows the dispersion relations and $\widetilde{E}_z/\widetilde{E}_\perp$ of the Alfvén-mode wave and slow-mode wave at $\theta = 62°$, 63°, and 64°. The Alfvén-mode wave is cut off at the frequency $\omega \simeq 0.5\Omega_{\rm cp}$ near the resonance frequency $\Omega_{\rm cp}\cos(\theta)$ at $\theta = 62°$, and the slow-mode wave is extended to frequency larger than $\Omega_{\rm cp}$. At $\theta = 63°$, the two mode waves are coupled, in which the low-frequency ($\omega \lesssim 0.5\Omega_{\rm cp}$) Alfvén-mode wave and high-frequency ($\omega \gtrsim 0.5\Omega_{\rm cp}$) slow-mode wave merge together, and the low-frequency slow-mode wave connects to the Alfvén mode at $\omega \simeq 0.5\Omega_{\rm cp}$. At $\theta = 64°$, the two recombined mode waves separate more clearly. Because this paper mainly focuses on the wave–particle interaction of the Alfvén-mode wave, in order to obtain the Alfvén-mode branch from the combined mode wave, we use the parallel electric field perturbation as an indicator. The merging point between the low-frequency Alfvén-mode wave and the high-frequency slow-mode wave corresponds to the position of the peak in the $\widetilde{E}_z/\widetilde{E}_\perp$ distribution (the corresponding wavenumber is defined by $k_{E_{\rm zpeak}}$). Therefore, the Alfvén-mode wave is the mode branch with $k < k_{E_{\rm zpeak}}$ in the wave normal angle region of $\theta \gtrsim 63°$. This criterion is used to obtain the dispersion surface of the Alfvén-mode wave in this study. However, it should be noted that as θ is much larger than 64°, we cannot strictly discriminate the Alfvén wave part from the slow wave part in the high-frequency branch due to the slow-wave part also behaving Alfvén like.

Appendix B
The Conductivity Tensor and the Current Density

Based on the Vlasov–Maxwellian model, the conductivity tensor is given by

$$\boldsymbol{\sigma}_s = -i\epsilon_0\frac{\omega_{\rm ps}^2}{\omega}\sum_n[\zeta_0 Z(\zeta_n)\boldsymbol{X}_n + 2\eta_0^2\Gamma_n\boldsymbol{L}_{\rm zz}], \tag{B1}$$

where

$$\boldsymbol{X}_n = \begin{pmatrix} n^2\Gamma_n/b & in\Gamma_n' & \sqrt{2/b}\, n\eta_n\Gamma_n \\ -in\Gamma_n' & n^2\Gamma_n/b - 2b\Gamma_n' & -i\sqrt{2b}\,\eta_n\Gamma_n' \\ \sqrt{2/b}\, n\eta_n\Gamma_n & i\sqrt{2b}\,\eta_n\Gamma_n' & 2\eta_n^2\Gamma_n \end{pmatrix}. \tag{B2}$$

Using the conductivity tensor at each n, $\boldsymbol{\sigma}_{\rm sn} = -i\epsilon_0(\omega_{\rm ps}^2/\omega)[\zeta_0 Z(\zeta_n)\boldsymbol{X}_n + 2\eta_0^2\Gamma_n\boldsymbol{L}_{\rm zz}]$, the current density at each n is given by

$$\widetilde{\boldsymbol{J}}_s(n) = \boldsymbol{\sigma}_{\rm sn}\cdot\widetilde{\boldsymbol{E}}. \tag{B3}$$

Appendix C
Resonant and Nonresonant Energy Transfer Rates at $n = 0$ and $n = \pm 1$

Here we consider the damping wave and give the analytical expressions of energy transfer rates resulting from resonant and nonresonant particles in Maxwellian plasmas. In $v_\parallel$–$v_\perp$ space, energy transfer rates are described by the following general expression,

$$P_{\rm sj}(v_\parallel, v_\perp, n) = \frac{1}{4W_{\rm EB}}[\widetilde{\boldsymbol{E}}_j\cdot\widetilde{\boldsymbol{J}}_{\rm sj}^*(v_\parallel, v_\perp, n) + \widetilde{\boldsymbol{E}}_j^*\cdot\widetilde{\boldsymbol{J}}_{\rm sj}(v_\parallel, v_\perp, n)], \tag{C1}$$

where j denotes the axis direction x, y, or z, and $J_{\rm sj}(n)$ denotes the j-direction current density at different n. Here we summarize the resonant and nonresonant energy transfer rates at $n = 0$ and $n = \pm 1$.

C.1. Energy Transfer Rates at $n = 0$

C.1.1. Resonant Energy Transfer Rates

Considering the $n = 0$ resonant wave–particle interactions and using Equation (27), resonant current densities are given as

$$\widetilde{J}_{\rm sy}^r(v_\parallel, v_\perp, n = 0) = C_{n=0}^r\int_0^{2\pi} d\phi[\sin(\phi)e^{ia_s\sin(\phi)}],$$

and

$$\widetilde{J}_{\rm sz}^r(v_\parallel, v_\perp, n = 0) = C_{n=0}^r\frac{v_\parallel}{v_\perp}\int_0^{2\pi} d\phi[e^{ia_s\sin(\phi)}],$$

with

$$C_{n=0}^r \equiv \frac{4\pi q_s^2}{m_s k_\parallel}\frac{v_\perp^3 f_{\rm s0}}{V_{\rm ts}^2}\left[iJ_0'(a_s)\widetilde{E}_y + \frac{v_\parallel}{v_\perp}J_0(a_s)\widetilde{E}_z\right]\delta(v_\parallel - V_{\rm r0}).$$

Then from Equation (C1) and the following relations

$$\int_0^{2\pi} d\phi[\sin(\phi)e^{ia_s\sin(\phi)}] = -i2\pi J_0'(a_s),$$
$$\int_0^{2\pi} d\phi[e^{ia_s\sin(\phi)}] = 2\pi J_0(a_s), \tag{C2}$$

resonant energy transfer rates at $n = 0$ are given as

$$P_{\rm sy}^r(v_\parallel, v_\perp, n = 0) = \frac{4\pi^2 q_s^2}{W_{\rm EB}m_s k_\parallel}\frac{v_\perp^3 f_{\rm s0}J_0'(a_s)}{V_{\rm ts}^2}$$
$$\times\left[J_0'(a_s)|\widetilde{E}_y|^2 - \frac{v_\parallel}{v_\perp}J_0(a_s)\sin(\psi_{\widetilde{E}_y} - \psi_{\widetilde{E}_z})|\widetilde{E}_y||\widetilde{E}_z|\right]$$
$$\times\,\delta(v_\parallel - V_{\rm r0}), \tag{C3}$$

and

$$P_{\rm sz}^r(v_\parallel, v_\perp, n = 0) = \frac{4\pi^2 q_s^2}{W_{\rm EB}m_s k_\parallel}\frac{v_\parallel v_\perp^2 f_{\rm s0}J_0(a_s)}{V_{\rm ts}^2}$$
$$\times\left[J_0'(a_s)\sin(\psi_{\widetilde{E}_z} - \psi_{\widetilde{E}_y})|\widetilde{E}_z||\widetilde{E}_y| + \frac{v_\parallel}{v_\perp}J_0(a_s)|\widetilde{E}_z|^2\right]$$
$$\times\,\delta(v_\parallel - V_{\rm r0}). \tag{C4}$$

C.1.2. Nonresonant Energy Transfer Rates

Current densities induced by wave–particle interactions of the $n = 0$ nonresonant particles are given as

$$\widetilde{J}_{\mathrm{sy}}^{\mathrm{nr}}(v_{\|}, v_{\perp}, n = 0) = C_{n=0}^{\mathrm{nr}} \int_0^{2\pi} d\phi[\sin(\phi)e^{ia_s\sin(\phi)}]$$

and

$$\widetilde{J}_{\mathrm{sz}}^{\mathrm{nr}}(v_{\|}, v_{\perp}, n = 0) = C_{n=0}^{\mathrm{nr}} \frac{v_{\|}}{v_{\perp}} \int_0^{2\pi} d\phi[e^{ia_s\sin(\phi)}],$$

with

$$C_{n=0}^{\mathrm{nr}} = -i\frac{2q_s^2}{m_s k_{\|}} \frac{v_{\perp}^3 f_{s0}}{V_{\mathrm{ts}}^2 (v_{\|} - \omega/k_{\|})} \left[iJ_0'(a_s)\widetilde{E}_y + \frac{v_{\|}}{v_{\perp}} J_0(a_s)\widetilde{E}_z \right].$$

Using Equation (C2) and the following expression

$$\frac{1}{v_{\|} - \omega/k_{\|}} = \frac{v_{\|} - V_{\mathrm{r0}} + i\gamma/k_{\|}}{(v_{\|} - V_{\mathrm{r0}})^2 + (\gamma/k_{\|})^2},$$

nonresonant energy transfer rates at $n = 0$ are given by

$$\begin{aligned} P_{\mathrm{sy}}^{\mathrm{nr}}(v_{\|}, v_{\perp}, n = 0) = {} & \frac{2\pi q_s^2}{W_{\mathrm{EB}} m_s k_{\|}} \frac{(v_{\perp}^3/V_{\mathrm{ts}}^2) f_{s0} J_0'(a_s)}{(v_{\|} - V_{\mathrm{r0}})^2 + (\gamma/k_{\|})^2} \\ & \times \left\{ \frac{\gamma}{k_{\|}} J_0'(a_s)|\widetilde{E}_y|^2 \right. \\ & - \frac{v_{\|}}{v_{\perp}} J_0(a_s) \left[(v_{\|} - V_{\mathrm{r0}}) \cos(\psi_{\widetilde{E}_y} - \psi_{\widetilde{E}_z}) \right. \\ & \left. \left. + \frac{\gamma}{k_{\|}} \sin(\psi_{\widetilde{E}_y} - \psi_{\widetilde{E}_z}) \right] |\widetilde{E}_y||\widetilde{E}_z| \right\} \end{aligned} \tag{C5}$$

and

$$\begin{aligned} P_{\mathrm{sz}}^{\mathrm{nr}}(v_{\|}, v_{\perp}, n = 0) = {} & \frac{2\pi q_s^2}{W_{\mathrm{EB}} m_s k_{\|}} \frac{(v_{\|} v_{\perp}^2/V_{\mathrm{ts}}^2) f_{s0} J_0(a_s)}{(v_{\|} - V_{\mathrm{r0}})^2 + (\gamma/k_{\|})^2} \\ & \times \left\{ \left[(v_{\|} - V_{\mathrm{r0}}) \cos(\psi_{\widetilde{E}_z} - \psi_{\widetilde{E}_y}) \right. \right. \\ & \left. + \frac{\gamma}{k_{\|}} \sin(\psi_{\widetilde{E}_z} - \psi_{\widetilde{E}_y}) \right] J_0'(a_s)|\widetilde{E}_z||\widetilde{E}_y| \\ & \left. + \frac{\gamma}{k_{\|}} \frac{v_{\|}}{v_{\perp}} J_0(a_s)|\widetilde{E}_z|^2 \right\}. \end{aligned} \tag{C6}$$

C.2. Resonant and Nonresonant Energy Transfer Rates at n = 1

C.2.1. Resonant Energy Transfer Rates

Through the $n = 1$ resonant wave–particle interactions, current densities are given by

$$\begin{aligned} J_{\mathrm{sx}}^{r}(v_{\|}, v_{\perp}, n = 1) &= C_{n=1}^{r} \int_0^{2\pi} d\phi[\cos(\phi)e^{ia_s\sin(\phi)}e^{-i\phi}], \\ J_{\mathrm{sy}}^{r}(v_{\|}, v_{\perp}, n = 1) &= C_{n=1}^{r} \int_0^{2\pi} d\phi[\sin(\phi)e^{ia_s\sin(\phi)}e^{-i\phi}], \\ J_{\mathrm{sz}}^{r}(v_{\|}, v_{\perp}, n = 1) &= C_{n=1}^{r} \frac{v_{\|}}{v_{\perp}} \int_0^{2\pi} d\phi[e^{ia_s\sin(\phi)}e^{-i\phi}], \end{aligned}$$

where

$$\begin{aligned} C_{n=1}^{r} = {} & \frac{4\pi q_s^2}{m_s k_{\|}} \frac{v_{\perp}^3 f_{s0}}{V_{\mathrm{ts}}^2} \left[\frac{J_1(a_s)}{a_s} \widetilde{E}_{x1} + iJ_1'(a_s)\widetilde{E}_y + \frac{v_{\|}}{v_{\perp}} J_1(a_s)\widetilde{E}_z \right] \\ & \times \delta(v_{\|} - V_{\mathrm{r1}}). \end{aligned}$$

Using Equation (C1) and the following relations:

$$\begin{aligned} \int_0^{2\pi} d\phi[\cos(\phi)e^{ia_s\sin(\phi)}e^{-i\phi}] &= \frac{2\pi}{a_s} J_1(a_s), \\ \int_0^{2\pi} d\phi[\sin(\phi)e^{ia_s\sin(\phi)}e^{-i\phi}] &= -i2\pi J_1'(a_s), \\ \int_0^{2\pi} d\phi[e^{ia_s\sin(\phi)}e^{-i\phi}] &= 2\pi J_1(a_s), \end{aligned} \tag{C7}$$

energy transfer rates at $n = 1$ are given by

$$\begin{aligned} P_{\mathrm{sx}}^{r}(v_{\|}, v_{\perp}, n = 1) = {} & \frac{4\pi^2 q_s^2}{W_{\mathrm{EB}} m_s k_{\|}} \frac{v_{\perp}^3 f_{s0}}{V_{\mathrm{ts}}^2} \frac{J_1(a_s)}{a_s} \\ & \times \left\{ \frac{J_1(a_s)}{a_s} |\widetilde{E}_x|^2 + J_1'(a_s) \sin(\psi_{\widetilde{E}_x} - \psi_{\widetilde{E}_y}) |\widetilde{E}_x||\widetilde{E}_y| \right. \\ & \left. + \frac{v_{\|}}{v_{\perp}} J_1(a_s) \cos(\psi_{\widetilde{E}_x} - \psi_{\widetilde{E}_z}) |\widetilde{E}_x||\widetilde{E}_z| \right\} \delta(v_{\|} - V_{\mathrm{r1}}), \end{aligned} \tag{C8}$$

$$\begin{aligned} P_{\mathrm{sy}}^{r}(v_{\|}, v_{\perp}, n = 1) = {} & \frac{4\pi^2 q_s^2}{W_{\mathrm{EB}} m_s k_{\|}} \frac{v_{\perp}^3 f_{s0} J_1'(a_s)}{V_{\mathrm{ts}}^2} \\ & \times \left\{ -\frac{J_1(a_s)}{a_s} \sin(\psi_{\widetilde{E}_y} - \psi_{\widetilde{E}_x}) |\widetilde{E}_y||\widetilde{E}_x| + J_1'(a_s)|\widetilde{E}_y|^2 \right. \\ & \left. - \frac{v_{\|}}{v_{\perp}} J_1(a_s) \sin(\psi_{\widetilde{E}_y} - \psi_{\widetilde{E}_z}) |\widetilde{E}_y||\widetilde{E}_z| \right\} \delta(v_{\|} - V_{\mathrm{r1}}), \end{aligned} \tag{C9}$$

$$\begin{aligned} P_{\mathrm{sz}}^{r}(v_{\|}, v_{\perp}, n = 1) = {} & \frac{4\pi^2 q_s^2}{W_{\mathrm{EB}} m_s k_{\|}} \frac{v_{\|} v_{\perp}^2 f_{s0} J_1(a_s)}{V_{\mathrm{ts}}^2} \\ & \times \left[\frac{J_1(a_s)}{a_s} \cos(\psi_{\widetilde{E}_z} - \psi_{\widetilde{E}_x}) |\widetilde{E}_z||\widetilde{E}_x| \right. \\ & \left. + J_1'(a_s) \sin(\psi_{\widetilde{E}_z} - \psi_{\widetilde{E}_y}) |\widetilde{E}_z||\widetilde{E}_y| + \frac{v_{\|}}{v_{\perp}} J_1(a_s)|\widetilde{E}_z|^2 \right] \delta(v_{\|} - V_{\mathrm{r1}}). \end{aligned} \tag{C10}$$

C.2.2. Nonresonant Energy Transfer Rates

Current densities induced by wave–particle interactions of the $n = 1$ nonresonant particles are given as

$$\begin{aligned} J_{\mathrm{sx}}^{\mathrm{nr}}(v_{\|}, v_{\perp}, n = 1) &= C_{n=1}^{\mathrm{nr}} \int_0^{2\pi} d\phi[\cos(\phi)e^{ia_s\sin(\phi)}e^{-i\phi}], \\ J_{\mathrm{sy}}^{\mathrm{nr}}(v_{\|}, v_{\perp}, n = 1) &= C_{n=1}^{\mathrm{nr}} \int_0^{2\pi} d\phi[\sin(\phi)e^{ia_s\sin(\phi)}e^{-i\phi}], \\ J_{\mathrm{sz}}^{\mathrm{nr}}(v_{\|}, v_{\perp}, n = 1) &= C_{n=1}^{\mathrm{nr}} \frac{v_{\|}}{v_{\perp}} \int_0^{2\pi} d\phi[e^{ia_s\sin(\phi)}e^{-i\phi}], \end{aligned}$$

where

$$C^{\rm nr}_{n=1} = -i\frac{2q_s^2}{m_s k_\parallel}\frac{(v_\perp^3/V_{\rm ts}^2)f_{s0}}{v_\parallel - (\omega - \Omega_{\rm cp})/k_\parallel} \times \left[\frac{J_1(a_s)}{a_s}\widetilde{E}_x + iJ_1'(a_s)\widetilde{E}_y + \frac{v_\parallel}{v_\perp}J_1(a_s)\widetilde{E}_z\right].$$

Using Equation (C7) and the following relation

$$\frac{1}{v_\parallel - (\omega_r - \Omega_{\rm cp})/k_\parallel} = \frac{v_\parallel - V_{\rm r1} + i\gamma/k_\parallel}{(v_\parallel - V_{\rm r1})^2 + (\gamma/k_\parallel)^2},$$

nonresonant energy transfer rates at $n = 1$ are given as

$$\begin{aligned} P^{\rm nr}_{\rm sx}(v_\parallel, v_\perp, n=1) &= \frac{2\pi q_s^2}{W_{\rm EB} m_s k_\parallel}\frac{(v_\perp^3/V_{\rm ts}^2)f_{s0}}{(v_\parallel - V_{\rm r1})^2 + (\gamma/k_\parallel)^2}\frac{J_1(a_s)}{a_s} \\ &\times \left\{\frac{\gamma}{k_\parallel}\frac{J_1(a_s)}{a_s}|\widetilde{E}_x|^2\right. \\ &+ \left[(v_\parallel - V_{\rm r1})\cos(\psi_{\widetilde{E}_x} - \psi_{\widetilde{E}_y}) + \frac{\gamma}{k_\parallel}\sin(\psi_{\widetilde{E}_x} - \psi_{\widetilde{E}_y})\right] \\ &\times J_1'(a_s)|\widetilde{E}_x||\widetilde{E}_y| \\ &- \left[(v_\parallel - V_{\rm r1})\sin(\psi_{\widetilde{E}_x} - \psi_{\widetilde{E}_z}) - \frac{\gamma}{k_\parallel}\cos(\psi_{\widetilde{E}_x} - \psi_{\widetilde{E}_z})\right] \\ &\left.\times \frac{v_\parallel}{v_\perp}J_1(a_s)|\widetilde{E}_x||\widetilde{E}_z|\right\}, \end{aligned} \tag{C11}$$

$$\begin{aligned} P^{\rm nr}_{\rm sy}(v_\parallel, v_\perp, n=1) &= -\frac{2\pi q_s^2}{W_{\rm EB} m_s k_\parallel}\frac{(v_\perp^3/V_{\rm ts}^2)f_{s0}J_1'(a_s)}{(v_\parallel - V_{\rm r1})^2 + (\gamma/k_\parallel)^2} \\ &\times \left\{\left[(v_\parallel - V_{\rm r1})\cos(\psi_{\widetilde{E}_y} - \psi_{\widetilde{E}_x}) + \frac{\gamma}{k_\parallel}\sin(\psi_{\widetilde{E}_y} - \psi_{\widetilde{E}_x})\right]\right. \\ &\times \frac{J_1(a_s)}{a_s}|\widetilde{E}_y||\widetilde{E}_x| - \frac{\gamma}{k_\parallel}J_1'(a_s)|\widetilde{E}_y|^2 \\ &+ \left[(v_\parallel - V_{\rm r1})\cos(\psi_{\widetilde{E}_y} - \psi_{\widetilde{E}_z}) + \frac{\gamma}{k_\parallel}\sin(\psi_{\widetilde{E}_y} - \psi_{\widetilde{E}_z})\right] \\ &\left.\times \frac{v_\parallel}{v_\perp}J_1(a_s)|\widetilde{E}_y||\widetilde{E}_z|\right\}, \end{aligned} \tag{C12}$$

$$\begin{aligned} P^{\rm nr}_{\rm sz}(v_\parallel, v_\perp, n=1) &= -\frac{2\pi q_s^2}{W_{\rm EB} m_s k_\parallel}\frac{(v_\parallel v_\perp^2/V_{\rm ts}^2)f_{s0}J_1(a_s)}{(v_\parallel - V_{\rm r1})^2 + (\gamma/k_\parallel)^2} \\ &\times \left\{\left[(v_\parallel - V_{\rm r1})\sin(\psi_{\widetilde{E}_z} - \psi_{\widetilde{E}_x}) - \frac{\gamma}{k_\parallel}\cos(\psi_{\widetilde{E}_z} - \psi_{\widetilde{E}_x})\right]\right. \\ &\times \frac{J_1(a_s)}{a_s}|\widetilde{E}_z||\widetilde{E}_x| \\ &- \left[(v_\parallel - V_{\rm r1})\cos(\psi_{\widetilde{E}_z} - \psi_{\widetilde{E}_y}) + \frac{\gamma}{k_\parallel}\sin(\psi_{\widetilde{E}_z} - \psi_{\widetilde{E}_y})\right] \\ &\left.\times J_1'(a_s)|\widetilde{E}_z||\widetilde{E}_y| - \frac{\gamma}{k_\parallel}\frac{v_\parallel}{v_\perp}J_1(a_s)|\widetilde{E}_z|^2\right\}. \end{aligned} \tag{C13}$$

C.3. Resonant and Nonresonant Energy Transfer Rates at $n = -1$

The derivation is similar to that given in Section C.2, and here we only summarize the expressions of resonant and nonresonant energy transfer rates at $n = -1$.

C.3.1. Resonant Energy Transfer Rates

Resonant energy transfer rates at $n = -1$ are given as

$$\begin{aligned} P^{r}_{\rm sx}(v_\parallel, v_\perp, n=-1) &= \frac{4\pi^2 q_s^2}{W_{\rm EB} m_s k_\parallel}\frac{v_\perp^3 f_{s0}}{V_{\rm ts}^2}\frac{J_{-1}(a_s)}{a_s} \\ &\times \left\{\frac{J_{-1}(a_s)}{a_s}|\widetilde{E}_x|^2 - J_{-1}'(a_s)\sin(\psi_{\widetilde{E}_x} - \psi_{\widetilde{E}_y})|\widetilde{E}_x||\widetilde{E}_y|\right. \\ &\left.- \frac{v_\parallel}{v_\perp}J_{-1}(a_s)\cos(\psi_{\widetilde{E}_x} - \psi_{\widetilde{E}_z})|\widetilde{E}_x||\widetilde{E}_z|\right\}\delta(v_\parallel - V_{\rm r-1}), \end{aligned} \tag{C14}$$

$$\begin{aligned} P^{r}_{\rm sy}(v_\parallel, v_\perp, n=-1) &= \frac{4\pi^2 q_s^2}{W_{\rm EB} m_s k_\parallel}\frac{v_\perp^3 f_{s0}J_{-1}'(a_s)}{V_{\rm ts}^2} \\ &\times \left\{\frac{J_{-1}(a_s)}{a_s}\sin(\psi_{\widetilde{E}_y} - \psi_{\widetilde{E}_x})|\widetilde{E}_y||\widetilde{E}_x| + J_{-1}'(a_s)|\widetilde{E}_y|^2\right. \\ &\left.- \frac{v_\parallel}{v_\perp}J_{-1}(a_s)\sin(\psi_{\widetilde{E}_y} - \psi_{\widetilde{E}_z})|\widetilde{E}_y||\widetilde{E}_z|\right\}\delta(v_\parallel - V_{\rm r-1}), \end{aligned} \tag{C15}$$

$$
\begin{aligned}
P_{\rm sz}^{r}(v_{\|}, v_{\perp}, n=-1) &= \frac{4\pi^2 q_s^2}{W_{\rm EB} m_s k_{\|}} \frac{v_{\|} v_{\perp}^2 f_{s0} J_{-1}(a_s)}{V_{\rm ts}^2} \\
&\times \bigg[-\frac{J_{-1}(a_s)}{a_s} \cos(\psi_{\widetilde{E}_z} - \psi_{\widetilde{E}_x}) |\widetilde{E}_z||\widetilde{E}_x| \\
&+ J'_{-1}(a_s) \sin(\psi_{\widetilde{E}_z} - \psi_{\widetilde{E}_y}) |\widetilde{E}_z||\widetilde{E}_y| + \frac{v_{\|}}{v_{\perp}} J_{-1}(a_s) |\widetilde{E}_z|^2 \bigg] \\
&\times \delta(v_{\|} - V_{\rm r-1}).
\end{aligned} \tag{C16}
$$

C.3.2. Nonresonant Energy Transfer Rates

Nonresonant energy transfer rates at $n = -1$ are given as

$$
\begin{aligned}
P_{\rm sx}^{\rm nr}(v_{\|}, v_{\perp}, n=-1) &= \frac{2\pi q_s^2}{W_{\rm EB} m_s k_{\|}} \frac{(v_{\perp}^3/V_{\rm ts}^2) f_{s0}}{(v_{\|} - V_{\rm r-1})^2 + (\gamma/k_{\|})^2} \frac{J_{-1}(a_s)}{a_s} \\
&\times \bigg\{ \frac{\gamma}{k_{\|}} \frac{J_{-1}(a_s)}{a_s} |\widetilde{E}_x|^2 - [(v_{\|} - V_{\rm r-1}) \cos(\psi_{\widetilde{E}_x} - \psi_{\widetilde{E}_y}) \\
&+ \frac{\gamma}{k_{\|}} \sin(\psi_{\widetilde{E}_x} - \psi_{\widetilde{E}_y}) \bigg] J'_{-1}(a_s) |\widetilde{E}_x||\widetilde{E}_y| \\
&+ [(v_{\|} - V_{\rm r-1}) \sin(\psi_{\widetilde{E}_x} - \psi_{\widetilde{E}_z}) \\
&- \frac{\gamma}{k_{\|}} \cos(\psi_{\widetilde{E}_x} - \psi_{\widetilde{E}_z}) \bigg] \frac{v_{\|}}{v_{\perp}} J_{-1}(a_s) |\widetilde{E}_x||\widetilde{E}_z| \bigg\},
\end{aligned} \tag{C17}
$$

$$
\begin{aligned}
P_{\rm sy}^{\rm nr}(v_{\|}, v_{\perp}, n=-1) &= \frac{2\pi q_s^2}{W_{\rm EB} m_s k_{\|}} \frac{(v_{\perp}^3/V_{\rm ts}^2) f_{s0} J'_{-1}(a_s)}{(v_{\|} - V_{\rm r-1})^2 + (\gamma/k_{\|})^2} \\
&\times \bigg\{ \bigg[(v_{\|} - V_{\rm r-1}) \cos(\psi_{\widetilde{E}_y} - \psi_{\widetilde{E}_x}) + \frac{\gamma}{k_{\|}} \sin(\psi_{\widetilde{E}_y} - \psi_{\widetilde{E}_x}) \bigg] \frac{J_{-1}(a_s)}{a_s} |\widetilde{E}_y||\widetilde{E}_x| \\
&+ \frac{\gamma}{k_{\|}} J'_{-1}(a_s) |\widetilde{E}_y|^2 - [(v_{\|} - V_{\rm r-1}) \cos(\psi_{\widetilde{E}_y} - \psi_{\widetilde{E}_z}) + \frac{\gamma}{k_{\|}} \sin(\psi_{\widetilde{E}_y} - \psi_{\widetilde{E}_z}) \bigg] \\
&\times \frac{v_{\|}}{v_{\perp}} J_{-1}(a_s) |\widetilde{E}_y||\widetilde{E}_z| \bigg\},
\end{aligned} \tag{C18}
$$

$$
\begin{aligned}
P_{\rm sz}^{\rm nr}(v_{\|}, v_{\perp}, n=-1) &= \frac{2\pi q_s^2}{W_{\rm EB} m_s k_{\|}} \frac{(v_{\|} v_{\perp}^2/V_{\rm ts}^2) f_{s0} J_{-1}(a_s)}{(v_{\|} - V_{\rm r-1})^2 + (\gamma/k_{\|})^2} \\
&\times \bigg\{ \bigg[(v_{\|} - V_{\rm r-1}) \sin(\psi_{\widetilde{E}_z} - \psi_{\widetilde{E}_x}) - \frac{\gamma}{k_{\|}} \cos(\psi_{\widetilde{E}_z} - \psi_{\widetilde{E}_x}) \bigg] \\
&\times \frac{J_{-1}(a_s)}{a_s} |\widetilde{E}_z||\widetilde{E}_x| \\
&+ \bigg[(v_{\|} - V_{\rm r-1}) \cos(\psi_{\widetilde{E}_z} - \psi_{\widetilde{E}_y}) + \frac{\gamma}{k_{\|}} \sin(\psi_{\widetilde{E}_z} - \psi_{\widetilde{E}_y}) \bigg] \\
&\times J'_{-1}(a_s) |\widetilde{E}_z||\widetilde{E}_y| \\
&+ \frac{\gamma}{k_{\|}} \frac{v_{\|}}{v_{\perp}} J_{-1}(a_s) |\widetilde{E}_z|^2 \bigg\}.
\end{aligned} \tag{C19}
$$

Appendix D

Two Examples: Resonant and Nonresonant Energy Transfer Rates of the Parallel and Highly Oblique Alfvén Waves as Functions of the Wavenumber and β_p

This appendix summarizes resonant and nonresonant energy transfer rates of parallel and highly oblique Alfvén waves in k–β_p space. Generally, through the integration of energy transfer rates (e.g., the 2D distributions in Appendix C) in velocity space, we could obtain the total energy transfer rates at each n and each direction (x, y, or z). Here we perform this integration for the resonant energy transfer rate $P_s^r(n)$, and then we use the expression $P_s^{\rm nr} = P_s - \sum_n P_s^r(n)$ to give the nonresonant energy transfer rate for each species "s," where P_s is given by using Equation (34).

For the parallel Alfvén-mode wave, only the normal cyclotron wave–particle interaction appears. The resonant proton energy transfer rates $P_{\rm px}^r(n=1)$ and $P_{\rm py}^r(n=1)$ are analytically given by

$$
\begin{aligned}
P_{\rm px}^r(n=1) &= \frac{\sqrt{\pi}\,\omega_{\rm pp}^2}{2V_{\rm tp} k_{\|}} e^{-\frac{(1-\omega_r/\Omega_{\rm cp})^2}{\beta_p \lambda_p^2 k_{\|}^2}} \frac{\epsilon_0 (|\widetilde{E}_x|^2 + |\widetilde{E}_x||\widetilde{E}_y|)}{W_{\rm EB}}, \\
P_{\rm py}^r(n=1) &= \frac{\sqrt{\pi}\,\omega_{\rm pp}^2}{2V_{\rm tp} k_{\|}} e^{-\frac{(1-\omega_r/\Omega_{\rm cp})^2}{\beta_p \lambda_p^2 k_{\|}^2}} \frac{\epsilon_0 (|\widetilde{E}_y|^2 + |\widetilde{E}_x||\widetilde{E}_y|)}{W_{\rm EB}}.
\end{aligned} \tag{D1}
$$

Because $|\widetilde{E}_x| = |\widetilde{E}_y|$ for the parallel Alfvén wave, $P_{\rm px}^r(n=1) = P_{\rm py}^r(n=1)$. Also, because both $P_{\rm px}^r(n=1)$ and $P_{\rm py}^r(n=1)$ are nearly proportional to $\exp(-1/(\beta_p \lambda_p^2 k_{\|}^2))$, they become more damping at larger β_p and/or larger $\lambda_p k_{\|}$. This change in the damping rate is shown in Figure 18. In addition to the damping rate, Figure 18 also presents the k–β_p distributions of the wave frequency ω_r, the total resonant proton energy transfer rate $P_{\rm pt}^r = P_{\rm px}^r + P_{\rm py}^r$, and the total nonresonant proton energy transfer rate $P_{\rm pt}^{\rm nr}(n=1)$. This figure also identifies that ω_r is even smaller than $0.02\Omega_{\rm cp}$ as $\beta_p \to 100$ due to the significant damping therein. Moreover, $P_p^r/(2|\gamma|)$ is nearly larger than 2 in most of the regime with $10^{-4} \leqslant |\gamma|/\omega_r \leqslant 1$; the corresponding nonresonant proton energy transfer rate is considerably large, i.e., $P_p^{\rm nr}/(2|\gamma|) \lesssim -1$.

For highly oblique Alfvén waves propagating at $\theta = 89°$, in order to understand their wave–particle interactions, at first, we present the distributions of the wave frequency ω_r, the damping rate γ, and the phase difference $\psi_{\widetilde{E}_y} - \psi_{\widetilde{E}_z}$ between $\widetilde{E}_y$ and $\widetilde{E}_z$ in Figure 19.

Figure 19 shows that the damping rate normally increases with increasing β_p (where $\beta_e = \beta_p$). When $\beta_p \gtrsim 10$, the damping rate is so strong (e.g., $-\gamma/\omega_r \gtrsim 1$) that the wave can be even annihilated at $\lambda_p k \sim 0.1$ (see Figure 19(b)). Furthermore, with increasing β_p, $\psi_{\widetilde{E}_y} - \psi_{\widetilde{E}_z}$ is roughly decreasing from $-66°$ to $-82°$ and then increasing to $-15°$ at MHD scales. This phase difference will considerably determine the energy transfer direction resulting from resonant wave–particle interactions.

Before we discuss the distributions of resonant and nonresonant energy transfer rates, we give a preliminary analysis for their analytic expressions. Through the integration of Equations (C3) and (C4) in velocity space, we obtain

$$
\begin{aligned}
P_{\rm py}^r(n=0) &= \frac{\sqrt{\pi}\,\omega_{\rm pp}^2 \lambda_p k_{\perp}}{V_{\rm tp} k_{\|}} [I_0(b_p^2) - I'_0(b_p^2)] \\
&\times \left[\beta_p \lambda_p k_{\perp} + \frac{\omega_r}{V_A k_{\|}} \sin(\psi_{\widetilde{E}_y} - \psi_{\widetilde{E}_z}) \frac{|\widetilde{E}_z|}{|\widetilde{E}_y|} \right] e^{-\frac{\omega_r^2}{V_{\rm tp}^2 k_{\|}^2} - b_p^2} \frac{\epsilon_0 |\widetilde{E}_y|^2}{W_{\rm EB}},
\end{aligned} \tag{D2}
$$

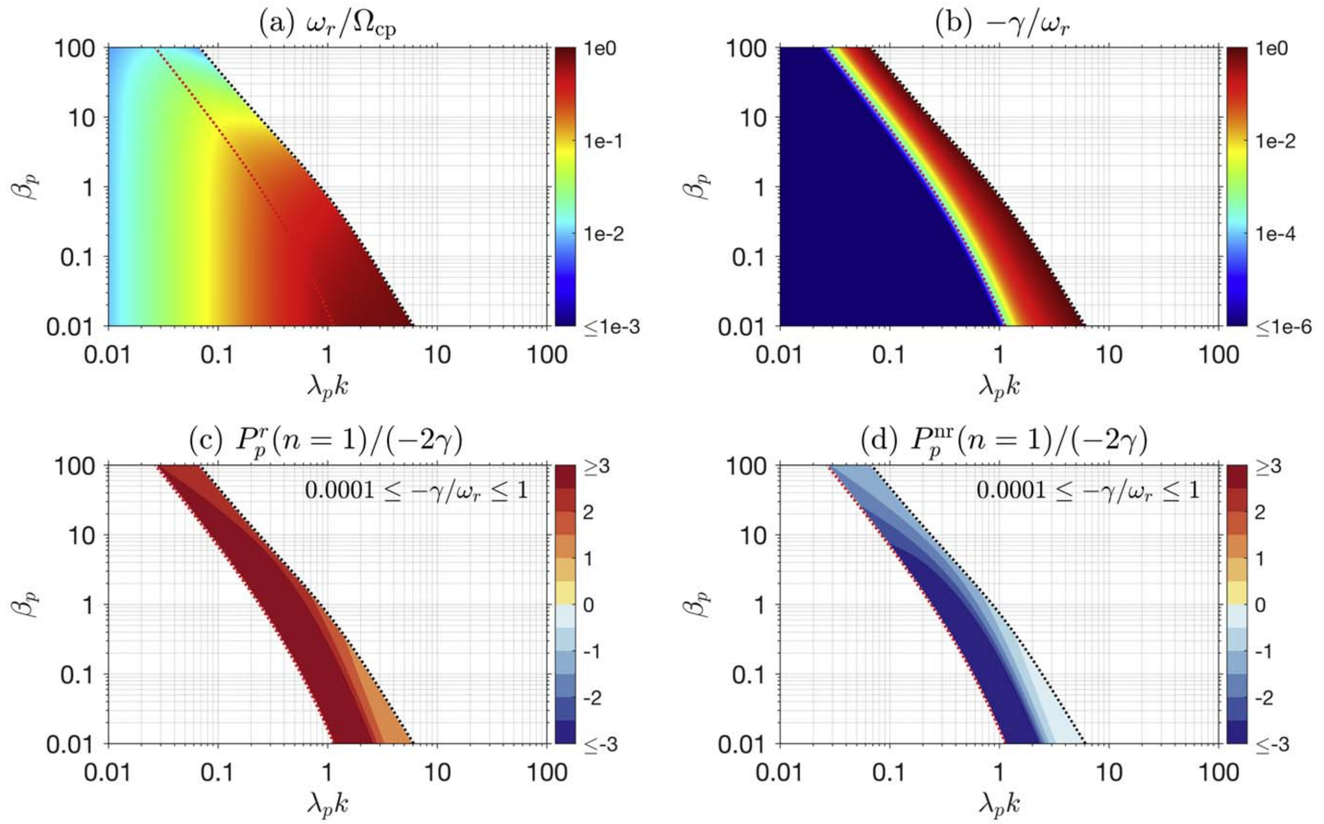

Figure 18. The distributions of (a) the real frequency normalized by the proton cyclotron frequency, $\omega_r/\Omega_{\rm cp}$, (b) the damping rate normalized by the real frequency, $-\gamma/\omega_r$, (c) the energy transfer rate induced by the $n = 1$ resonant wave–particle interaction, $P_p^r(n = 1)/(-2\gamma)$; and (d) the energy transfer rate induced by the $n = 1$ nonresonant wave–particle interaction, $P_p^{\rm nr}(n = 1)/(-2\gamma)$. The red and black dotted curves denote the contour lines of $\gamma/\omega_r = -10^{-4}$ and $\gamma/\omega_r = -1$, respectively.

and

$$P_{\rm pz}^r(n = 0) = \frac{\sqrt{\pi}\,\omega_{\rm pp}^2}{V_{\rm tp}k_\parallel}\frac{\omega_r}{V_A k_\parallel}[I_0(b_p^2) - I_0^{'}(b_p^2)] \times \left[\lambda_p k_\perp \sin(\psi_{\widetilde{E}_y} - \psi_{\widetilde{E}_z})\frac{|\widetilde{E}_y|}{|\widetilde{E}_z|} + \frac{2}{\beta_p}\frac{\omega_r}{V_A k_\parallel}\frac{I_0(b_p^2)}{I_0(b_p^2) - I_0^{'}(b_p^2)}\right] e^{-\frac{\omega_r^2}{V_{\rm tp}^2 k_\parallel^2} - b_p^2}\frac{\epsilon_0|\widetilde{E}_z|^2}{W_{\rm EB}}, \tag{D3}$$

where $b_p = \rho_p k_\perp$ and ρ_p denotes the proton gyroradius. Due to $\sin(\psi_{\widetilde{E}_y} - \psi_{\widetilde{E}_z}) < 0$ for these highly oblique Alfvén waves, $P_{\rm py}^r(n = 0)$ will turn to a positive value from a negative value with increasing β_p, and the transition point occurs at

$$\beta_{\rm pt1} = \frac{\omega_r}{V_A k_\parallel \lambda_p k_\perp}\sin(\psi_{\widetilde{E}_z} - \psi_{\widetilde{E}_y})\frac{|\widetilde{E}_z|}{|\widetilde{E}_y|}.$$

For $P_{\rm pz}^r(n = 0)$, different from $P_{\rm py}^r(n = 0)$, its value turns to negative from positive, and the transition point occurs at

$$\beta_{\rm pt2} = \frac{2\omega_r}{V_A k_\parallel \lambda_p k_\perp}\frac{I_0(b_p^2)}{I_0(b_p^2) - I_0^{'}(b_p^2)}\sin^{-1}(\psi_{\widetilde{E}_z} - \psi_{\widetilde{E}_y})\frac{|\widetilde{E}_z|}{|\widetilde{E}_y|}.$$

Moreover, when we only consider the term related to β_p in square brackets in Equations (D2) and (D3), $P_{\rm py}^r(n = 0)$ is nearly proportional to $\beta_p^{1/2}\exp(-1/\beta_p)$, and $P_{\rm pz}^r(n = 0)$ approximates $(1/\beta_p^{3/2})\exp(-1/\beta_p)$ in the positive energy transfer rate regime. Consequently, $P_{\rm py}^r(n = 0)$ is normally increasing with increasing β_p, and $P_{\rm pz}^r(n = 0)$ can reach the maximum at $\beta_p \sim 0.67$ at MHD scales.

For electron energy transfer rates, considering $b_e^2 = (\lambda_p^2 k_\perp^2/2)\beta_e(m_e/m_p) \ll 1$, their analytical expressions are given by

$$P_{\rm ey}^r(n = 0) = \frac{\sqrt{\pi}\,\omega_{\rm pp}^2 \lambda_p k_\perp}{V_{\rm te}k_\parallel} \times \left[\beta_e \lambda_p k_\perp + \frac{\omega_r}{V_A k_\parallel}\frac{|\widetilde{E}_z|}{|\widetilde{E}_y|}\sin(\psi_{\widetilde{E}_z} - \psi_{\widetilde{E}_y})\right]\frac{\epsilon_0|\widetilde{E}_y|^2}{W_{\rm EB}}, \tag{D4}$$

and

$$P_{\rm ez}^r(n = 0) = \frac{\sqrt{\pi}\,\omega_{\rm pp}^2}{V_{\rm te}k_\parallel}\frac{\omega_r}{V_A k_\parallel} \times \left[\lambda_p k_\perp \frac{|\widetilde{E}_y|}{|\widetilde{E}_z|}\sin(\psi_{\widetilde{E}_z} - \psi_{\widetilde{E}_y}) + \frac{2}{\beta_e}\frac{\omega_r}{V_A k_\parallel}\right]\frac{\epsilon_0|\widetilde{E}_z|^2}{W_{\rm EB}}. \tag{D5}$$

Different from proton energy transfer rates, the two sources of both $P_{\rm ey}^r(n = 0)$ and $P_{\rm ez}^r(n = 0)$ are in favor of wave damping. From their analytical expressions, we can directly find $P_{\rm ey}^r(n = 0) \propto \beta_e^{1/2}$ and $P_{\rm ez}^r(n = 0) \propto 1/\beta_e^{3/2}$. Moreover, due to $P_{\rm ey}^r(n = 0) \propto \lambda_p^2 k_\perp^2$ in the large-β_e regime, $P_{\rm ey}^r(n = 0)$ would easily yield $P_{\rm ez}^r(n = 0)$ at a large $\lambda_p k_\perp$ wherein.

The aforementioned features of the proton and electron energy transfer rates are evident in Figure 20, which presents the k–β_p distributions of both resonant and nonresonant energy transfer rates, where $\beta_e = \beta_p$. According to the magnitude

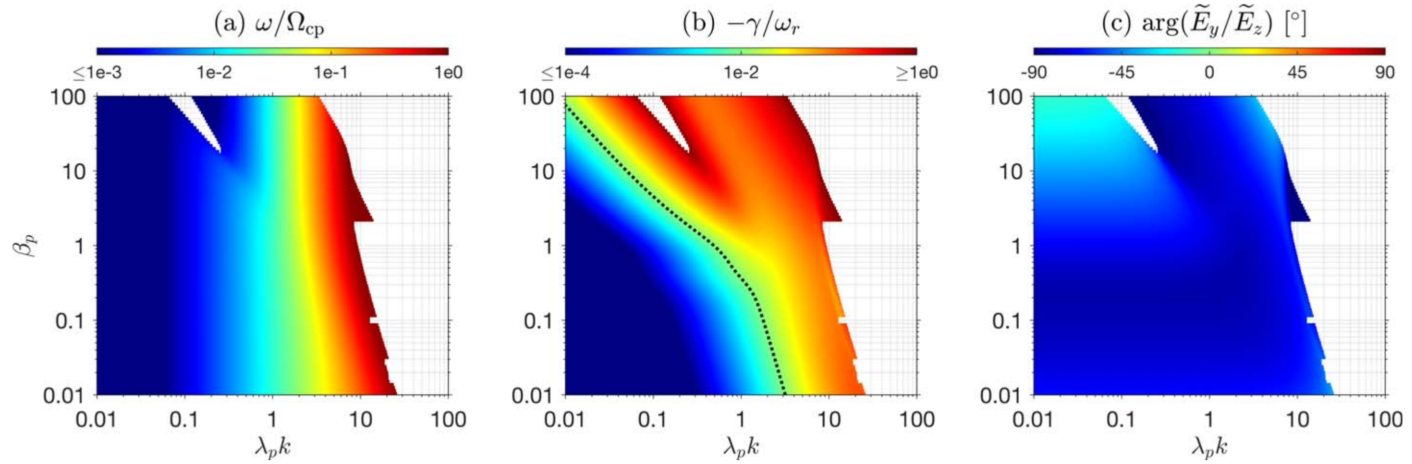

Figure 19. The distributions of (a) the real frequency normalized by the proton cyclotron frequency, $\omega_r/\Omega_{\rm cp}$, (b) the damping rate normalized by the real frequency, $-\gamma/\omega_r$, and (c) the phase difference $\psi_{\widetilde{E}_y} - \psi_{\widetilde{E}_z}$ between $\widetilde{E}_y$ and $\widetilde{E}_z$ for highly oblique Alfvén waves propagating at $\theta = 89°$. The black dotted curve denotes the contour line of $\gamma/\omega_r = -0.01$.

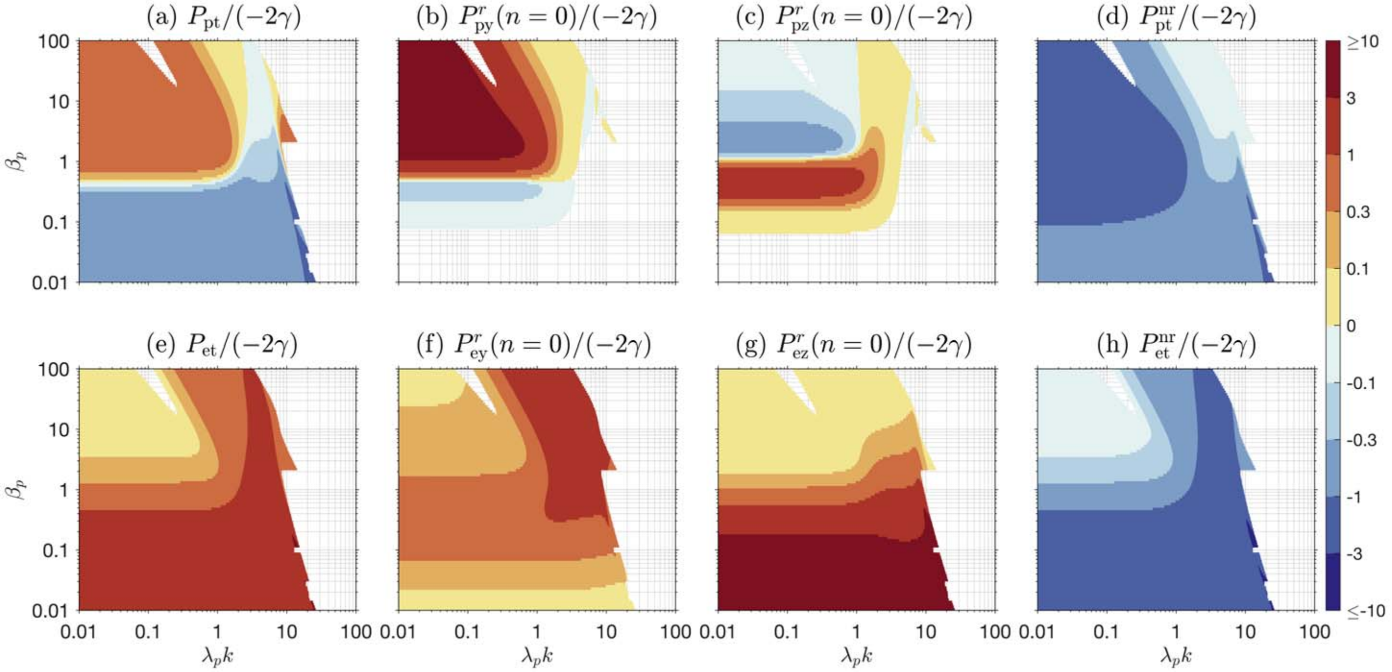

Figure 20. The distributions of the energy transfer rate of highly oblique Alfvén waves propagating at $\theta = 89°$. (a) The total proton energy transfer rate, $P_{\rm pt}$; (b) the proton energy transfer rate in the y direction (induced by the proton resonant transit-time interaction), $P^r_{\rm py}$; (c) the proton energy transfer rate in the z direction (induced by the proton resonant Landau interaction), $P^r_{\rm pz}$. The meaning of panels (e)−(h) is the same as that in panels (a)−(d), but for electrons. The data with values smaller than 10^{-5} are ignored in panels (b) and (c).

of each energy transfer rate, we further classify the resonant wave–particle interactions responsible for the damping of highly oblique Alfvén waves into the following four classes: (i) the proton transit-time damping regime ($P^r_{\rm py}(n=0)/(2|\gamma|) \gtrsim 1$), where $\lambda_p k \lesssim 1$ and $\beta_p \gtrsim 0.7$; (ii) the proton Landau damping regime ($P^r_{\rm pz}(n=0) \gtrsim 1$), where $\lambda_p k \lesssim 1$ and $\beta_p \sim 0.3-0.7$; (iii) the electron transit-time damping regime ($P^r_{\rm ey}(n=0) \gtrsim 1$), where $\lambda_p k \gtrsim 1$ and $\beta_e = \beta_p \gtrsim 0.3$; and (iv) the electron Landau damping regime ($P^r_{\rm pz}(n=0) \gtrsim 1$), where $\beta_e = \beta_p \lesssim 0.3$.

ORCID iDs

Jinsong Zhao https://orcid.org/0000-0002-3859-6394
Louchuang Lee https://orcid.org/0000-0003-4012-991X
Huasheng Xie https://orcid.org/0000-0001-9204-135X
Yuhang Yao https://orcid.org/0000-0002-3061-8763
Dejin Wu https://orcid.org/0000-0003-2418-5508
Yuriy Voitenko https://orcid.org/0000-0002-4139-1795
Viviane, Pierrard https://orcid.org/0000-0001-5014-7682

References

Barnes, A. 1966, PhFl, 9, 1483
Bellan, P. M. 2008, Fundamentals of Plasma Physics (Cambridge: Cambridge Univ. Press)
Cerri, S. S., Arzamasskiy, L., & Kunz, M. W. 2021, ApJ, 916, 120
Chen, C. H. K., Klein, K. G., & Howes, G. G. 2019, NatCo, 10, 740
Drummond, W. E., & Pines, D. 1962, Nuclear Fusion Supplement, 3, 1049
Duan, D., He, J., Bowen, T. A., et al. 2021, ApJL, 915, L8

Duan, D., He, J., Wu, H., & Verscharen, D. 2020, ApJ, 896, 47

Gary, S. P. 1986, JPlPh, 35, 431

He, J., Duan, D., Wang, T., et al. 2019, ApJ, 880, 121

He, J., Zhu, X., Verscharen, D., et al. 2020, ApJ, 898, 43

Hollweg, J. V. 1999, JGR, 104, 14811

Howes, G. G., Cowley, S. C., Dorland, W., et al. 2008, JGRA, 113, A05103

Howes, G. G., Klein, K. G., & Li, T. C. 2017, JPlPh, 83, 705830102

Kennel, C. F., & Engelmann, F. 1966, PhFl, 9, 2377

Kennel, C. F., & Wong, H. V. 1967, JPlPh, 1, 75

Kitamura, N., Shoji, M., Nakamura, S., et al. 2021, JGRA, 126, e28912

Klein, K. G., & Howes, G. G. 2016, ApJL, 826, L30

Klein, K. G., Howes, G. G., & Tenbarge, J. M. 2017, JPlPh, 83, 535830401

Klein, K. G., Howes, G. G., TenBarge, J. M., & Valentini, F. 2020, JPlPh, 86, 905860402

Leamon, R. J., Smith, C. W., Ness, N. F., Matthaeus, W. H., & Wong, H. K. 1998, JGR, 103, 4775

Liu, W., Zhao, J., Xie, H., et al. 2021, ApJ, 920, 158

Marsch, E. 2006, LRSP, 3, 1

Miyamoto, K. 2005, Plasma Physics and Controlled Nuclear Fusion, 38 (Berlin: Springer)

Quataert, E. 1998, ApJ, 500, 978

Sagdeev, R. Z., & Galeev, A. A. 1969, Nonlinear Plasma Theory (New York: Benjamin)

Schekochihin, A. A., Cowley, S. C., Dorland, W., et al. 2009, ApJS, 182, 310

Stix, T. H. 1992, in Waves in plasmas, ed. T. H. Stix (New York: American Institute of Physics)

Sun, H., Zhao, J., Liu, W., et al. 2021, ApJL, 916, L4

Vedenov, A. A., Velikhov, E., & Sagdeev, R. 1962, Nuclear Fusion Supplement, 2, 465

Verniero, J. L., Howes, G. G., Stewart, D. E., & Klein, K. G. 2021, JGRA, 126, e28361

Verscharen, D., Klein, K. G., & Maruca, B. A. 2019, LRSP, 16, 5

Woodham, L. D., Wicks, R. T., Verscharen, D., & Owen, C. J. 2018, ApJ, 856, 49

Wu, D. J., & Chen, L. 2020, Kinetic Alfvén Waves in Laboratory, Space, and Astrophysical Plasmas (Singapore: Springer)

Xie, H. 2019, CoPhC, 244, 343

Xie, H., Ma, H., & Bai, Y. 2021, arXiv:2111.05669

Zhao, J. 2015, PhPl, 22, 042115

Zhao, J. S., Voitenko, Y., Yu, M. Y., Lu, J. Y., & Wu, D. J. 2014, ApJ, 793, 107